Title
Synthesis, Characterization and Pore Structure Analysis of Mesoporous Materials

Author
Saldarriaga Lopez, Laura Carolina

Publication Date
2014

Peer reviewed|Thesis/dissertation

UNIVERISTY OF CALIFORNIA

Los Angeles

Synthesis, Characterization and Pore Structure Analysis of Mesoporous Materials

A dissertation submitted in partial satisfaction of the

requirements for the degree Doctor of Philosophy

in Chemistry

By

Laura Carolina Saldarriaga Lopez

2014

ABSTRACT OF DISSERTATION

Synthesis Characterization and Pore Structure Analysis of Mesoporous Materials

By

Laura Carolina Saldarriaga Lopez

Doctor in Philosophy in Chemistry

University of California, Los Angeles, 2014

Professor Sarah H. Tolbert, Chair

Self-assembly provides a route to make mesoporous structures that have accessible internal surface area. These types of materials show promise for use in opto-electronic devices as well as for energy storage devices. In this work we synthesize a range of mesoporous thin films from molecular and nanocrystal precursors. We characterize these films' porous structure and surface area using ellipsometric-porosimetry.

This work is divided into three parts; the first section focuses on synthesizing and characterizing mesoporous semiconducting films. Two approaches are utilized, one in which germanium Zintl clusters co-assemble with a charged surfactant via electrostatic attractions to produce an ordered organic/inorganic composite that can later be converted into a porous network by surfactant removal. The other method uses pre-formed cadmiun selenide

nanocrystals that coassemble with diblock copolymer micelles to produce a porous film with large accessible surface areas. Both of these nanostructured semiconductors are electrically interconnected, making them suitable for a range of applications.

In the second part of this work we focus on studying the pore structure of four different porous metal-oxide films. Mn_3O_4, $FeMn_2O_3$, ITO, and ITO coated with V_2O_5. All of these systems use nanocrystal/diblock copolymer assembly methods described above to produce a 3-D porous network with large accessible surface areas. Mn_3O_4, $FeMn_2O_3$ are redox active materials that were synthesized for their redox capacities. ITO nanocrystals coated with V_2O_5 are also redox active due to the vanadia coating. In all 3 systems the porous architectures exhibit high surface areas, providing ample redox active sites, and an interconnected open porosity, facilitating solvent/ion diffusion to those sites. In the case of ITO coated with vanadia we investigated the effect of vanadia coating thickness on surface accessibility.

In the final section we examine ways to measure surface area of thin films using ellipsometric-porosimetry combined with two different solvents: isopentane and methanol. We studied the advantages and disadvantages of each solvent in determining the surface area of the film.

Dissertation of Laura Carolina Saldarriaga Lopez is approved.

Bruce S. Dunn

Richard B. Kaner

Sarah H. Tolbert, Committee Chair

University of California, Los Angeles

2014

Para todos los que estuvieron de cuerpo y alma conmigo durante esta viaje – Gracias

For all of you who were present in my life during this trip – Thank you

TABLE OF CONTENTS

LIST OF FIGURES

CHAPTER 2. Synthesis and Characterization of Nanoporous Germanium Films Using Zintl Clusters

CHAPTER 3. Nanoporous Semiconductors Synthesized Through Polymer Templating of Ligand-Stripped CdSe Nanocrystals

CHAPTER 4. A General Method for the Synthesis of Hierarchical Nanocrystal-Based Mesoporous Materials

LIST OF TABLES

ACKNOWLEDGEMENTS

Where to start? There are so many people to thank that it would be an impossible task to remember every single one of them. I do however feel that throughout my time through UCLA I have met many people that have impacted my life positively, and of course there are the people before UCLA that have and still make my life as fun and wonderful as it is.

First of all my family, without my parents I would not be me. They have supported me throughout life in every decision I have made, good or bad, they have always being there and for that I am thankful. There is one person though that is so very special to me, without her, my life would be empty. My sister, of course, Silvia G. A. S. L. she has been extremely helpful especially when everything was going wrong, she was there for me to make me laugh, I cannot put in words what I feel when I write about her, Silvi, I hope you know that you have been fundamental to me making it all this way, I love you. Thanks for everything, including all the trips we took together, and also for getting a place in HI for me to come visit!

Many people have left a mark in my life, and I would like to mention just a few that will always stay with me. More than half of my life I spent in Colombia and I just want to mention that there are many people that looked up to me that I could not let them down, this is for all of you guys, you know who you are, and also for my two little goddaughters: Laura and Maria Jose! Here in the states I would like to thank to two great friends David Britt, Travis Pecorelli. The 3 of us became good friends during grad school and I cannot tell you how much I miss those poker sessions we were able to have our first quarter. Also to Dean Campbell the one person that since I met has supported me in every way, he is always there be it to tease me, help me, or dance with me. About a year ago he became more than a friend and for that I am very happy.

Dean thanks you for your motivational words, the dances, the hikes, the exercise, and all the good things that you brought into my life.

Of course I could not leave UCLA without thanking the people I worked with and the people that made it easier for me to navigate grad school. Joe Rangel became a really great friend and he helped me in so many ways. Every time I was in the machine shop he was there making sure I did not hurt myself and helping me in any way he could. He also would talk to me and listen to me when I needed it the most. Joe thank you very much for all your help, you really made it more pleasant to work here. I also want to thank Marek Grzeskowiak because he came to the rescue when I went through a rough economic time, my computer died and he was able to provide me with a computer to do my work, actually the one in which I am writing this, for that I am extremely thankful. Then there are all the people I actually spend all my time with: my lab mates. I have made some really good friends that will move on with me past grad school. First of all Iris Rauda, we started grad school together and she has always been there as a collaborator and a friend. I want to thank my friend Jessie because in the moments when I needed someone to talk she was always there and it always made me feel better. I also would like to thank Andrew Clark, he really helped me throughout my time here at UCLA, he was there to have conversations about science and many other topics that helped me understand a little more how grad school life was. And of course everyone else in the Tolbert lab, you guys are awesome people and I truly enjoyed my time here. I cannot leave though without thanking my adviser Sarah Tolbert, she definitely made me understand science on a different level than what I was used to, and because of her I feel that my scientific intuition has gotten sharper. She is a great teacher and I learned a lot from her. Thank you Sarah for all your help.

Professor Sarah H. Tolbert has directed the research presented in this dissertation.

Chapter 2 is a version of: Laura C. Saldarriaga-Lopez, Laura T. Schelhas, Sarah H. Tolbert, "Synthesis and Characterization of Nanoporous Germanium Films from Zintl Clusters." I wrote the manuscript and Professor Sarah H. Tolbert helped edit it. This manuscript will be submitted for publication shortly after this dissertation is filed.

Chapter 3 is a version of: Iris E. Rauda, Laura C. Saldarriaga-Lopez, Brett A. Helms, Laura T. Schelhas, Daniel Membreno, Delia J. Milliron, Sarah H. Tolbert, "Nanoporous Semiconductors Synthesized Through Polymer Templating of Ligand-Stripped CdSe Nanocrystals." Iris wrote the manuscript. Drs. Brett A. Helms, Delia J. Milliron and Professor Sarah H. Tolbert helped edit the manuscript. This manuscript has been submitted for publication to *Advanced Materials*.

Chapter 4 is a version of: Iris E. Rauda, Raffaella Buonsanti, Laura C. Saldarriaga-Lopez, Kanokraj Benjauthrit, Laura T. Schelhas, Morgan Stefik, Veronica Augustyn, Jesse Ko, Bruce Dunn, Ulrich Wiesner, Delia J. Milliron, Sarah H. Tolbert, "General Method for the Synthesis of Hierarchical Nanocrystal-Based Mesoporous Materials." *ACS Nano*, 2012, *6*, 6386–6399. Copyright 2012 American Chemical Society. Iris wrote the manuscript. Drs. Raffaella Buonsanti, Delia J. Milliron and Professor Sarah H. Tolbert helped edit the manuscript.

Chapter 5 is a version of: Iris E. Rauda, Veronica Augustyn, Xinyi Chen, Laura C. Saldarriaga-Lopez, Laura T. Schelhas, Gary Rubloff, Bruce Dunn, Sarah H. Tolbert, "High-Performance Pseudocapacitors Based on Atomic Layer Deposition of V2O5 onto Conductive Nanocrystal-Based ITO Mesoporous Scaffolds." Iris Rauda and I wrote the manuscript. Professor Sarah H. Tolbert helped edit the manuscript. This manuscript will be submitted for publication shortly after this dissertation is filed.

Chapter 6 is a version of Laura C. Saldarriaga-Lopez, Sarah H. Tolbert "Room Temperature Surface Area Measurement of Thin Films by Ellipsometric-Porosimetry" I wrote the manuscript. Professor Sarah H. Tolbert helped edit the manuscript.

Most of the work in this dissertation was supported by: California NanoSystem Institute (CNSI); National Science Foundation (NSF); NSF Integrative Graduate Education and Research Traineeship Program (IGERT); Center for Molecularly Engineered Energy Materials (MEEM), an Energy Frontier Research Center funded by the U.S. Department of Energy (D.O.E.), Office of Science, Office of Basic Energy Sciences; University of California Multicampus Research Programs and Initiatives (UC MRPI); and the UCLA Graduate Division. Portions of this research were performed as a user project at the Molecular Foundry, Lawrence Berkeley National Laboratory, which is supported by the Office of Science, Office of Basic Energy Sciences, of the U.S. D.O.E. Portions of this research were carried out at the Stanford Synchrotron Radiation Laboratory, a national user facility operated by Stanford University on behalf of the U.S. Department of Energy, Office of Basic Energy Sciences.

VITA

2004	A. A. Degree, Golden West College, Huntington Beach
2006	B.S Chemistry, University of California San Diego
2006-2007	First year graduate division award fellowship, UCLA
2007-2009	Materials Creation Training program, NSF IGERT, UCLA
2007, 2010-2013	Teaching Assistant, Department of Chemistry, UCLA
2009	Internsip, Comision Nacional de Energia Atomica, Buenos Aires Argentina
2013	Hanson-Dow Excellence in Teaching award, UCLA

PUBLICATIONS AND PRESENTATIONS

I. E. Rauda, V. Augustin, **L. C. Saldarriaga-Lopez**, X. Chen, L. T. Schelhas, G. Rubloff, B. Dunn, S. H. Tolbert. "High-Performance Pseudocapacitors Based on Atomic Layer Deposition of V_2O_5 onto Conductive Nanocrystal-Based ITO mesoporous Scaffolds" 2014 manuscript ready to be submitted to Advanced Functional Materials

I. E. Rauda, **L. C. Saldarriaga-Lopez**, B. A. Helms, L. T. Schelhas, D. Membreno, B. Dunn, D. J. Milliron, S. H. Tolbert. "Nanoporous Semiconductors Synthesized Through Polymer Templating of Ligand-Stripped CdSe nanocrystals." *Adv. Mater.* 2013, *25*, 1315-1322.

I. E. Rauda, R. Buonsanti, **L. C. Saldarriaga-Lopez**, K. Benjaurhrit, L. T. Schelhas, M. Stefik, V. Augustyn, J. Ko, B. Dunn, U. Wiesner, D. J. Milliron, S. H. Tolbert. "General Method for the Synthesis of Hierarchical Nanocrystal-Based Mesoporous Materials." *ACS Nano* 2012, *6*, 6386-6399.

Laura C. Saldarriaga lopez, Sarah H. Tolbert. "Synthesis and Characterization of Nanoporous Germanium Films" Invited Talk 2009 MSI / IGERT Conference, University of Oregon

Laura C. Saldarriaga-Lopez, Alejandra Calvo, Galo Soler-Illia, Sarah H. Tolbert. "Detailed Characterization of Amino Functionalized Silica Films Using Ellipsometry-Porosimetry." Poster Presented at the MCTP/IGERT symposium, UCLA, 2009

Laura C. Saldarriaga lopez, Sarah H. Tolbert . "Synthesis of Nanoporous Germanium Thin Films" Poster presented at the MSI / IGERT Conference. University of Oregon, 2009

CHAPTER 1

Introduction

Being able to control the properties of porous materials at the nanoscale using synthetic methods can be very advantageous for producing mesostructured materials with different optical, and electronic characteristics that can be used for a wide variety of applications.[1–6] A bottom-up approach is to start with the basic building blocks or precursors in a solution-phase synthesis. These precursors must be soluble species that can either self-assemble, or co-assemble with a structure directing agent or template from solution by a sol-gel method, to produce a material with a unique architecture that may exhibit structural and/or compositional-dependent properties.[7]

The solution-phase syntheses used in this work are simple, cost-effective methods to producing nanostructured, mesoporous materials. Assembly of an inorganic precursor with an organic template has been studied in depth and there are many examples of mesostructured templated materials in the literature, such as mesoporous oxides and non-oxides.[1–6,8–11] Silica-based materials are very well-known mesoporous structured materials that are prepared using a sol-gel method. This method[12–14] has been extended to organosilicates as well as metal-chalcogenides and transition metal oxides. Nanostructured semiconductors are particularly interesting functional materials because they have high optical absorption coefficients, tunable band gaps in the visible region, and demonstrate quantum confinement when they are nanodimensional, which gives them new physical properties that makes them optimal for electronic applications.[15,16]

There is ample research on semiconducting materials with well-defined nanoscale architectures such as nanocrystal arrays,[17,18] etched nanoporous materials,[19] and nanowire forests based on

both carbon nanotubes and inorganic nanowires;[20,21,22,23] however there is not much work on templated non-oxide systems with periodic nanostructure. Some of the latest examples of templated non-oxides include systems of poly-charged Zintl clusters.[24,25] The periodicity of these materials arises from co-assembly of cationic surfactant species with the polycharged zintl anion. In order to make the structures more robust, the inorganic framework must be cross-linked with a transition metal cation. One disadvantage of these types of materials is that the template cannot be removed as the order is lost upon removal, therefore losing all the porosity.[26,27] Nevertheless, there have been successful attempts at leaving behind a fully porous network of non-oxide materials in the powder form using the same ion-mediated cross-linking polymerization of Ge_9^{4-} zintl clusters to make intermetallic architectures.[28,29]

As mentioned above, transition metal oxides are another type of materials that have also recently gained attention due to their redox properties. Porous films of these materials are currently under investigation for their ability to function as pseudocapacitors. Pseudocapacitors have become increasingly popular recently because they can provide greater power, faster charge/discharging times, and longer charge/discharge cycling stability than traditional batteries.[30] Pseudocapacitors store energy using faradaic processes that involve surface reactions, avoiding the limitation of long ion diffusion distances through the bulk system like a traditional battery. An ideal architecture should include short ion diffusion lengths, high surface area with accessibility to all redox active sites, and conductivity incorporated into it. Nanostructured porous materials provide a solid base to build on because they fulfill these requirements. In our group we have previously developed a model system that uses anatase titania nanocrystals made into a thin film that demonstrated enhanced pseudocapacitive charge storage.[7] The titania nanocrystals were co-assembled with a block copolymer by an evaporation-induced self-assembly process, followed

by removal of the template, to yield a mesoporous inorganic composite with high surface area. Enhancement of electrochemical properties was observed and the large surface area arising from the mesoporosity and microporosity provided sufficient redox active sites.

We are capable of controlling the nanoscale architecture of inorganic mesoporous materials using solution-phase methods. Here we present two types of porous films: first, dense wall films where the inorganic precursor is a molecular species that produces a polymeric chain, generating a dense wall, and second, nanocrystalline films where the inorganic presursors are pre-formed bare nanocrystals stabilized in solution, making a wall with micropores arising from the spacing between the nanocrystals. In both cases the inorganic precursor co-assembles with the organic template to produce a composite material that can be treated to wash/decompose the organic matter leaving behind a porous network of the inorganic material.

This work is divided into 5 chapters. We present the characterization and analysis of the properties and the pore structure of different types of mesoporous films ranging from pure semiconductors such as germanium, and cadmium selenide (chapters 2 and 3), to nanocrystals films that were coated with a thin layer of V_2O_5 in chapters 4 and 5. We are interested in the novel properties that arise from making films with nanoscale morphology. The germanium and cadmium selenide systems are attractive because they are well-known semiconductors that have a great potential for use in opto-electronic devices. The other systems studied use a facile solution phase synthesis and the focus is on energy storage applications. Starting with pre-formed ITO, Mn_3O_4 and $MnFe_2O_3$ nanocrystals as the building blocks, we make porous films using two block copolymers to show the tunability of the pore size, porosity and accessible area in the materials. And lastly ITO nanocrystal films coated with V_2O_5 were studied for use in

pseudocapacitors, taking advantage of the redox properties of vanadia and the fact that a thin layer, via ALD, could be deposited onto the ITO nanocrystalline fim.

As mentioned above in Chapter 2 we present the synthesis of a porous network using a germanium zintl $(Ge_9)^{4-}$ cluster that polymerizes into $(Ge_9)_n^{2-}$ under mild acidic conditions to then self-assemble around a charged surfactant such as cetyltriethylammonium bromide (CTEAB). We produce continuous, mesoporous, non-oxidized germanium thin films. These films have the advantage of being more mechanically stable than the powder[25] form while retaining the same architecture. We synthesize these films by borrowing ideas from the sol-gel chemistries, as we can control the extent of polymerization of the germanium zintl cluster using a mild oxidizing agent, in our case ammonium bromide, to slowly polymerize the monomeric Ge_9^{4-} to $(Ge_9)_n^{2-}$. This species can easily co-assemble with a surfactant (CTEAB) to produce an ordered nanoporous film due to the electrostatic attraction of the negatively zintl ion to the positive charge head on the surfactant producing an organic/inorganic composite where the organic template can be removed upon oxidation of the inorganic species. These films are continuous, non-oxidized, porous films that have possible applications in microelectronic devices.

In recent years, the synthesis of nanoporous materials has been achieve by the utilization of large amphiphilic diblock copolymers by self-assembly with preformed nanocrystals of oxide systems.[31–34] In chapter 3 we explore this avenue and take it one step further with the synthesis of porous semiconducting films of cadmium selenide (CdSe). Here we focus on making a mesoporous nanocrystalline film where we use a diblock copolymer that forms micelles in polar solvents, to template colloidal CdSe nanocrystals into mesoporous hierarchical architectures that exhibit a high surface area and a bimodal porosity. The pre-formed CdSe nanocrystals, are highly

soluble and dispersed in solution as a result of the nanocrystals being stripped off their native ligands using a ligand exchange process that utilizes Meerwin's salt (Et_3OBF_4) as the stripping agent.[35] We then use an evaporation induced self-assembly process to generate organic/inorganic films where the polymer can be decomposed under inert conditions to produce a CdSe-based mesoporous films that retains the semiconducting properties of CdSe, including quantum confined excitonic absorption and modest carrier mobilities. This approach to make air sensitive semiconducting films can be extended to any type of nanocrystals, since the chemistry is not specific to the CdSe reactivity demonstrating the generality of this method.

The next part of this work goes into detail about the fabrication and design rules that we propose to make an effective energy storage device such as a pseudocapacitor. In chapter 4 we build upon our previous work on titania pseudocapacitors and continue to construct this ideal architecture by making nanocrystal thin films using different types of transition metal oxides. We use a wider range of nanocrystal systems including manganese oxide (Mn_3O_4), manganese ferrite ($FeMn_2O_4$) and ITO nanocrystals. These nanocrystals were ligand-stripped using an established ligand-exchange method, similar to the one used in chapter 3, that uses $NOBF_4$ salt to produce soluble precursors that can self-assemble to make an ordered architecture. We varied the size of the nanocrystals and the block lengths of the block copolymers used, to study and analyze the porosity and pore size produced by each system. We found that by varying the size of the nanocrystals we could tune the microporosity of the film and by changing the block copolymer length we could tune the mesopore size in the film. This result was not dependent on the type of nanocrystal used, demonstrating a general route to produce mesoporous nanocrystal films. Also we showed that templated Mn_3O_4 exhibits enhanced pseusocapacitive storage compared to untemplated nanocrystal films, establishing once more the effectiveness of the architecture.

In chapter 5 we continue to build on the same type of mesoporous structure, this time, integrating conductivity into the network. Electrical conductivity can be a limitation if thicker films are desired for commercial applications. Therefore we construct a model system where we template ITO nanocrystals into a mesoporous network to then coat them with a thin layer of vanadia via ALD, to produce a structure that incorporates the large surface area of the porous architecture, with the redox properties of the vanadia while still maintaining good electrical conductivity throughout the film. Here, we deposit variable thicknesses of V_2O_5, annealed at two different temperatures, onto the ITO scaffolds and study the limitations that come with depositing thicker films as well as the effects of the crystallinity of the vanadia layer. We concluded that at low temperatures, up to a thickness of 7nm of vanadia we still retain the pseudocapacitance mechanism for charge storage which is not limited by ion diffusion into the redox active layer.

In chapter 6 we switch gears and discuss surface area measurements for thin films. To date there are few measurements that can be used to measure the surface area of a thin film because in a thin film there is not much material.[36,37] We propose a new method using ellipsometric-porosimetry[37–39] by exploring new solvents that can generate a BET region[40–42] and allow for the calculation of surface area in thin films. This method provides the flexibility of using two solvents to compare as well it is the advantage to do all the measurements at room temperature.

Finally, in chapter 7 we conclude with an overview of all the chapters in this work and a possible path to continue with this work if desired|.

1.1 References

(1) D. m. Antonelli, J. Y. Y. *Angew. Chem. Int. Ed. Engl.* **1996**, *35*, 426–430.

(2) Armatas, G. S.; Kanatzidis, M. G. *Nature* **2006**, *441*, 1122–1125.

(3) Mohanan, J. L.; Arachchige, I. U.; Brock, S. L. **2014**, *397*.

(4) Kresge, C.; Leonowicz, M.; Roth, W. *Nature* **1992**, *359*, 710–712.

(5) Z-R. Tian, E. al. *Science (80-.).* **1997**, *276*, 926–930.

(6) Attard, G. S.; Corker, J. M.; Göltner, C. G.; Henke, S.; Templer, R. H. *Angew. Chemie Int. Ed. English* **1997**, *36*, 1315–1317.

(7) Brezesinski, T.; Wang, J.; Polleux, J. *J. Am. Chem. Soc.* **2009**, 1802–1809.

(8) Inagaki, S.; Guan, S.; Ohsuna, T.; Terasaki, O. *Nature* **2002**, *416*, 304–307.

(9) Rangan, K. K.; Trikalitis, P. N.; Kanatzidis, M. G.; Lansing, E.; June, R. V. **2000**, 10230–10231.

(10) Spectroscopic, R.; Liebert, R. K. **1999**, *402*, 867–871.

(11) Zou, X.; Conradsson, T.; Klingstedt, M.; Dadachov, M. S.; O'Keeffe, M. *Nature* **2005**, *437*, 716–719.

(12) Soler-Illia, G.; Crepaldi, E. *Curr. Opin. colloid ...* **2003**, *8*, 109–126.

(13) Lu, Y.; Ganguli, R.; Drewien, C.; Anderson, M. *Nature* **1997**, *389*, 651–655.

(14) Liong, M.; Lu, J.; Kovochich, M.; Xia, T.; Ruehm, S. G.; Nel, A. E.; Tamanoi, F.; Zink, J. I. *ACS Nano* **2008**, *2*, 889–896.

(15) Shi, Y.; Wan, Y.; Zhao, D. *Chem. Soc. Rev.* **2011**, *40*, 3854–3878.

(16) Ramasamy, K.; Malik, M. A.; Revaprasadu, N.; O'Brien, P. *Chem. Mater.* **2013**, *25*, 3551–3569.

(17) Woodward, I.; Schofield, W. C. E.; Roucoules, V.; Badyal, J. P. S. **2003**, 3432–3438.

(18) Hosono, E.; Fujihara, S.; Honma, I.; Zhou, H. *J. Am. Chem. Soc.* **2005**, *127*, 13458–13459.

(19) Jung, K.; Shih, S.; Kwong, D. *J. Electrochem. Soc.* **1993**, *140*.

(20) *Int. J. Nanosci.* **2002**, *1*.

(21) Xia, Y.; Yang, P.; Sun, Y.; Wu, Y.; Mayers, B.; Gates, B.; Yin, Y.; Kim, F.; Yan, H. *Adv. Mater.* **2003**, *15*, 353–389.

(22) Plasticity, R. T.; Smith, D. A.; Holmberg, V. C.; Korgel, B. A. *ACS Nano* **2010**, *4*, 2356–2362.

(23) Hanrath, T.; Korgel, B. a. *Adv. Mater.* **2003**, *15*, 437–440.

(24) Armatas, G. S.; Kanatzidis, M. G. *Adv. Mater.* **2008**, *20*, 546–550.

(25) Sun, D.; Riley, A. E.; Cadby, A. J.; Richman, E. K.; Korlann, S. D.; Tolbert, S. H. *Nature* **2006**, *441*, 1126–1130.

(26) Korlann, S. D.; Riley, A. E.; Kirsch, B. L.; Mun, B. S.; Tolbert, S. H. *J. Am. Chem. Soc.* **2005**, *127*, 12516–12527.

(27) Riley, A. E.; Korlann, S. D.; Richman, E. K.; Tolbert, S. H. *Angew. Chem. Int. Ed. Engl.* **2005**, *45*, 235–241.

(28) Armatas, G. S.; Kanatzidis, M. G. *J. Am. Chem. Soc.* **2008**, *130*, 11430–11436.

(29) Armatas, G. S.; Kanatzidis, M. G. *Nat. Mater.* **2009**, *8*, 217–222.

(30) Miller, J.; Simon, P. *Sci. Mag.* **2008**, *321*, 651–652.

(31) Rauda, I. E.; Saldarriaga-Lopez, L. C.; Helms, B. a; Schelhas, L. T.; Membreno, D.; Milliron, D. J.; Tolbert, S. H. *Adv. Mater.* **2013**, *25*, 1315–1322.

(32) Rauda, I. E.; Buonsanti, R.; Saldarriaga-Lopez, L. C.; Benjauthrit, K.; Schelhas, L. T.; Stefik, M.; Augustyn, V.; Ko, J.; Dunn, B.; Wiesner, U.; Milliron, D. J.; Tolbert, S. H. *ACS Nano* **2012**, *6*, 6386–6399.

(33) Warren, S. C.; Messina, L. C.; Slaughter, L. S.; Kamperman, M.; Zhou, Q.; Gruner, S. M.; DiSalvo, F. J.; Wiesner, U. *Science* **2008**, *320*, 1748–1752.

(34) Buonsanti, R.; Pick, T. E.; Krins, N.; Richardson, T. J.; Helms, B. a; Milliron, D. J. *Nano Lett.* **2012**, *12*, 3872–3877.

(35) Rosen, E. L.; Buonsanti, R.; Llordes, A.; Sawvel, A. M.; Milliron, D. J.; Helms, B. a. *Angew. Chem. Int. Ed. Engl.* **2012**, *51*, 684–689.

(36) Nina, H.; Barron, A. R. 1–11.

(37) Baklanov, M. R.; Mogilnikov, K. P.; Polovinkin, V. G.; Dultsev, F. N. *J. Vac. Sci. Technol. B Microelectron. Nanom. Struct.* **2000**, *18*, 1385.

(38) Boissiere, C.; Grosso, D.; Lepoutre, S.; Nicole, L.; Bruneau, A. B.; Sanchez, C. *Langmuir* **2005**, *21*, 12362–12371.

(39) Fuertes, M.; Colodrero, S. *J. Phys. Chem. C Lett.* **2008**, *112*, 3157–3163.

(40) Brunauer, S.; Deming, L. *J. Am. Chem. Soc.* **1940**, *1139*.

(41) Brunauer, S.; Emmett, P.; Teller, E. *J. Am. Chem. Soc.* **1938**, *407*.

(42) Krause, K. M.; Thommes, M.; Brett, M. J. *Microporous Mesoporous Mater.* **2011**, *143*, 166–173.

CHAPTER 2.

Synthesis and Characterization of Nanoporous Germanium Films from Zintl Clusters

2.1 Introduction

In recent years much emphasis has been placed on investigating various types of semiconducting materials, amongst which germanium and silicon have been extensively studied for their applications in integrated circuits, sensing materials and optoelectronic and energy conversion devices.[1,2] One advantage of semiconducting materials is that they possess visible photoluminescence,[3] absorptive properties, and at the nanoscale their physical properties change due to quantum confinement.[4] There are some examples of pure elemental porous semiconducting films in the literature,[5,6] but it is still difficult to fabricate these films in a simple and robust way due to the reactivity of the precursors. In this work, we report a facile synthesis of nanoporous ordered germanium thin films, via interface nucleation, from Zintl clusters co-assembled with a cationic surfactant.

Solution-phase self assembly is a well known technique to produce nanostructured architectures with ordered mesoporosity. Metal oxides are some of the most common materials successfully produced using traditional sol-gel chemistries, via evaporation induced self-assembly methods.[7–9] Solution-gelation, as the name implies, is generally achieved by hydrolyzing an inorganic precursor, followed by condensation to make the oxide bonds and polymeric species that can co-assemble with a surfactant or block co-polymer templating agent. Films are then produced either by interface nucleation at the liquid-gas interface, spin-coating or dip-coating. These methods require careful preparation of the solution as it needs to age, is sensitive to pH, and humidity, concentration and in general is mostly limited to oxide materials.

Also, dip-coating and spin-coating are difficult methods to scale up since as the film becomes thicker cracking becomes a problem. Free standing films nucleated at the liquid-gas interface is also a well studied method to prepare silica films. These films are also produced by co-assembly of the silica precursor with a surfactant usually at very dilute acidic conditions. This method is very attractive however, because the films can vary in thickness from ten of nanometer to over 20μm without cracking, and because of the film's capability to serve as free standing membranes.[10] Some other applications of porous oxides include uses as ion exchange materials, catalysts supports,[11] micro machines for drug delivery[12] and as host for making new architectures. However, most porous oxide thin films have the disadvantage that they are either insulators or wide-band gap semiconductors, which limits their applications where conductivity is required.[13] In addition, for many adsorbent or reactive applications, the oxide limits the nature of the bonding and the types of intermolecular interactions that can be achieved.

Non-oxide films can also be prepared using a sol-gel technique via evaporation induced self-assembly method. One example uses preformed soluble bare nanocrystals that self-assemble around a block copolymer to produce an ordered architecture.[14,15] Also other nanostructured materials such as wires can be obtained using a hard template such as alumina to make different types of nanostructures from non-oxide precursors.[16,17]

Our focus in this paper is on germanium because it has high electron and hole mobilities,[18] as well as a smaller band gap when compared to silicon,[19] which makes it extremely useful as a component in heterostructured based solar cell[20]. In the literature, we can find several syntheses for making nanostructured porous germanium materials using a number of techniques some of which include spark processing,[21] inductively couple plasma chemical vapor deposition (ICPCVD),[22] reduction of germanium oxide films in a reducing hydrogen atmosphere,[5] and

electrochemical etching and anodization[23–25]. With these techniques, the porous architecture cannot be controlled well, creating a disordered network. We want to move away from these techniques and explore the possibilities of using zintl clusters as the molecular precursors to making films using solution based methods.

Zintl phases are highly reduced polycharged species generated by the reaction with an alkali metal at hight temperatures.[26–29] They have been known for a long time but recently they have been used to produce nanostructured materials taking advantage of their solubility in non-aqueous polar solvents, and anionic charge to self-assemble with cationic surfactant species. These nanoscale ordered composite materials are generally synthesized from cooperative assembly of poly-charged Zintl clusters and cationic surfactants. The inorganic framework, made from clusters anions, is cross-linked by transition metal cations. Thus the band-gap of the nanosrtuctured materials can be fine tuned by varying either the chemical constituents of the Zintl anions or the transition metal cations in the system. However, while the structure formed is robust, the surfactant cannot be removed without collapse of the nanostructure.[13,30,31]

In our group we have reported the synthesis of a germanium porous architecture that uses zintl Ge_9^{4-} clusters as the precursors to self-assemble around a charged surfactant such as cetyltriethyl ammonium bromide CTEAB producing a hexagonally ordered structure that can be fully oxidized to remove the surfactant avoiding a collapse of the porous structure.[32] We use ethylenediamine as the solvent of choice because the germanium is soluble and stable in it therefore the reaction times are reasonable. Others have also reported using the germanium zintl cluster to make intermetallic architectures.[33,34]

Here, we want to investigate other types of nanostructured materials moving away from powders therefore we take advantage of this opportunity to develop a method that can produce thin mesoporous germanium films with ordered porosity. We want to explore two different methods; interface nucleation at the liquid-gas interface[10,35–40] as well as spin-coating. Our goal in this work is to produce a germanium film that is porous, continuous and can have better conductivity throughout since they do not require binders to make them electrically connected. These thin films can be used for fundamental intrinsic studies as well as in applications such as thin film batteries, solar cells, and on-chip applications.

We fabricate these films through a sol-gel type chemistry, using a germanium zintl cluster.[41,42] By controlling the extent of polymerization of the germanium zintl cluster from the monomeric Ge_9^{4-} to $(Ge_9)_n^{2-}$ using a mild oxidizing agent, we can mimic conditions similar to those found in the slowly condensing sol-gel solutions. Co-assembly of the oligomerized species with the surfactant, cetyltriethylammonium bromide (CTEAB), produces an ordered nanostructured organic/inorganic composite. This network is formed due to the electrostatic attraction between the negatively charged zintl ion cluster to the positively charge surfactant. Further oxidation of the anionic Ge polymer to amorphous, zero valent Ge breaks this ionic bond and allows us to obtain a composite where the organic template can be removed using a simple solvent wash.

As mentioned above we explore two different methods to prepare these films. Interface nucleated films utilize the slow polymerization of the zintl cluster with the slow addition of an acid to produce a free-standing film where we can control how fast the film forms by varying the amount of oxidizing agent used. The second method employs more standard sol-gel fabrication techniques where by spin-coating from homogeneous precursor solution onto a substrate in an

inert atmosphere. Here we compare the porosity, nanoscale periodicity, and overall film quality produced by these two methods in an effort to expand the range of materials that can readily be deposited as nanoporous films from solution.

2.2 Results and discussion

2.2.1 Film Synthesis: The synthesis of mesoporous germanium films was achieved by oxidatively crosslinking zintl germanium oligomers in the presence of a cationic surfactant, CTEAB, under inert conditions to produce an inorganic/organic composite material with nanoscale periodicity. We took advantage of the interface-nucleation method, (refs) in which films nucleate on surfactant arrays that assemble at the solvent/air interface. The germanium precursor solution is mixed with the surfactant under very mild oxidizing conditions to slowly polymerize the negatively charged zintl clusters into a polyelectrolyte. In this method we use ammonium bromide as the oxidizing agent because it is a very weak acid that can polymerize the monomeric zintl cluster, liberating hydrogen gas according to the following reaction:

$$(Ge_9)^{4-} + 2H^+ \rightarrow (Ge_9)_n^{2-} + H_2$$

These anionic Ge polymers will then co-assemble with polycharged organic species. If the reaction is slow because of a low acid concentration, co-assembly will occur preferentially at the surfactant array that assembles at the interface of the solvent and the vapor phase. The slow reaction also appears to help produce a well-ordered organic/inorganic film. Because the film can continually grow once it has nucleated, growth time allows us to tune the thickness of the films ranging from a couple hundred nanometers to well over 1 micron in thickness.

Spin-coated films were also produced by mixing the polymeric germanium precursor solution with the surfactant and spin-coating films from this mixture. In order to keep the this solution homogenous, no external oxidizing agent was added to this precursor solution, as the addition of any acid eventually cause a powder to precipitate. The films produced in this way are continuous and the thickness is tune by the speed at which they were spin-coated. The solvent used is ethylenediamine with a boiling point of 120 ºC. To gently remove this solvent, films were dried at 60 ºC under vacuum for 30 minutes to avoid washing away the material in the following steps.

In order to produce films that can be made porous by surfactant removal, the anionic Ge polymer must be fully reduced to zero valent germanium. We accomplish this again, by soaking the fully formed films in a solution of ammonium bromide which serves both as an oxidizing agent and as a H^+ donor to passivate any dangling anionic bonds on the Ge surface.

$$(Ge_9)_n^{2-} + 2H^+ \rightarrow a\text{-Ge:H} + H_2$$

The films are also given a final rinse in HF to completely saturate the surface with H-bonds. One advantage of these two methods is that we are not limited by the substrate as the films can be transferred or spin-coated onto different types of substrates, giving us a large range of possibilities depending on the application that we are going to use.

2.2.2 Structural characterization: Low angle XRD (figure 2.1) was used to characterize the nanoscale periodicity of these nanoporous materials. Figure 2.1a shows diffraction for a porous interface-nucleated

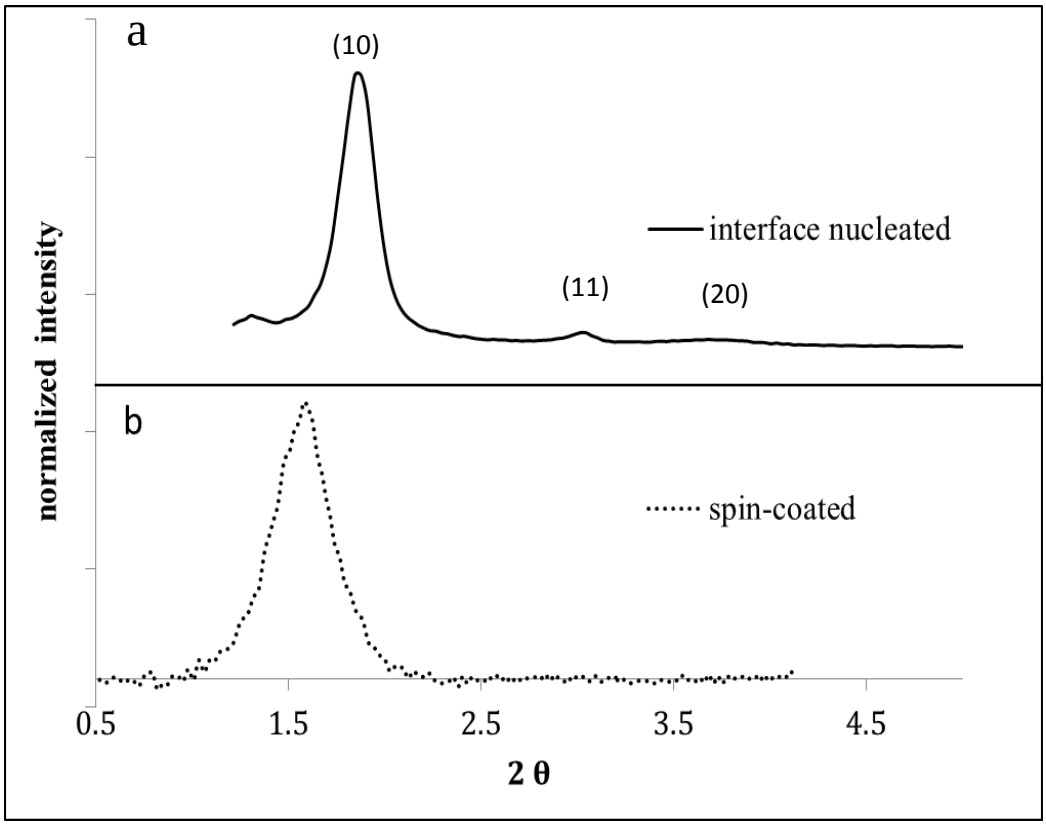

Figure 2.1. XRD showing traditional pattern for a mesoporous interface-nucleated Germanium film, three peaks can be seen which can be indexed to a hexagonal pattern with a d spacing of 4.7 nm (a) XRD pattern for a mesoporous spin-coated film the peak at $2\theta = 1.6$ corresponds to a repeat distance of 4.2 nm typical of CTEAB micelles templated materials.

film. The 3 peaks are in a 1:√ 3 : 2 ratio which can be indexed to the p6mm hexagonal phase indicating that a hexagonal honey-comb structure was formed by assembly of cylindrical micelles with the anionic Ge polylmer. The film shows a $d_{(10)}$ repeat distance of 4.7 nm which corresponds to a hexagonal lattice constant of a = 5.4 nm. Figure 2.1b shows a pattern for a porous spin-coated film. This sample shows a single peak at $2\theta = 1.6°$ which corresponds to a repeat distance of 5.5 nm. While the precise nanoscale architecture cannot be determined from the diffraction in figure 1b, the peak position is consistent with a partly disordered honeycomb structured material synthesized using Zintl cluster precursors and surfactants such as CTEAB (need a ref to back up this statement). Even though both methods produced ordered or partly ordered films, the primary d-spacing for each sample is not the same. Variations are likely due both to differences in the extent of order in the films, and to differences in the Ge oxidation state, and thus the density of the inorganic Ge walls. Interface-nucleated films clearly show a more organized structure due to the slow reaction conditions. Spin-coated films, while displaying some nanoscale periodicity, form quickly without extensive Ge crosslinking and so have many kinetic limitations on the nanoscale periodicity that can form.

Scanning electron microscopy images of both interface nucleated and spin coated films were taken to confirm continuity and thickness of the films. Figure 2.2 shows cross-section, as well as a top down view images of interface-nucleated films. The film thickness can be controlled by the time the film is allowed to grow, varying from a few hours to well over 1 day. Figure 2.2a shows a film grown for 1 hr with a thickness of 300 nm. This can be compared to figure 2.2b, which shows a film that was allowed to grow for 24 hr, producing a film with a thickness of 1500 nm. Figure 1c shows a top down view of the thin film and figure 2.2d shows a

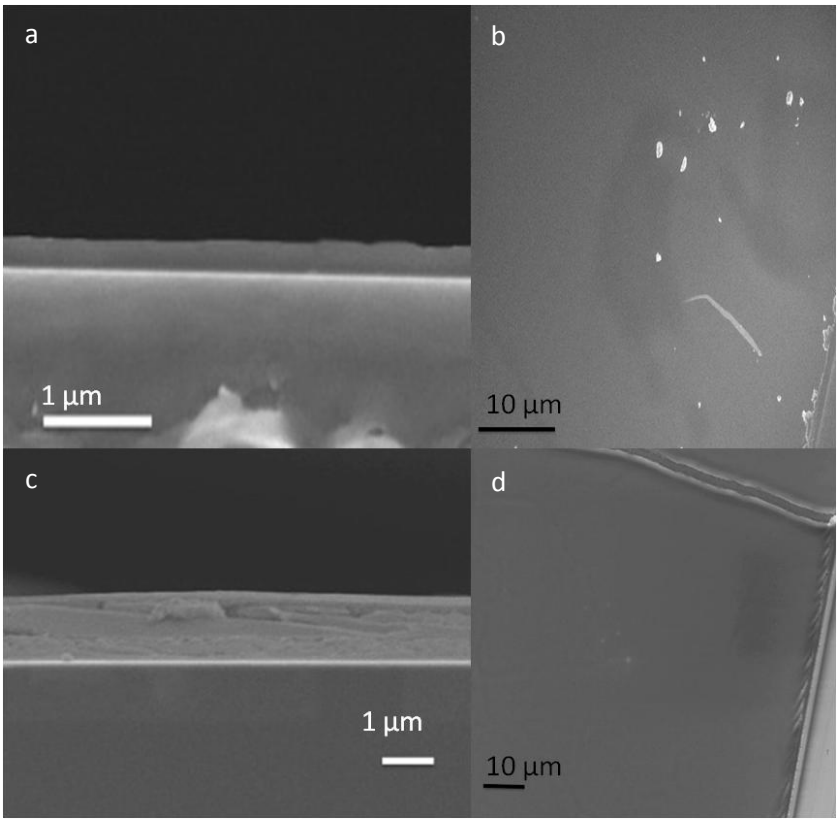

Figure 2.2. Scanning Electron Microscope images showing variation in the thickness from an interface-nucleated Germanium film. (a and c) same films in a and c top down view to show that the films are continuous with no visible cracks at the micron scale (b and d)

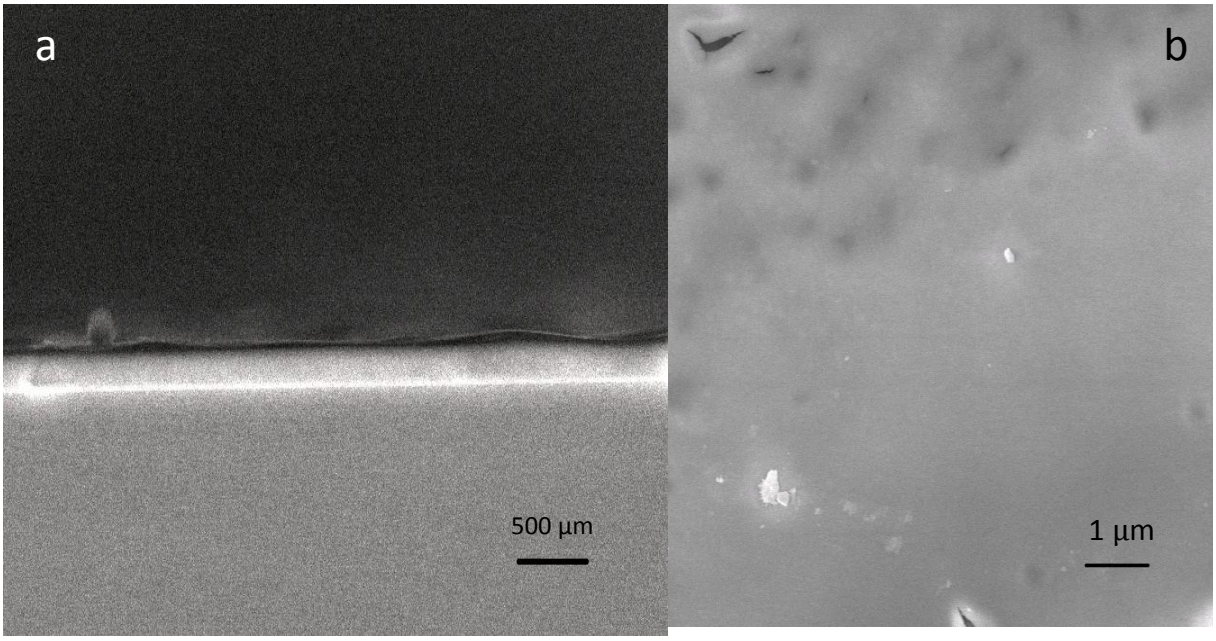

Figure 2.3. Scanning Electron Microscope images showing a spin-coated germanium film side view (a) and top down view to confirm the film is continuous (b)

top down view of the thicker film, in both cases the films are continuous and homogeneous in thickness.

The thickness of the spin-coated films cannot be controlled over such a large range because the solutions used to deposit the films are not highly viscous and ethylenediamine is not a highly volatile solvent. As a result, maximum film thicknesses are limited by the slowest spin speed that produces homogeneous films. Figure 2.3a shows a cross-sectional view of a spin-coated film with a thickness of 300 nm. These films also show good continuity, as can be seen from figure 2.3b.

To confirm that we have produced elemental germanium in these nanoporous films, X-ray photoelectron spectroscopy (XPS) was used. Figure 2.4a shows XPS data for a spin-coated film Ge film. The specra shows only one major peak near 29 eV, which corresponds to neutral germanium.[23] There is a small shoulder at higher binding energy indicating the presence of some oxidized germanium which can most likely be attributed to a very thin layer of germanium oxide formed on top due to the very reactive precursor. Figure 2.4b shows the XPS spectra of an interface-nucleated film also with the major peak at 29 eV indicating that the film is dominantly zero valent neutral germanium. Again a small shoulder is found at higher binding energies, indicating a small amount of of partly oxidized germanium. For both of these films, the fraction of unoxidized germanium is over 70%. Since these films are porous, they should have a very high surface area and so we would expect them to oxidize easily. It is not clear, however, if the oxidation arises from imperfect conditions in the nitrogen filled glove box where the films were synthesized, or during exposure upon transfer to the XPS.

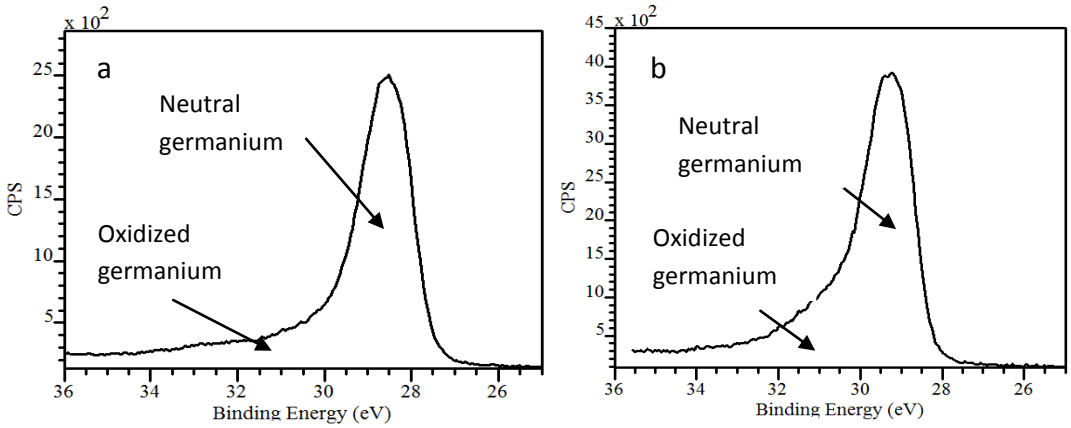

Figure 2.4. X-Ray photoelectron spectroscopy of a germanium film showing the 3d peak for a spin-coated film (a) and for an interface-nucleated film (b). In both cases the data shows mostly germanium in its neutral state.

2.2.3 Porosimetry measurements: While the existence of low angle diffraction peaks suggest that we have created a nanoporous germanium architecture, that porosity must be directly measured to ensure that pore spaces are both present and accessible to the environment. Here we used ellipsometric-porosimetry, a recently developed technique that is used to determine porosity of thin films and to analyze the porosity of composites.[43] Figure 5a shows an adsorption-desorption isotherm, using toluene as the adsorbate[43–45], or a mesoporous interface-nucleated germanium film. The film is found to exhibit a typical type IV isotherm.[46] The hysteresis present at a relative pressure of ~0.4 is indicative of a mesostructured material with open porosity. The hysteresis observed is not typical of cylindrical pores as there exist no cages and necks, however we believe that in our case the hysteresis is produced from a vertical shrinkage in the film, producing ellipsoidal rather than cylindrical pores. The isotherm also shows a material with a 20% pore volume which makes this film a reasonable candidate for adsorption based applications. For cylindrical pores BJH analysis assumes one pore size from adsorption. A Kelvin model fit to the isotherm produces a pore size distribution for the pores centered at 5.3 nm, as shown in Figure 5b. From diffraction the peak position of this film shows a single peak at $2\theta = 1.7\ ^\circ$ which corresponds to a repeat distance of 5.2 nm and a lattice parameter of 6 nm. Using and average size of 5.2 nm pores from porosimetry; we would obtain a wall thickness less than 0.8 nm. Assuming we have ellipsoidal pores, however, this wall thickness is underestimated.

We were not able to obtain meaningful data for porosimetry on spin-coated films. The spin-coated films that were measured very show little porosity. We can offer two explanations for this issue, one is that the surfactant is not fully removed by the oxidation and washing treatment

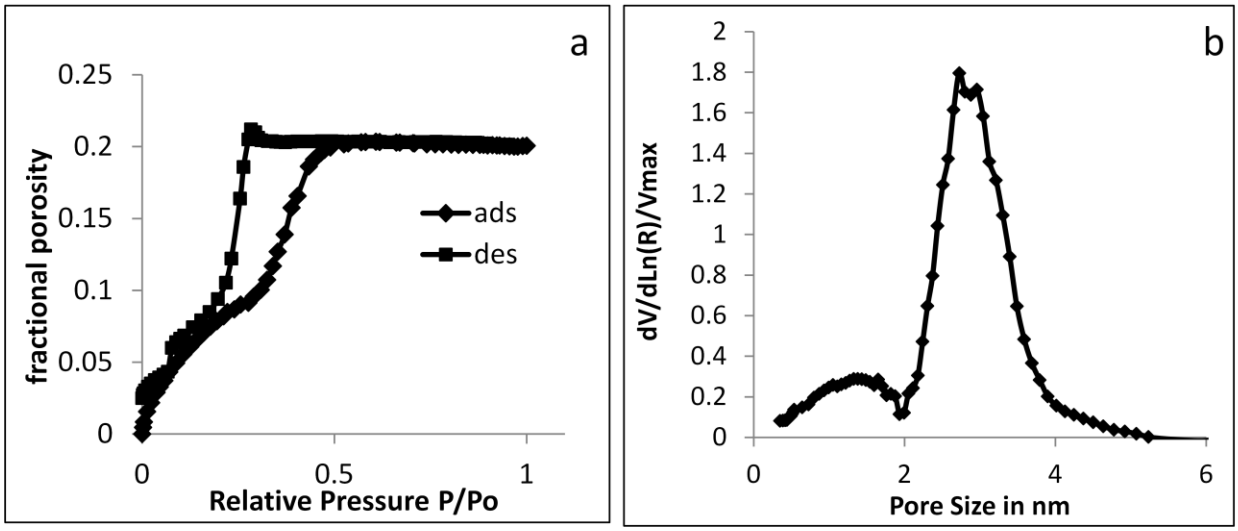

Figure 2.5. Toluene adsorption-desorption isotherm showing characteristic behavior for a mesoporous Interface-grown Germanium film (a) Pore size distribution data obtained from the adsorption part of the isotherm for a mesoporous Interface-grown Germanium film (b)

therefore blocking most of the accessible porosity, or it could also be because the top of the film is sealed in the spin-coating process and the pores are not accessible to the toluene.

2.3 Conclusions

In this work we explore two different methods to produce surfactant template germanium thin films. Solvent/vapor interface-nucleated films formed very slowly by addition of an oxidizing agent. The thickness of these films was controlled based on growth time, and films between 100 nm and 1.5 μm could be produced while maintaining a continuous ordered mesostructure. Spin-coated films were also made from similar, but less oxidized precursor solution. Our results indicate that interface-nucleated films are more ordered than spin-coated films, due to the slower rate assembly, and show higher porosity. However, spin-coating has the advantage that it is easier to produce homogeneous larger area films.

In this work we accomplished the synthesis of porous semiconducting germanium films using two methods that resemble sol-gel chemistry expanding the chemistries to non-oxide films with nanoscale order that have the possibility of being integrated into energy conversion devices, demonstrating a facile pathway to make porous semiconducting films.

2.4 Experimental

2.4.1 Materials: The following chemicals were purchased and used as received: Germanium powder (99.9% Alfa Aesar), Potassium metal (99.9% Afa Aesar) Ammonium Bromide (99.9% Alfa Aesar), Bomohexadecane (98% Aldrich), Triethylamine (96% Aldrich), Ethelene Diamine and Acetonitrile were distilled under Nitrogen using standard schlenk line techniques.

All procedures were carried out under inert atmosphere using standard glove box techniques.

2.4.2 Synthesis of germanium Zintl Cluster: K_4Ge_9 was made using a previously developed[32] solid state method. In a typical synthesis stoichiometric amounts of germanium and potassium were mixed and alloyed at 300 ºC for 1 hr. The mixture was then heated to 850 ºC in a sealed ampule under inert atmosphere for 2 hrs to produce the K_4Ge_9 powder, which was then dissolved in ethylene diamine to make a 0.03 M solution. This solution is the precursor solution used to make every film.

2.4.3 Interface nucleated films: 2 mL of the K_4Ge_9 precursor solution was combined with 2mL of 0.3M Cetyltriethylammonium Bromide dissolved in ethylene diamine at 40°C. This mixture was allowed to come to equilibrium and 0.1 mL of 0.02 M NH_4Br was added to initiate the oxidation process from Ge_9^{4-} to the more polymeric species Ge_9^{2-} allowing the co-assembly process of zintl germanium with the surfactant to take place. Once the acid was added the solution was left undisturbed until a film formed on the surface of the solution. These films were carefully picked up using any type of very clean substrate; we chose to use polycrystalline silicon.

2.4.4 Spin-Coated thin-films 2 mL of the K_4Ge_9 precursor solution combined with 2mL of 0.3M Cetyltriethylammonium Bromide dissolved in ethylenediamine at 40ºC. This mixture was spin-coated onto clean polar substrates using an evaporation-induced self-assembly process.

In both cases, the surfactant self-assembles to form micelles in solution and by electrostatic attraction the anionic germanium precursor assembles around the surfactant to yield a mesostructured organic/inorganic composite.

Both types of films were given the same post-treatment to remove the surfactant. In each case the films were heated to 60 °C for 1 hour to strengthen the bonds. They were washed in a 0.3M NH_4Br solution in ethylenediamine to fully oxidize the germanium to neutral germanium, following by a wash in acetonitrile to remove any leftover surfactant on the film. To get rid of any surface oxidation the films were briefly submerged in 4%HF in ethanol right before doing any measurements.

2.5 Methods

Scanning electron microscopy (SEM) images were obtained using a JEOL model 6700F electron microscope with beam energy 5 kV, and with a Zeiss Gemini Ultra-55 Analytical electron microscope with beam energy 5 kV. Conventional X-ray diffraction measurements were carried out on a Panalytical XPert PRO MPD diffractometer, with $Cu_{K\alpha}$ radiation. Ellipsometric porosimetry was performed on a PS-1000 instrument from Semilab using toluene as the adsorbate. A UV–visible CCD detector adapted to a grating spectrograph analyzes the signal reflected by the sample. The light source is a 75 W Hamamatsu Xenon lamp and measurements were performed on the spectral range from 1.24-4.5 eV. Data analysis was performed using the associated SEA software. XPS analysis was performed using a Kratos Axis Ultra DLD with a monochromatic (K_α radiation) source. The charge neutralizer filament was used to control charging of the sample. A 20 eV pass energy was used with a 0.05 eV pass energy. Scans were calibrated using the C 1s peak shifted to 294.8 eV.

2.7 References

1. Adhikari, H., Marshall, A. F., Chidsey, C. E. D. & McIntyre, P. C. Germanium nanowire epitaxy: shape and orientation control. *Nano Lett.* **6,** 318–23 (2006).

2. Kodambaka, S., Tersoff, J., Reuter, M. C. & Ross, F. M. Germanium nanowire growth below the eutectic temperature. *Science* **316,** 729–32 (2007).

3. Chang, S.-S. & Hummel, R. . Comparison of photoluminescence behavior of porous germanium and spark-processed Ge. *J. Lumin.* **86,** 33–38 (2000).

4. Kartopu, G., Sapelkin, a. V., Karavanskii, V. a., Serincan, U. & Turan, R. Structural and optical properties of porous nanocrystalline Ge. *J. Appl. Phys.* **103,** 113518 (2008).

5. Jing, C. *et al.* Fabrication and characteristics of porous germanium films. *Sci. Technol. Adv. Mater.* **10,** 065001 (2009).

6. Shieh, J., Chen, H. L., Ko, T. S., Cheng, H. C. & Chu, T. C. Nanoparticle-Assisted Growth of Porous Germanium Thin Films. *Adv. Mater.* **16,** 1121–1124 (2004).

7. Zhao, D. *et al.* Continuous Mesoporous Silica Films with Highly Ordered Large Pore Structures. *Adv. Mater.* **10,** 1380–1385 (1998).

8. Lu, Y., Ganguli, R., Drewien, C. & Anderson, M. Continuous formation of supported cubic and hexagonal mesoporous films by sol–gel dip-coating. *Nature* **389,** 651–655 (1997).

9. Soler-Illia, G. & Crepaldi, E. Block copolymer-templated mesoporous oxides. *Curr. Opin. colloid …* **8,** 109–126 (2003).

10. Edler, K. J. & Yang, B. Formation of mesostructured thin films at the air-liquid interface. *Chem. Soc. Rev.* **42,** 3765–76 (2013).

11. Fıçıcılar, B., Bayrakçeken, A. & Eroğlu, İ. Effect of Pd loading in Pd-Pt bimetallic catalysts doped into hollow core mesoporous shell carbon on performance of proton exchange membrane fuel cells. *J. Power Sources* **193,** 17–23 (2009).

12. Liong, M. *et al.* Multifunctional inorganic nanoparticles for imaging, targeting, and drug delivery. *ACS Nano* **2,** 889–96 (2008).

13. Riley, A. E., Korlann, S. D., Richman, E. K. & Tolbert, S. H. Synthesis of semiconducting thin films with nanometer-scale periodicity by solution-phase coassembly of zintl clusters with surfactants. *Angew. Chem. Int. Ed. Engl.* **45,** 235–41 (2005).

14. Rauda, I. E. *et al.* Nanoporous semiconductors synthesized through polymer templating of ligand-stripped CdSe nanocrystals. *Adv. Mater.* **25,** 1315–22 (2013).

15. Rauda, I. E. *et al.* General method for the synthesis of hierarchical nanocrystal-based mesoporous materials. *ACS Nano* **6,** 6386–99 (2012).

16. Shingubara, S. Fabrication of Nanomaterials Using Porous Alumina Templates. *J. Nanoparticle Res.* **5,** 17–30 (2003).

17. Z-R. Tian, E. al. Manganese Oxide Mesoporous Structures: Mixed-Valent Semiconducting Catalysts. *Science (80-.).* **276,** 926–930 (1997).

18. Shang, H. *et al*. Electrical characterization of germanium p-channel MOSFETs. *IEEE Electron Device Lett.* **24,** 242–244 (2003).

19. Kittel, C. *Introduction to Solid State Physics*. (John Wiley & Sons, et al., 1986).

20. Liu, S., Lee, S., Member, S. & Chern, M. Hydrogenated Amorphous Silicon-Germanium PIN. *IEEE Trans. Electron Devices* **48,** 1564–1567 (2001).

21. Kartopu, G. Simultaneous micro-Raman and photoluminescence study of spark-processed germanium: Report on the origin of the orange photoluminescence emission band. *J. Appl. Phys.* **95,** 3466 (2004).

22. Carroll, M. S., Verley, J. C., Sheng, J. J. & Banks, J. Roughening transition in nanoporous hydrogenated amorphous germanium: Roughness correlation to film stress. *J. Appl. Phys.* **101,** 063540 (2007).

23. Chandrasekharan, N. & Sevov, S. C. Anodic Electrodeposition of Germanium Films from Ethylenediamine Solutions of Deltahedral Ge[sub 9][sup 4−] Zintl Ions. *J. Electrochem. Soc.* **157,** C140 (2010).

24. Langa, S., Christophersen, M., Carstensen, J., Tiginyanu, I. M. & Föll, H. Electrochemical pore etching in Ge. *Phys. Status Solidi* **195,** R4–R6 (2003).

25. Scavetta, E. *et al.* Nanoporous Ge coated by Au nanoparticles for electrochemical application. *Electrochem. commun.* **30,** 83–86 (2013).

26. Kauzlarich, S. M. Zintl Compounds. (2006). doi:10.1002/0470862106.ia262

27. Birdwhistell, T. & Klein, C. Synthesis and crystal structures of the layered I–III–V Zintl phases, K4In4X6, where X= As, Sb. *J. Mater. ...* **1,** 555–558 (1991).

28. Corbett, J. Diverse naked clusters of the heavy main-group elements. Electronic regularities and analogies. *Struct. Electron. Paradig. Clust. ...* **87,** (1997).

29. Sevov, S. C. & Goicoechea, J. M. ReViews Chemistry of Deltahedral Zintl Ions. *Organometallics* **9,** 5678–5692 (2006).

30. Korlann, S. D., Riley, A. E., Kirsch, B. L., Mun, B. S. & Tolbert, S. H. Chemical tuning of the electronic properties in a periodic surfactant-templated nanostructured semiconductor. *J. Am. Chem. Soc.* **127,** 12516–27 (2005).

31. Riley, A. E. & Tolbert, S. H. Synthesis and characterization of tin telluride inorganic / organic composite materials with nanoscale periodicity through solution-phase self-assembly : a new class of composite materials based on Zintl cluster self-oligomerization. *Res. Chem. Intermed* **33,** 111–124 (2007).

32. Sun, D. *et al.* Hexagonal nanoporous germanium through surfactant-driven self-assembly of Zintl clusters. *Nature* **441,** 1126–30 (2006).

33. Armatas, G. S. & Kanatzidis, M. G. High-Surface-Area Mesoporous Germanium from Oxidative Polymerization of the Deltahedral [Ge9]4– Cluster: Electronic Structure Modulation with Donor and Acceptor Molecules. *Adv. Mater.* **20,** 546–550 (2008).

34. Armatas, G. S. & Kanatzidis, M. G. Mesoporous compound semiconductors from the reaction of metal ions with deltahedral [Ge9]4- clusters. *J. Am. Chem. Soc.* **130,** 11430–6 (2008).

35. Brown, A., Holt, S., Dam, T., Trau, M. & White, J. Mesoporous silicate film growth at the air-water interface direct observation by X-ray reflectivity. *Langmuir* **7463,** 6363–6365 (1997).

36. Edler, K. J., Brennan, T., Roser, S. J., Mann, S. & Richardson, R. M. Formation of CTAB-templated mesophase silicate films from acidic solutions. *Microporous Mesoporous Mater.* **62,** 165–175 (2003).

37. Fernandez-Martin, C., Edler, K. J. & Roser, S. J. Humidity and temperature effects on CTAB-templated mesophase silicate films at the air-liquid interface. *Langmuir* **20,** 10679–84 (2004).

38. Ruggles, J. L., Holt, S. a., Reynolds, P. a. & White, J. W. Synthesis of Silica Films at the Air/Water Interface: Effect of Template Chain Length and Ionic Strength. *Langmuir* **16,** 4613–4619 (2000).

39. Yang, H., Coombs, N., Sokolov, I. & Ozin, G. Free-standing and oriented mesoporous silica films grown at the air–water interface. *Nature* **381,** 589–592 (1996).

40. Tolbert, S., Schäffer, T. & Feng, J. A new phase of oriented mesoporous silicate thin films. *Chem. …* **4756,** 1962–1967 (1997).

41. Sevov, S. & Goicoechea, J. Chemistry of deltahedral zintl ions. *Organometallics* **9,** 5678–5692 (2006).

42. Karttunen, A. J., Fässler, T. F., Linnolahti, M. & Pakkanen, T. a. Two-, one-, and zero-dimensional elemental nanostructures based on Ge(9)-clusters. *Chemphyschem* **11,** 1944–50 (2010).

43. Boissiere, C. *et al.* Porosity and mechanical properties of mesoporous thin films assessed by environmental ellipsometric porosimetry. *Langmuir* **21,** 12362–71 (2005).

44. Baklanov, M. R., Mogilnikov, K. P., Polovinkin, V. G. & Dultsev, F. N. Determination of pore size distribution in thin films by ellipsometric porosimetry. *J. Vac. Sci. Technol. B Microelectron. Nanom. Struct.* **18,** 1385 (2000).

45. Eslava, S. *et al.* Characterization of a molecular sieve coating using ellipsometric porosimetry. *Langmuir* **23,** 12811–6 (2007).

46. Gregg, S. J.; Sing, K. S. W. *Adsorption, Surface Area, and Porosity*.

CHAPTER 3

Nanoporous Semiconductors Synthesized Through Polymer templating of Ligand-Stripped CdSe Nanocrystals

3.1 Introduction

The push to develop new functional materials for both catalysis and energy related applications has produced a surge of interest in producing mesoporous architectures from functional materials. When nanostructured materials are made mesoporous with an open and interconnected pore structure, the surface area of that material becomes accessible to the solvent environment, allowing materials to be optimized for specific chemical transformations and redox reactions. Examples of processes that could benefit from functional mesoporous materials vary from catalysis and photocatalysis to solar energy harvesting and electrochemical charge storage.[1-7]

One particularly exciting family of systems for many of these applications, particularly those involving absorption of solar radiation, is main-group semiconductor nanocrystals. These materials have been shown to exhibit a broad range of exciting optical and electronic properties, making them suitable for integration into a diverse family of devices.[8-11] The literature includes a vast number of synthetic routes to produce stable semiconductor nanocrystals with controlled compositions, shapes, and sizes.[12-18] In general, these syntheses leave the surface of nanocrystals capped with organic ligands that act to stabilize the nanocrystals and prevent aggregation. Monodisperse nanocrystals of this type can be crystallized into highly periodic arrays, containing many different types of nanocrystal.[19,20] While compositionally and topologically diverse materials can be created, the resulting materials are often neither conductive nor porous because of the surface passivating groups. In many cases, removal of these surface stabilizing groups

leads to undesirable agglomeration or etching.[21,22] Conductivity problems have been partially resolved by depositing a dense film of nanocrystals, followed by a ligand-exchange with a very small, organic ligand.[23-25] Materials have also been synthesized with inorganic ligands that can be thermally processed to produce nanocrystals embedded in a conductive matrix.[26-29] While these methods can be used to solve the conductivity problem, the resulting materials are mostly dense and so they do not provide solvent access to the tremendous intrinsic interfacial area of these nanocrystal based materials.

Recently, some very beautiful sol-gel methods for assembling colloidal nanocrystals of various semiconductors into porous aerogels have been reported.[30-33] This sol-gel method has been used to prepare highly porous aerogels from various chalcogenide semiconductor nanocrystals, including CdSe,[30] CdTe,[31,32] CdS,[30] PbS,[30] ZnS[30] and Ag_2Se[33]. These aerogels have been shown to exhibit typical absorption of quantum-confined semiconductors. These sol-gel method produce the desirable combination of high surface area and open porosity, although the pores are fairly large with a broad pore size distribution that ranges from mesopores to macropores (~2-120 nm).[32,33] For the preparation of such aerogels, an efficient and specific surface reaction is also usually necessary in order to gelate the colloids; to date the method has only been applied to chalcogenide based systems. As a result, while this aero-gel work marks a major advance in the field, there is still a need for a general method for building mesoporous semiconductor, particularly in thin film format, with smaller and more homogeneous porosity from a broader range of semiconductor nanocrystals.

While aerogels like those described above may be the most familiar form of porous materials, another route to produce mesoporous materials is through solution-phase self-assembly of soluble building blocks, typically molecular inorganic precursors, with a structure

directing template such as amphiphilic surfactants or block copolymers.[34-39] In many cases, sol-gel chemistries are utilized, producing oxide-based inorganic materials through an evaporation-induced self-assembly process (EISA).[40-44] In this simple approach, the organic template forms micelles, and upon evaporation of the solvent, the inorganic precursors co-assemble with the micelles and self-organize into an organic-inorganic composite. The template is then thermally decomposed, usually in air, to yield a mesoporous architecture.

In recent years, the utilization of large diblock copolymers as templating agents has led to the synthesis of porous materials with crystalline walls that exhibit large mesopores with good solvent accessibility to the pore volume.[45-50] Unfortunately, the surface area of these large pore materials tends to be fairly modest as wall thicknesses are in the 10-20 nm range, rather than the 5 nm range. To address this problem, significant recent advances have been made in the synthesis of nanoporous materials from assembly of pre-formed nanocrystal building blocks into hierarchical mesoporous architectures.[5,51-56] Such materials combine the accessibility of large-pore materials, with the surface area of much smaller-pore systems. Nanocrystal-based nanoporous materials have now been made from systems as diverse as oxides, metals, and fluorides.[5,54-56] The one thing shared by all systems made to date, however, is the fact that they are air stable. This is because decomposition of the polymer template is generally carried out in oxidative conditions.

While there are many interesting applications for noble metal and oxide nanocrystal-based porous materials, the ability to assemble non-oxide nanocrystals, such as main-group semiconductors, into porous films would significantly broaden the spectrum of applications for these high surface area porous materials. In particular, applications such a solar energy harvesting and photocatalysis generally require mid-to-low band gap semiconductors, and these

are difficult to produce in oxide systems. However, as discussed above, semiconductor nanocrystals have organic surface ligands that make them unsuitable for polymer templating in polar solvents.

Huge strides have recently been made in solving these problems using soluble, ligand-free nanocrystals. A series of recent reports indicate that it is now possible to strip native ligands off the surface of nanocrystals to produce bare, stable nanocrystals that are soluble in polar organic solvents.[57-59] Such nanocrystals can be easily processed into conductive films.[60] More importantly, we have recently demonstrated that these ligand-free nanocrystals can be templated to form high surface area nanoporous architectures using block copolymer templating.[51,52] While our previous work was a major step toward realizing materials that combine electrical connectivity, high surface area, and open porosity, the materials were still limited by one major constraint – only oxidatively stable materials could be produced as the polymer template was thermally degraded in air at elevated temperature.

In this work, we build from our previous nanocrystal templating results by extending this approach to oxidatively unstable materials. This work focuses on the synthesis of mesoporous materials from ligand-stripped cadmium selenide (CdSe) nanocrystals as a model system, but the method should be general to the broad family of main group semiconductor nanocrystals. We specifically utilize recently developed chemistries that use Meerwein's salt (Et_3OBF_4) to gently strip ligands from the surface of CdSe nanocrystals.[59] The ligand-stripped CdSe nanocrystals are then combined with a block copolymer that can be thermally decomposed to volatile species under inert conditions. We show that mesoporous CdSe-based materials retain their semiconducting properties, including quantum confined excitonic absorption and modest carrier mobilities. These standard properties are then complemented by new features, such as

homogeneous open porosity and high surface area. This work thus builds a bridge between the structural complexity of templated porous materials, and the electronic and optical complexity of semiconductor nanocrystals. While this work utilizes one of the most common semiconductor nanocrystals, CdSe, it is important to point out that nothing in the assembly methods used here takes advantage of CdSe specific chemistries. Because the assembly process itself is independent of the synthesis and reactivity of the CdSe itself, our approach should be applicable across the wide range of semiconductor nanocrystals which can be prepared as ligand-free dispersions using the Meerwein's salt process.

3.2 Results and Discussion

3.2.1 Synthesis of the nanocrystal-based films

As discussed above, in order to template nanocrystals, they must be stripped of their native ligands in order to form stable dispersions in polar solvents. Here, we utilize previously reported methods to produce ligand-stripped or "bare" CdSe nanocrystals.[59,61] Briefly, oleate-passivated CdSe (CdSe-OA) nanocrystals were synthesized according to literature procedures using the automated synthesis robot, WANDA.[62] In a typical ligand-exchange process, a solution of Et_3OBF_4 in acetonitrile (MeCN) is added to CdSe-OA nanocrystals dispersed in hexane, forming a biphasic solution. The reaction mixture is vortexed, resulting in oleate ligand stripping with subsequent charge stabilization by BF_4^- anions. The resultant "bare" nanocrystals are then washed and redispersed in dimethylformamide (DMF). Figure 3.1a shows a transmission electron microscope (TEM) image of CdSe nanocrystals after the ligand-exchange process with an average diameter of 4.1 ± 0.3 nm. The image shows that the nanocrystals are not agglomerated or fused together after Et_3OBF_4 treatment.[59,61] This is important, because to

effectively assemble nanocrystals into robust networks, they must be bare and individually dispersed. Previous work has shown that the size of a species that can be organized by a block copolymer is directly related to the molecular weight of the polymer itself.[53] The modest sized polymer used here cannot organize a large nanocrystal or aggregates of nanocrystals (which are equivalent). Bare nanocrystals are required because the nanocrystals must fuse into a robust network at temperatures below the thermal degradation point of the polymer template with minimal volume change.

Because CdSe can oxidize to form both CdO and SeO_2, another important element for templating CdSe nanocrystals is to use a polymer template that can be decomposed under non-oxidizing conditions. Here, we use the diblock copolymer poly(butylene oxide)-*block*-poly(ethylene oxide), (PBO(5000)-*b*-PEO(6500), M_n = 11500 g mol^{-1}), which has ether functional groups along the backbone for both blocks. This ether functionality provides an oxygen source during thermal degradation of the polymer that leads to the production of volatile species from both blocks. Unlike typical pluronic surfactants, however, which are based on combination of PEO with poly(propylene oxide),[38,40] the hydrophobic contrast between PBO and PEO is quite good and so strong segregation of blocks is observed in a range of polar organic solvents. Figure 3.1b shows a thermal gravimetric analysis (TGA) trace for PBO-*b*-PEO heated under argon. The data confirm that the polymer is fully decomposed by 350 °C in the absence of oxygen. This is important because chemically unstable materials, like CdSe nanocrystals, are unable to withstand oxidizing environments.

In a typical synthesis of CdSe mesoporous films, a dispersion of ligand-stripped CdSe nanocrystals in DMF was combined with polymer, also dissolved in DMF. From this solution, films were prepared by spin-coating onto polar substrates, followed by thermal treatment to 400

°C under argon. Figure 3.2 shows (a) low- and (b) high-magnification scanning electron microscope (SEM) images of CdSe nanocrystal-based mesoporous films with an average thickness of 120 ± 20 nm, as determined by profilometry measurements. The films show the appearance of locally disordered mesopores. As discussed above, the size of the polymer determines the size of nanocrystals it can assemble; therefore, it is likely that a larger polymer would produce more ordered pores.[53] It is important to note, however, that while the films do not show periodic pores, they do demonstrate macroscopic homogeneity of the mesopores, with the mesopores having an average diameter of 15 ± 2 nm, judging by SEM. Moreover, the films are crack-free with visibly open porosity at the film surface. A closer look at Figure 3.2b shows the presence of individual nanocrystals comprising the pore-walls. The agglomerated nanocrystals in the walls give rise to micropores, which significantly increase the surface area of these materials compared to materials with dense walls. Figure 3.2 also shows (c) low- and (d) high-magnification SEM images of a CdSe mesoporous film that was prepared by drop-casting, leading to a film that is 1.2 ± 0.2 μm thick. The thick films are also crack-free, show open mesopores at the surface with an average diameter of 15 ± 2 nm, and have individual nanocrystals embedded in the pore-walls.

3.2.2 Structural and Optical Characterization of the Nanocrystal-based Films

To determine the crystal structure of both CdSe nanocrystals and the templated mesoporous CdSe films, two-dimensional wide angle X-ray scattering (2D-WAXS) measurements were performed on beamline 11-3 at the Stanford Synchrotron Radiation Laboratory (SSRL). 2D-WAXS measurements were carried out in reflection mode with the incoming beam at or near grazing incidence. Here we define β as the angle between the X-ray beam and the plane of the substrate. Figure 3.1c shows WAXS patterns for CdSe nanocrystals

after ligand-exchange with Et_3OBF_4 (A) and mesoporous film of CdSe nanocrystals after templating with PBO-*b*-PEO (B), collected at $\beta = 2.0°$. The main peaks for both samples can be indexed to the hexagonal or wurtzite phase of CdSe (JCPDS reference card no. 02-0330). Deviations in peak intensities from the ideal wurtzite structure, however, indicate some stacking faults and structure that is actually intermediate between wurtzite and the related cubic zinc blende structure. The pattern for the ligand-exchanged nanocrystals (A) shows significant peak broadening, consistent with their small size. Domain sizes calculated by Scherrer analysis of the peak widths were found to be ~5 nm. This is also consistent with the diameter observed in TEM (Figure 3.1a). Some additional small peaks belonging to BF_4^- salts ($NOBF_4$ and NO_2BF_4) are observed and these are marked with an asterisk (JCPDS reference cards nos. 17-0252 and 17-0253). These extra peaks disappear after thermal degradation of the polymer to leave behind the pure wurtzite phase of CdSe (B).

Pattern B shows diffraction for the mesoporous CdSe films. For this sample, the peak intensities show more deviation from the ideal wurtzite structure, indicative of increasing zinc blende character. Analysis of the peak widths for the templated films gives a grain size of ~10 nm for the more intense and narrower peaks (i.e. (110) and (112)), and ~5 nm for the less intense and broader peaks (i.e. (102) and (103)). This observation can be explained by a distribution of nanocrystals – some that have fused to yield larger domains and some that did not grow in size during thermal treatments. It is usually difficult to see a distribution of nanocrystal sizes by X-ray diffraction because larger nanocrystals scatter much more strongly than small ones. In this case, however, the nanocrystals that grow in size apparently have more zinc blende character, which allows us to see the presence of the uncoarsened nanocrystals in the wurtzite peaks.[63] While this data does indicate that there is some grain growth during the thermal treatment, the

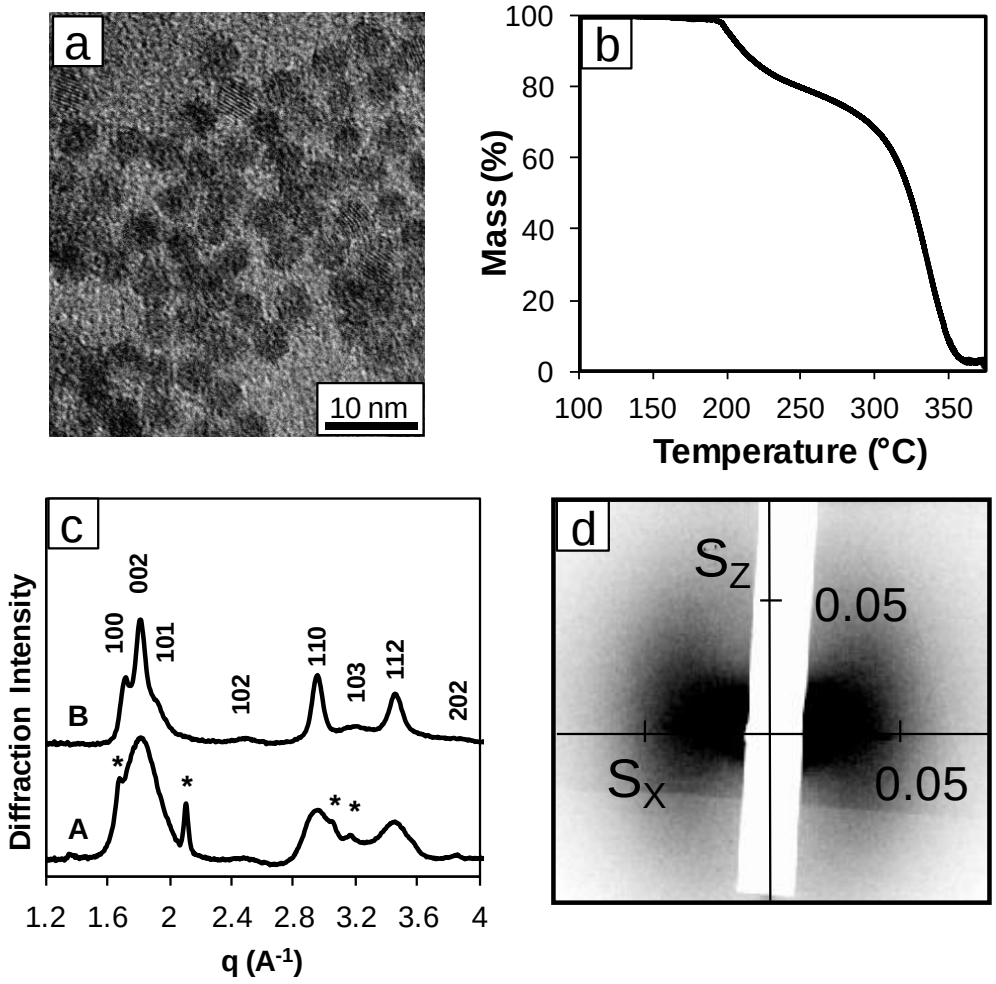

Figure 3.1. (a) TEM image of CdSe nanocrystals after treatment with Et_3OBF_4 . The nanocrystals are monodisperse and non-agglomerated. (b) TGA data for PBO-*b*-PEO at a constant heating rate of 1 °C min^{-1} under a flowing argon atmosphere. The data indicate that this diblock copolymer can be fully degraded under inert atmosphere by 350 ºC. (c) Wide angle XRD patterns obtained by integrating 2D-WAXS data collected on CdSe nanocrystals after the ligand-exchange process with Et_3OBF_4 (A) and after templating with PBO-*b*-PEO and thermal treatment to 400 °C to form a mesoporous CdSe nanocrystal-based film (B). Both before and after templating, the diffraction can be indexed to the wurtzite crystal structure of CdSe. Narrow

peaks marked with * correspond to organic salts used in the ligand-stripping process. (d) 2D-SAXS pattern obtained on a CdSe nanocrystal-based mesoporous film. The image shows strong in-plane scattering, indicative of a well-defined pore size, but no long range periodicity of the pores. Scattering vector *S* components are given in 1/nm.

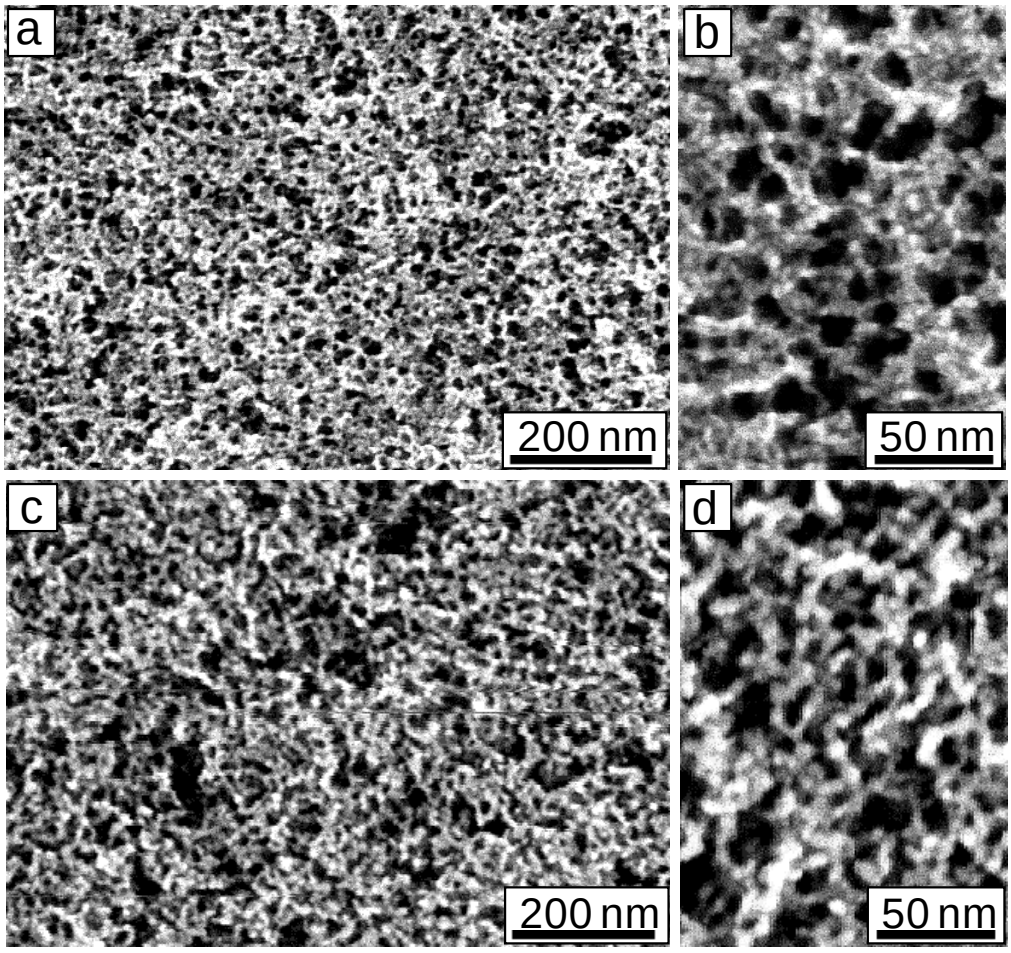

Figure 3.2. Top-view SEM images of CdSe nanocrystal-based mesoporous films templated with PBO-*b*-PEO. Parts (a) and (b) show low-magnification and high-magnification images, respectively, of films prepared by spin-coating. Parts (c) and (d) show low-magnification and high-magnification images, respectively, of films prepare by drop-casting. In both cases, both the larger black mesopores and the individual nanocrystals can be seen.

data also corroborates the SEM images in Figure 3.2a-d where individual nanocrystals that do not fully fuse can still be seen making up the pore wall. We also note that a comparison of the relative intensities around the diffraction rings for each peak in the raw 2-D data for both (A) and (B) indicates that the nanocrystals embedded in the pore walls are randomly oriented with respect to the substrate and there is no preferred or oriented growth during the thermal treatment.

Analysis of the templated films further made use of two-dimensional small-angle X-ray scattering (2D-SAXS) measurements performed on beamline 1-4 at SSRL, collected in reflection mode at a grazing angle of incidence, $\beta = 0.8°$. Figure 3.1d shows a 2D-SAXS pattern collected for PBO-*b*-PEO templated CdSe nanocrystals. Little out-of-plane diffraction is observed in the z-direction, but strong in-plane scattering maxima can be seen along the x-direction. Analysis of the observed scattering maxima corresponds to a lengthscale of 28 nm. This type of diffuse scattering is characteristic of a disordered or non-periodic material with homogenously sized pores. This repeat distance of 28 nm is also in reasonable agreement with the sum of the average pore diameter and wall thickness determined by SEM above.

The optical properties of the mesoporous CdSe films were investigated by absorption spectroscopy. Figure 3.3a shows UV-visible absorption spectra for oleate-passivated CdSe nanocrystals dispersed in hexane (black line), and CdSe nanocrystals after Et_3OBF_4 treatment dispersed in DMF (dashed black line), both plotted as normalized absorbance versus wavelength. The oleate-capped nanocrystals show a first exciton peak at 578 nm or 2.15 eV, which corresponds to a calculated diameter of ~3.8 nm.[64] The spectrum for the ligand-stripped nanocrystals shows very similar data with the first exciton peak at 573 nm or 2.16 eV, and a calculated diameter of ~3.7 nm.[64] The slight exciton peak shift after the ligand-exchange process may be attributed to differences in surface passivation by oxoanionic ligands versus DMF.

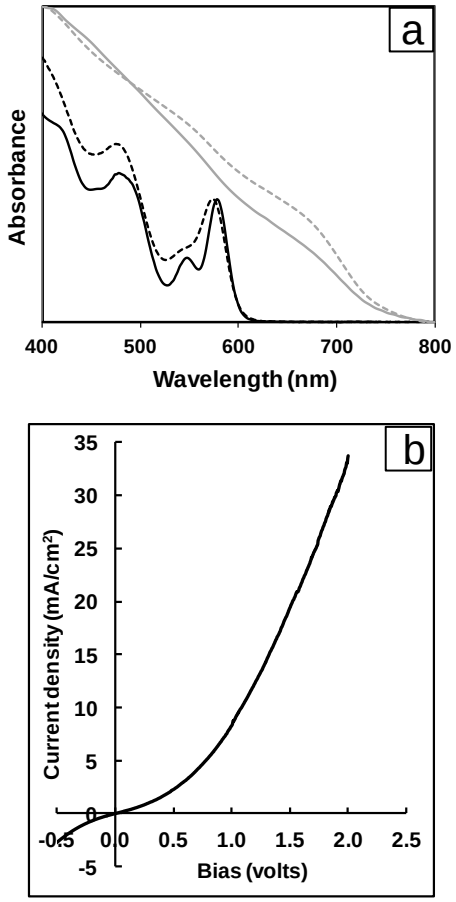

Figure 3.3. (a) UV-visible absorption spectra of CdSe nanocrystals in several environments. As-synthesized samples dispersed in hexane are indicated with a solid black line. Data collected on samples dispersed in DMF after ligand stripping with Et_3OBF_4 are indicated with a dashed black line. Data for a dense film of untemplated CdSe nanocrystals after ligand stripping are indicated by a dashed gray line. Data for a template mesoporous CdSe nanocrystal-based film are indicated by a solid gray line. All data is plotted as normalized absorbance versus wavelength. (b) Experimental current density-voltage curve for a CdSe nanocrystal-based mesoporous film demonstrating typical diodic behavior. A space-charge limited current model was utilized to calculate a carrier mobility of 10^{-4} cm^2 V^{-1} sec^{-1} from this data.

Figure 3.3a also shows absorption for a dense film of untemplated ligand-stripped CdSe nanocrystals (dashed grey line), and a mesoporous CdSe film (gray line). Both films were deposited onto glass heated to 400 °C under argon and data is plotted as normalized absorbance versus wavelength. The porous templated CdSe film was approximately 1.0 ± 0.1 μm. Very similar behavior is observed for both films, with bathochromic shifts of the exciton peak to ~675 nm or 1.84 eV for the dense film of untemplated CdSe and to ~680 nm or 1.82 eV for mesoporous templated CdSe are observed. The shifts may be explained by a combination of increases in the interparticle electronic coupling and real grain growth of the nanocrystals in both films.[65]

To better understand this data, it is worth noting that the room temperature bulk band gap for bulk wurtzite CdSe is 1.74 eV.[66] For both nanocrystal based films film, a tail of absorption and/or scattering are observed beyond this bulk band edge. The presence of both an excitonic peak and absorption near the bulk band edge is consistent with the 2D-WAXS data from figure 3.1c which shows the presence of both larger (10 nm, not quantum confined) and smaller (5 nm) domains after annealing. The optical data is also in agreement with the SEM images that show that the nanocrystals are fused together. Moreover, the data shows that thermal processing has the same effect on both templated and untemplated nanocrystals, demonstrating that the CdSe behavior does not change after making it mesoporous. Despite these optical changes, the templated film still shows a distinct size induced blue shift of the absorption, indicating that these nanoporous, nanocrystal-based films can successfully combine quantum confinement, high surface area, and porosity, a combination that could be beneficial for a range of light driven processes.

3.2.3 Compositional Characterization

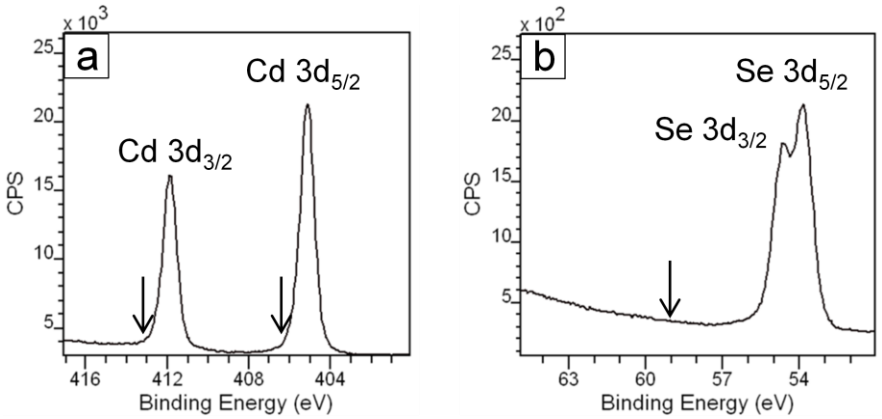

Figure 3.4. (a – b) XPS collected on a mesoporous CdSe nanocrystal-based film. (a) A high resolution spectrum of the Cd 3d core region shows peaks for the $3d_{3/2}$ and $3d_{5/2}$ core levels of Cd in CdSe. No peaks corresponding to CdO_x can be observed (arrows mark expected location). (b) A high resolution spectrum for Se 3d core region shows peaks for the $3d_{3/2}$ and $3d_{5/2}$ core levels of Se in CdSe. Again, no peaks corresponding SeO_2 can be observed (arrows mark expected location).

Compositional information on the templated CdSe films was determined from X-ray photoelectron spectroscopy (XPS) measurements. Figure 3.4a shows a high-resolution spectrum taken of the Cd 3d core region which contains two peaks corresponding to the $3d_{3/2}$ and $3d_{5/2}$ core levels. The positions of the peak for the Cd $3d_{3/2}$ and Cd $3d_{5/2}$ core levels are centered on binding energies of 411.9 and 405.2 eV, which are in good agreement with reported values of 411.93 and 405.13 eV for CdSe. [66,67] More importantly, the data shows that no oxidation of the Cd occurred, as evidenced by the complete absence of CdO_x peaks that typically appear as shoulders at slightly higher binding energies for both $3d_{3/2}$ and $3d_{5/2}$ core levels. The expected positions of the CdO_x $3d_{3/2}$ and $3d_{5/2}$ peaks, reported to be 413.08 and 406.30 eV,[67] are indicated on the figure with arrows. Figure 3.4b shows a similar high resolution spectrum of the Se 3d core region showing two peaks corresponding to $3d_{3/2}$ and $3d_{5/2}$ core levels centered at binding energies of 54.7 and 53.8 eV. These energies are again in agreement with literature values for Se $3d_{3/2}$ and $3d_{5/2}$ core levels in CdSe, reported as 55.07 and 54.18 eV.[66,67] Similarly, the spectrum shows the complete absence of an oxidized Se peak, which occurs at higher binding energy, reported at 59.0 eV for SeO_2.[67,68] The binding energy of CdSe, measured as the difference between the Cd $3d_{5/2}$ and Se $3d_{5/2}$ peaks, averages 351.4 eV, which is again in good agreement with previous reports for bulk CdSe and CdSe nanocrystals.[66,67] Taken together, the XPS data clearly shows that the CdSe nanocrystals are not oxidized during either the templating process or thermal annealing step.

3.2.4 Ellipsometric-porosimetry Measurements

The micro- and mesoporosity of both template and untemplated CdSe nanocrystal films was analyzed by ellipsometric porosimetry using toluene as the adsorbate.[69] Figure 3.5a shows a typical adsorption-desorption isotherm for a PBO-*b*-PEO-templated CdSe mesoporous film,

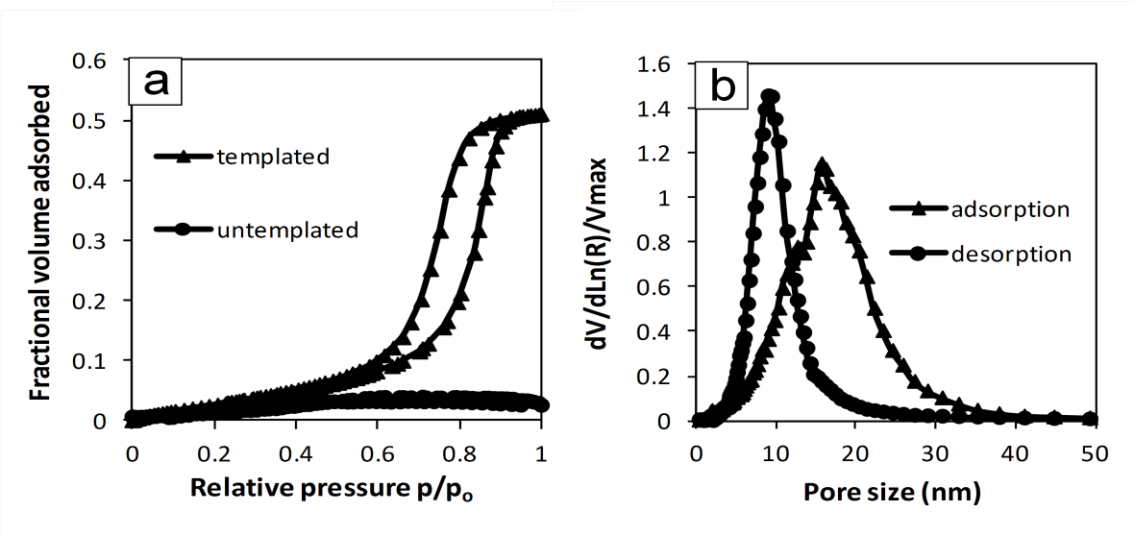

Figure 3.5. (a) Toluene adsorption-desorption isotherm for a templated CdSe nanocrystal-based mesoporous film (filled triangles) and a dense film of untemplated nanocrystals (filled circles). The mesoporous film exhibits a 50 % toluene-accessible porous volume while the dense film exhibits a 4 % toluene-accessible porous volume. (b) Corresponding pore size distribution data obtained for the templated film in (a).

demonstrating typical IV behavior.[70] The templated CdSe mesoporous film shows a 50 % overall toluene-accessible pore volume. The appearance of a hysteresis loop in the isotherm at higher relative pressures is representative of a mesoporous material that exhibits an interconnected porosity, where the absorption trace provides information about the size of any cages in the material, and the desorption trace provides information about neck sizes. The mesopore size distribution shown in Figure 3.5b was determined by fitting a Kelvin model to the data to give a cage diameter distribution centered at 18 nm and a neck diameter distribution centered at 9 nm. The mesopore size distribution determined by ellipsometric porosimetry, arising from the PBO-*b*-PEO template, is thus in good agreement with the pore diameter determined by SEM (Figure 3.2 a-d) and the average repeat distance determined by 2D-SAXS (Figure 3.1d) measurements. For comparison, data was also collected on a dense film of untemplated ligand-stripped nanocrystals. The dense film exhibited a 4 % overall toluene-accessible pore volume with a mesopore size distribution centered around 3 nm. Both films exhibit very similar behavior at lower pressures, indicating similar microporosity. At higher pressures, the templated films deviate significantly from the untemplated films, confirming the idea that the mesoporosity arises from the polymer template. As expected, the dense films have a much smaller pore volume, compared to the templated films, because the pores are created only by the random aggregation of the nanocrystal building blocks.

A fit of the Dubinin-Radushkevich model to the isotherm at lower relative pressures gives the micropore size distribution. Here we find a cage diameter of 2.0 nm and a neck diameter of 1.8 nm. The micropores arise from the spaces in between the CdSe nanocrystals that make up the pore walls. The same fit was applied to a dense film of untemplated nanocrystals, and the micropores were found to exhibit a cage size of 2.0 nm and a neck diameter of 1.2 nm. It

is likely that the 3 nm mesopores obtained from the Kelvin fit are part of the same continuous distribution of small pores, which lie at the size limits of both models. Based on this result, it is reasonable to speculate that the Dubinin-Radushkevich model may slightly underestimate the micropore size distribution in the template films as well. Overall, we find that both films have similar micropore sizes, suggesting that the nanocrystals retain their nanodimensional character when cast into films, regardless of the presence of polymer derived mesopores. The presence of both meso- and micropores in the templated CdSe films results in the useful combination of high surface are and good accessibility.

3.2.5 Electronic Properties of CdSe Films

Finally, to investigate the electrical properties of the templated CdSe nanocrystal-based mesoporous films, dc current-voltage measurements of CdSe nanocrystal-based films deposited onto ITO-coated glass substrate were performed using hanging mercury drop electrodes. Figure 3.3b depicts the current density-voltage characteristics obtained for a 100 nm thick mesoporous CdSe film. Figure 3.3b shows typical diodic behavior, thus allowing us to use a space-charge limited current (SCLC) model to estimate the carrier mobility from this data.[71] A fit to a logarithmic current density-voltage plot to the trap-free (or equivalently trap-filled) space charge limited region where the slope = 2 gives a SCLC mobility of 10^{-4} cm^2 V^{-1} s^{-1}, which is within the standard range of values reported in the literature for CdSe nanocrystal-based solid films.[65] These results demonstrate that in addition to the open porosity observed by porosimetry, these templated CdSe nanocrystal-based mesoporous films are also electrically interconnected. Such connectivity is key to both photovoltaic performance and to electrochemically assisted photocatalysis.

3.3 Conclusions

In this work, we report a solution-phase route for the assembly of ligand-stripped CdSe nanocrystals into mesoporous hierarchical architectures. The ligand-exchange process using Et_3OBF_4 readily produces "bare" CdSe nanocrystals that can be templated with a PBO-*b*-PEO block copolymer. Because the templating process is completely decoupled from the chemistry used to synthesize these nanocrystals, the method should be directly transferable to any other semiconductor or metal nanocrystals that can be ligand-stripped using Meerwein's salt, regardless of whether they are air-stable. We demonstrate that the crystal structure and composition of the templated CdSe films are retained during the thermal annealing process, and while some grain growth does occur, quantum confined excitonic features are still observed in the final porous material. The mesoporous CdSe films exhibit reasonable charge carrier mobility, confirming that the nanocrystals are electronically interconnected in the film. By varying the type and size of nanocrystal, block ratio, and total molecular weight of the block copolymer polymer used as the template, it should be possible to tune many of the details of the final architecture. This should make it possible to produce porous materials with varying composition, mesoporosity, and microporosity, which are important for applications where domain size, diffusion length and electronic conductivity effect device performance.

The method is also compositionally flexible – because the nanocrystals are synthesized in a step that is completely separate from the co-assembly, the nanocrystals are more physical objects than chemical species. This means that it should be possible to combine different types of nanocrystals into a single porous network, joining, for example, metals and semiconductors or two semiconductors with different band offsets.[72,73] More importantly, because the CdSe is porous, it should also be possible to fill the pore volume with other materials.[74,75] Extending

nanocrystal templating methods to systems that are not stable in air thus opens up the potential to produce an incredible diversity of designed composites that could exhibit novel or interesting properties.

3.4 Methods

3.4.1 Materials

The following chemicals were purchased and used as received: (Poly(butylene oxide)-*b*-poly(ethylene oxide), with a mass ratio of PBO(5000)-*b*-PEO(6500), a block ratio of PBO_{90}-*b*-PEO_{114}, and a PDI = 1.09 was purchased from Advanced Polymer Materials Inc.

3.4.2 Synthesis of CdSe nanocrystalsand mesoporous Films

CdSe nanocrystals were synthesized using the Workstation for Automated Nanomaterials Discovery and Analysis (WANDA), an automated nanocrystal synthesis robot housed in the Molecular Foundry, Lawrence Berkeley National Laboratory.[62] To carry out the ligand-exchange process, as-synthesized nanocrystals were treated with Et_3OBF_4 according to recently reported procedures.[59,61] All ligand-stripping reactions were carried out under inert conditions.

The synthesis of mesoporous CdSe nanocrystal-based films was carried out under inert conditions, including both film deposition and thermal annealing steps. In a typical procedure, 10 mg of the PBO_{90}-*b*-PEO_{114} diblock copolymer was dissolved in 0.1 mL of DMF with gentle heating. To this solution, 1 mL of CdSe nanocrystals dispersed in DMF (20 mg/mL) was added. From this mixture, thin films were prepared by spin-coating onto desired substrates (silicon, ITO-coated glass, or glass) at 1000 to 2000 rpm for 60 s. Thick films were be produced by drop casting onto desired substrates. The films were dried using a 3 h ramp up to 175 °C, followed by

a 3 h soak. Thermal decomposition of the template was done after the drying step using a 6 h ramp from 175 °C to 400 °C, followed by a 3 h soak.

3.4.4 Instrumentation

TEM images were obtained using a JEOL-2100 electron microscope operating at 200 kV. TGA measurements were performed under flowing argon gas using a Perkin Elmer Instruments Pyris Diamond TG/DTA Thermogravimetric/Differential Thermal Analyzer Module. SEM images were obtained using a JEOL model 6700F electron microscope with beam energy 5 kV. 2D-WAXS and 2D-SAXS data were collected at the Stanford Synchrotron Radiation Laboratory using beamlines 11-3 and 1-4. Absorbance spectra were performed on an Agilent HP 8452A UV-Vis Spectrophotometer. XPS analysis was performed using a Kratos Axis Ultra DLD with a monochromatic (K_α radiation) source. The charge neutralizer filament was used to control charging of the sample. A 20 eV pass energy was used with a 0.05 eV pass energy. Scans were calibrated using the C 1s peak shifted to 294.8 eV. DC conductivity of the CdSe films on ITO substrates were measured in an argon filled glovebox using a Solartron 1287 potentiostat and 1252A frequency analyzer. Voltage was applied through the CdSe film using two 16 mm^2 hanging mercury drops separated by 1 cm. Ellipsometric porosimetry was performed on a PS-1000 instrument from Semilab using toluene and as the solvent. A UV–visible CCD detector adapted to a grating spectrograph analyzes the signal reflected by the sample. The light source is a 75 W Hamamatsu Xenon lamp and measurements were performed on the spectral range from 1.24–4.5 eV. Data analysis was performed using the associated WinElli II software with the assumption of slit-like pores. If the actual pores are closer to cylindrical, the real pores sizes will be slightly larger than the values reported here. Data is fit with a contact angle of zero for the solvent.

3.5 References

[1] Zhang, Y.; Xie, Z.; Wang, J. Supramolecular-Templated Thick Mesoporous Titania Films for Dye-Sensitized Solar Cells: Effect of Morphology on Performance. *Appl. Mater. Inter.* **2009**, *1*, 2789-2795.

[2] Kim, J.-Y.; Kang, S. H.; Kim, H. S.; Sung, Y.-E. Preparation of Highly Ordered mesoporous Al_2O_3/TiO_2 and Its Application in Dye-Sensitized Solar Cells. *Langmuir*, **2010**, *26*, 2864-2870.

[3] Zhang, Y.; Yuwono, A. H.; Wang, J.; Li, J. Enhanced photocatalysis by doping cerium into mesoporous titania thin films. *J. Phys. Chem. C* **2009**, *113*, 21406-21412.

[4] Sreethawong, T.; Suzuki, Y.; Yoshikawa, S. Photocatalytic evolution of hydrogen over mesoporous TiO_2 supported NiO photocatalyst prepared by single-step sol-gel process with surfactant template. *Int. J. Hydrogen Energy* **2005**, *30*, 1053-1062.

[5] Brezesinski, B.; Wang, J.; Polleux, J.; Dunn, B.; Tolbert, S. H. Templated Nanocrystal-Based Porous TiO_2 Films for Next-Generation Electrochemical Capacitors *J. Am. Chem. Soc.* **2009,** *131*, 1802-1809.

[6] Wang, P.; Zakeeruddin, S. M.; Moser, J. E.; Nazeeruddin, M. K.; Sekiguchi, T.; Gratzel, M. A stable quasi-solid-state dye-sensitized solar cell with and amphiphilic ruthenium sensitizer and polymer gel electrolye. *Nat. Mater.* **2003**, *2*, 402- 407.

[7] Wang, P.; Zakeeruddin, S. M.; Comte, P.; Charvet, R.; Humphry-Baker, R.; Gratzel, M. Enhance the performance of dye-sensitized solar cells by Co-grafting amphiphilic sensitizer and hexadecylmalonic acid on TiO_2 nanocrystals. *J. Phys. Chem. B* **2003**, *107*, 14336-14341.

[8] Talapin, D. V.; Murray, C. B.; PbSe nanocrystal Solids for n- and p-Channel Thin Film Field-effect transistors. *Science* **2005**, *310*, 86-89.

[9] Gur, I.; Fromer, N. A.; Geier, M. L.; Alivisatos, A. P.; Air-stable All-inorganic nanocrystal solar cells processed from solution. *Science* **2005**, *310*, 462-465.

[10] Dayal, S.; Kopidakis, N.; Olson, D. C.; Ginley, D. S.; Rumbles, G.; Photovoltaic devices with a low band gap polymer and CdSe nanostructures exceeding 3 % efficiency. *Nano Lett.* **2010,** *10*, 239-242.

[11] Choi, J. J.; Wenger, W. N.; Hoffman, R. S.; Lim, Y.-F.; Luria, J.; Jasieniak, J.; Marohn, J. A.; Hanrath, T.; Solution-processed nanocrystal quantum dot tandem solar cells. *Adv. Mater.* **2011**, *23*, 3144-3148.

[12] Manna, L.; Milliron, D. J.; Meisel, A.; Scher, E. C.; Alivisatos, A. P.; Controlled growth of tetrapod-branced inorganic nanocrystals. *Nat. Mater.* **2003**, *2*, 382-385.

[13] Peng, X.; Manna, L.; Yang, W.; Wickham, J.; Scher, E.; Kadavanich, A.; Alivisatos, A. P.; Shape control of CdSe nanocrystals. *Nature,* **2000**, *404*, 59-61.

[14] Murray, C. B.; Norris, D. J.; Bawendi, M. G. Synthesis and characterization of nearly monodisperse CdE (E = S, Se, Te) semiconductor nanocrystallites. *J. Am. Chem. Soc.* **1993**, *115*, 8706-8715.

[15] Hines, M. A.; Guyot-Sionnest, P.; Synthesis and characterization of strongly luminescing ZnS-capped CdSe nanocrystals. *J. Phys. Chem.* **1996**, *100*, 468-471.

[16] Peng, X.; Schlamp, M. C.; Kadavanich, A. V.; Alivisatos, A. P.; Epitaxial growth of highly luminescent CdSe/CdS Core/Shell nanocrystals with photostabiliy and electronic accessibility. *J. Am. Chem. Soc.* **1997**, *119*, 7019-7029.

[17] Guzelian, A. A.; Banin, U.; Kadavanich, A. V.; Peng, X.; Alivisatos, A. P. Colloidal chemical synthesis and characterization of InAs nanocrystal quantum dots. *Appl. Phys. Lett.* **1996**, *69*, 1432-1434.

[18] Kruszynska, M.; Borchert, H.; Parisi, J.; Kolny-Olesiak, J. Synthesis and shape control of $CuInS_2$ nanoparticles. *J. Am. Chem. Soc.* **2010**, *132*, 15976-15986.

[19] Shevchenko, E. V.; Talapin, D. V.; Kotov, N. A.; O'Brien, S. O.; Murray, C. B. Structural diversity in binary nanoparticle superlattices. *Nature* **2006**, *439*, 55-59.

[20] Talapin, D. V.; Shevchenko, E. V.; Bodnarchuk, M. I.; Ye, X.; Chen, J.; Murray, C. B. Quasicrystalline order in self-assembled binary nanoparticle superlattices. *Nature* **2009**, *461*, 964-967.

[21] Zhao, H.; Wang, D.; Chaker, M.; Ma, D.; Effect of different types of surface ligands on the structure and optical property of water-soluble PbS quantum dots encapsulated by amphiphilic polymers. *J. Phys. Chem. C* **2011**, *115*, 1620-1626.

[22] Aldana, J.; Wang, Y. A.; Peng, X.; Photochemical Instability of CdSe Nanocrystals Coated by Hydrophilic Thiols. *J. Am. Chem. Soc.* **2001**, *123*, 8844-8850.

[23] Law, M.; Luther, J. M.; Song, Q.; Hughes, B. K.; Perkins, C. L.; Nozik, A. J.; Structural, Optical, and electrical properties of PbSe nanocrystals solids treated thermally or with simple amines. *J. Am. Chem. Soc.* **2008**, *130*, 5974-5985.

[24] Luther, J. M.; Law, M.; Song, Q.; Perkins, C. L.; Beard, M. C.; Nozik, A. J.; Structural, Optical, and Electrical Properties of Self-Assembled Films of PbSe Nanocrystals Treated with 1,2-Ethanedithiol. *ACS Nano* **2008**, *2*, 271-280.

[25] Zarghami, M. H.; Liu, Y.; Gibbs, M.; Gebremichael, E.; Webster, C.; Law, M.; p-Type PbSe and PbS Quantum Dot Solids Prepared with Short-Chain Acids and Diacids. *ACS Nano* **2010**, *4*, 2475-2485.

[26] Kovalenko, M. V.; Scheele, M.; Talapin, D. V. Colloidal nanocrystals with molecular metal chalchogenide surface ligands. *Science* **2009**, *324*, 1417-1420.

[27] Wang, R.; Tangirala, R.; Raoux, S.; Jordan-Sweet, J. L.; Milliron, D. J. Ionic and electronic transport in Ag_2S nanocrystal-GeS_2 Matrix Composites with size-controlled Ag_2S nanocrystals. *Adv. Mater*. **2012**, *24*, 99-103.

[28] Jiang, C.; Lee, J.-S.; Talapin, D. V. Soluble precursors for $CuInSe_2$, $CuIn_{1-x}Ga_xSe_2$, and $Cu_2ZnSn(S,Se)_4$ based on colloidal nanocrystals and molecular metal chalcogenide surface ligands. *J. Am. Chem. Soc.* **2012**, *134*, 5010-5013.

[29] Rangirala, R.; Baker, J. L.; Alivisatos, A. P.; Milliron, D. J. Modular Inorganic Nanocomposites by Conversion of Nanocrystal superlattices. *Angew. Chem. Int. Ed.* **2010**, *49*, 2878-2882.

[30] Mohanan, J. L.; Arachchige, I. U.; Brock, S. L. Porous Semiconductor Chalcogenide Aerogels. *Science* **2005**, *307*, 397-400.

[31] Gaponik, N.; Wolf, A.; Marx, R.; Lesnyak, V.; Schilling, K.; Eychmuller, A. Three-dimensional self-assembly of thiol-capped CdTe nanocrystals: Gels and Aerogels as building blocks for nanotechnology. *Adv. Mater.* **2008**, *20*, 4257-4262.

[32] Yao, Q.; Brock, S. L. Porous CdTe nanocrystals assemblies: Ligation effects on the gelation process and the properties of resultant aerogels. *Inorg. Chem.* **2011**, *50*, 9985-9992.

[33] Yao, Q. Arachchige, I. U.; Brock, S. L. Brock. Expanding the repertoire of chalcogenide nanocrystal networks: Ag2Se gels and aerogels by cation exchange reactions. *J. Am. Chem. Soc.* **2009**, *131*, 2800-2801.

[34]Yanagisawa, T.; Shimizu, T.; Kuroda, K.; Kato, C. The preparation of alkyltrimethylammonium-kanemite complexes and their conversion to microporous materials *Bull. Chem. Soc. Jpn.* **1990**, *63*, 988-992.

[35] Inagaki, S.; Fukushima, Y.; Kuroda, K. *J.* Synthesis of highly ordered mesoporous materials from a layered polysilicate. *Chem. Soc. Chem. Commun.* **1993**, 680-682.

[36] Kresge, C. T.; Leonowicz, M. E.; Roth, W. J.; Vartuli, J. C.; Beck, J. S. Ordered mesoporous molecular sieves synthesized by a liquid-crystal template mechanism *Nature* **1992**, *359*, 710-712.

[37] Beck, J. S.; Vartuli, J. C.; Roth, W. L.; Leonowicz, M. E.; Kresge, C. T.; Schmidt, K. D.; Chu, C. T.-W.; Olson, D. H.; Sheppard, E. W.; McCullen, S. B.; Higgins, J. B.; Schlenker, J. L. A new family of mesoporous molecular sieves prepared with liquid crystal templates. *J. Am. Chem. Soc.* **1992,** *114*, 10834-10843.

[38] Zhao, D. Y.; Feng, J. L.; Huo, Q. S.; Melosh, N.; Fredrickson, G. H.; Chmelka, B. F.; Stucky, G. D. Triblock Copolymer Syntheses of Mesoporous Silica with Periodic 50 to 300 Angstrom Pores. *Science* **1998**, *279*, 548-552.

[39] Monnier, A.; Schuth, F.; Huo, Q.; Kumar, D.; Margolese, D.; Maxwell, R. S.; Stucky, G. D.; Krishnamurty, M.; Petroff, P.; Firouzi, A.; Janicke, M.; Chmelka, B. F.; Cooperative Formation of Inorganic-Organic Interfaces in the Synthesis of Silicate Mesostructures. *Science* **1993**, *261*, 1299-1303.

[40] Yang, P.; Deng, T.; Zhao, D.; Feng, P.; Pine, D.; Chmelka, B.; Whitesides, G.; Stucky, G. D. Hierarchically Ordered Oxides. *Science* **1998**, *282*, 2244-2246.

[41] Templin, M.; Franck, A.; Chesne, A. D.; Leist, H.; Zhang, Y.; Ulrich, R.; Schadler, V.; Wiesner, U; Organically Modified Aluminosilicate Mesostructures from Block Copolymer Phases. *Science* **1997**, *278*, 1795-1798.

[42] Tian, B. Z.; Liu, X. Y.; Tu, B.; Yu, C. Z.; Fan, J.; Wang, L. M.; Xie, S. H.; Stucky, G. D.; Zhao, D. Y. Self-adjusted synthesis of ordered stable mesoporous minerals by acid–base pairs *Nat. Mater.* **2003**, *2*, 159-163.

[43] Antonelli, D. M.; Ying, J. Y. Synthesis of Hexagonally Packed Mesoporous TiO_2 by a Modified Sol–Gel Method *Angew. Chem., Int. Ed. Engl.* **1995**, *34*, 2014-2017.

[44] Mamak, M.; Coombs, N.; Ozin, G. Mesoporous Yttria–Zirconia and Metal–Yttria–Zirconia Solid Solutions for Fuel Cells *Adv. Mater.* **2000**, *12*, 198-202.

[45] Warren, S. C.; Perkins, M. R.; Adams, A. M.; Kamperman, M.; Burns, A. A.; Arora, H.; Herz, E.; Suteewong, T.; Sai, H.; Li, Z.; Werner, J.; Song, J.; Werner-Zwanziger, U.; Zwanziger, J. W.; Gratzel, M.; DiSalvo, F. J.; Wiesner, U.; A silica sol–gel design strategy for nanostructured metallic materials *Nat. Mater.* **2012**, *11*, 460-467.

[46] Brezesinski, B.; Wang, J.; Tolbert, S. H.; Dunn, B.; Ordered Mesoporous Alpha-MoO_3 with Iso-Oriented Nanocrystalline Walls for Thin-Film Pseudocapacitors. *Nat. Mater.* **2010,** *9*, 146-151.

[47] Templin, M.; Franck, A.; Chesne, A. D.; Leist, H.; Zhang, Y.; Ulrich, R.; Schadler, V.; Wiesner, U; Organically Modified Aluminosilicate Mesostructures from Block Copolymer Phases. *Science* **1997**, *278*, 1795-1798.

[48] Kuemmel, M.; Smatt, J.-H.; Boissiere, C.; Nicole, L.; Sanchez, C.; Linden, M.; Grosso, D.; Hierarchical Inorganic Nanopatterning (INP) Through Direct Easy Block-Copolymer Templating *J. Mater. Chem.*, **2009**, *19*, 3638-3642.

[49] Brezesinski, K.; Wang, J.; Haetge, J.; Reitz, C.; Steinmueller, S. O.; Tolbert, S. H.; Smarsly, B. M.; Dunn, B.; Brezesinski, T.; Pseudocapacitive Contributions to Charge Storage in Highly

Ordered Mesoporous Group V Transition Metal Oxides with Iso-Oriented Layered Nanocrystalline Domains. *J. Am. Chem. Soc*. **2010**, *132*, 6982-6990.

[50] Quickel, T. E.; Le, V. H.; Brezensinski, T.; Tolbert, S. H. On the Correlation Between Nanoscale Structure and Magnetic Properties in Ordered Mesoporous Cobalt Ferrite ($CoFe_2O_4$) Thin Films. *Nano Lett.* **2010**, *10*, 2982-2988.

[51] Rauda, I. E.; Buonsanti, R.; Saldarriaga-Lopez, L. C.; Benjauthrit, K.; Schelhas, L. T.; Stefik, M.; Augustyn, V.; Ko, J.; Dunn, B.; Wiesner, U.; Milliron, D. J.; Tolbert, S. H.; General method for the synthesis of hierarchical nanocrystal-based mesoporous materials. *ACS Nano*, **2012**, *6*, 6386-6399.

[52] Buonsanti, R.; Pick, T. E.; Krins, N.; Richardson, T. J.; Helms, B. A.; Milliron, D. J.; Assembly of ligand-stripped nanocrystals into precisely controlled mesoporous architectures. *Nano Lett.* **2012**, *12*, 3872-3877.

[53] Warren, S. C.; Messina, L. C.; Slaughter, L. S.; Kamperman, M.; Zhou, Q.; Gruner, S. M.; DiSalvo, F. J.; Wiesner, U.; Ordered Mesoporous Materials from Metal Nanoparticle-Block Copolymer Self-Assembly. *Science* **2008**, *320*, 1748-1752.

[54] Ba, J. H.; Polleux, J.; Antonietti, M.; Niederberger, M. Non-aqueous Synthesis of Tin Oxide Nanocrystals and Their Assembly into Ordered Porous Mesostructures. *Adv. Mater.* **2005**, *17*, 2509-2512.

[55] Corma, A.; Atienzar, P.; Garcia, H.; Chane-Ching, J. Y. Hierarchically Mesostructured Doped CeO_2 with Potential for Solar-Cell Use. *Nat. Mater.* **2004**, *3*, 394-397.

[56] Deshpande, A. S.; Pinna, N.; Smarsly, B.; Antonietti, M.; Niederberger, M. Controlled Assembly of Preformed Ceria Nanocrystals into Highly Ordered 3D Nanostructures. *Small* **2005**, *1*, 313-316.

[57] Dong, A.; Ye, X.; Chen, J.; Kang, Y.; Gordon, T.; Kikkawa, J. M.; Murray, C. B. A Generalized Ligand-Exchange Strategy Enabling Sequential Surface Functionalization of Colloidal Nanocrystals. *J. Am. Chem. Soc*. **2011,** *133*, 998-1006.

[58] Nag, A.; Kovalenko, M. V.; Lee, J-S.; Liu, W.; Spokoyny, B.; Talapin, D. V.; Metal-free Inorganic Ligands for Colloidal Nanocrystals: S^{2-}, HS^{-}, Se^{2-}, HSe^{-}, Te^{2-}, HTe^{-}, TeS_3^{2-}, OH^{-}, and NH^{2-} as Surface Ligands. *J. Am. Chem. Soc*. **2011,** *133*, 10612-10620.

[59] Rosen, E. L.; Buonsanti, R.; Llordes, A.; Sawvel, A. M.; Milliron, D. J.; Helms, B. A.; Exceptionally Mild Reactive Stripping of Native Ligands from Nanocrystal Surfaces by Using Meerwein's Salt. *Angew. Chem. Int. Ed*. **2012,** *51*, 684-689.

[60] Llordes, A.; Hammack, A. T.; Buonsanti, R.; Tangirala, R.; Aloni, S.; Helms, B. A.; Milliron, D. J. Polyoxometalates and Colloidal Nanocrystals as Building Blocks for Metal Oxide Nanocomposite Films. *J. Mater. Chem.* **2011,** *21*, 11631-11638.

[61] Duong, J. T., Bailey, M. J., Pick, T. E., McBride, P. M., Rosen, E. L., Buonsanti, R., Milliron, D. J., Helms, B. A.; Efficient Polymer Passivation of Ligand-Stripped Nanocrystal Surfaces. *J. Polym. Sci. A Polm. Chem.* **2012,** *50*, 3719-3727.

[62] Chan, E. M., Xu, C., Mao, A. W., Han, G., Owen, J. S., Cohen, B. E., Milliron, D. J. Reproducible, High-Througput Synthesis of Colloidal Nanocrystals for Optimization in Multidimensional Parameter Space. *Nano Lett.* **2010**, *10*, 1874-1885.

[63] Fedorov, V. A.; Ganshin, V. A.; Korkishko, Y. N. Determination of the Point of the Zincblende-to-Wurtzite Structural Phase Transition in Cadmium Selenide Crystals. *Phys. Stat. Sol. A.* **1991**, *126*, K5-K7.

[64] Jasieniak, J,; Smith, L.; van Embden, J.; Mulvaney, P.; Califano, M.; Re-examination of the size-dependent absorption properties of CdSe quantum dots. *J. Phys. Chem. C* **2009**, *113*, 19468-19474.

[65] Webber, D. H.; Brutchey, R. L.; Ligand exchange on colloidal CdSe nanocrystals using thermally labile tert-butylthiol for improved photocurrent in nanocrystal films. *J. Am. Chem. Soc.* **2012**, *134*, 1085-1092.

[66] Katari, J. E. B.; Colvin, V. L.; Alivisatos, A. P. X-ray photoelectron spectroscopy of CdSe nanocrystals with applications to studies of the nanocrystal surface. *J. Phys. Chem.* **1994**, *98*, 4109-4117.

[67] Vesely, C. J.; Langer, D. W.; Electronic Core Levels of the II*B*-VI*A* Compounds. *Phys. Rev. B* **1971**, *4*, 451-462.

[68] Tsuchiya, K.; Sakata, M.; Funyu, A.; Ikoma, H. Selenium passivation of GaAs with Se/NH_4OH solution. *Jpn. J. Appl. Phys*. **1995**, *34*, 5926-5932.

[69] Baklanov, M. R.; Mogilnikov, K. P.; Polovinkin, V. G.; Dultsev, F. N.; Determination of Pore Size Distribution in Thin Films by Ellipsometric Porosimetry. *J. of Vac. Sci. & Tech. B* **2000**, *18*, 1385-1391.

[70] Gregg, S. J.; Sing, K. S. W.; Adsorption, Surface Area, and Porosity. 2nd ed. (Academic, London, **1982**).

[71]Hikmet, R. A. M.; Talapin, D. V.; Weller, H. Study of conduction mechanism and electroluminescenece in CdSe/ZnS quantum dot composites. *J. Appl. Phys.* **2003**, *93*, 3509-3514.

[72] Nakayama, T.; Murayama, M. Chemical trend of band offsets at wurtzite/zinc-blende heterocrystalline semiconductor interfaces. *Phys. Rev. B* **1994**, *49*, 4710-4724.

[73] Wei, S.-H.; Zunger, A. Calculated natural band offsets of all II-VI and II-V semiconductors: chemical trends and the role of cation *d* orbitals. *Appl. Phys. Lett*. **1998**, *72*, 2011-2013.

[74] Coakley, K. M.; Liu, Y.; McGehee, M. D.; Frindell, K. L.; Stucky, G. D. Infiltrating semiconducting polymers into self-assembled mesoporous titania films for photovoltaic applications. *Adv. Funct. Mater*. **2003**, *13*, 301-306.

[75] Coakley, K. M.; McGehee, M. D. Photovoltaic cells made from conjugated polymers infiltrated into mesoporous titania. *Appl. Phys. Lett*. **2003**, *83*, 3380-3382.

CHAPTER 4

A General Method for the Synthesis of Hierarchical Nanocrystal-Based Mesoporous Materials

4.1 Introduction

One of the key goals of nanoscience research over the past 2 decades has been the development of methods to precisely control structure at the nanometer length scale. One route to this control that has met with significant success is amphiphilic templating of inorganic materials. In this method, soluble inorganic oligomers co-assemble with amphiphilic organic species to produce a structured inorganic/organic composite material. Thermal or chemical removal of the organic component leaves behind an inorganic material with porosity on the nanometer length scale, and an architecture that is determined by co-assembly of the organic and inorganic components.[1-9] Common structure directing agents include surfactants and block copolymers, and these have been used to prepare a broad range of mesoporous architectures from soluble inorganic building blocks, in most cases utilizing sol-gel chemistries.[10-28]

While this method provides beautiful control of nanometer scale architecture, there is much less control of the atomic scale structure in most templated nanoporous materials. Pore walls can be crystallized by thermal processing, but in many cases the walls do not fully crystallize during template removal, resulting in a partially crystalline or amorphous pore wall.[29-30] Moreover, the lack of control of grain growth during the crystallization process can result in the destruction of the pore-solid architecture and the interconnected porosity. Creating materials with this type of nanometer scale architecture is a worthwhile goal, however, as this architecture

imparts the unique combination of a high surface, an electrically interconnected structure, and good accessibility to the surface area from the porosity.

One approach to mitigate the problems associated with crystallization of the inorganic framework is to start not with sol-gel type molecular precursors, but with preformed nanocrystals. Using this method, crystalline nanoporous materials can be produced, and because thermal processing is needed only to remove the polymer template and network the nanocrystals, not to crystallize the inorganic phase, open, interconnected porosity is well retained. A few examples of this type of nanocrystal templating exist in the literature.[31-36] The problem is that while the literature is full of beautiful routes to soluble nanocrystals with well-defined chemical composition, size, shape, and distinctive optical, electronic, and chemical properties,[37-50] the vast majority of those nanocrystals are coated with organic surface ligands that provide solubility and prevent nanocrystal agglomeration. In order to substitute sol-gel type precursors with pre-formed nanocrystals in typical template-driven syntheses, the ligands must be removed from the nanocrystals while maintaining nanocrystal solubility and preventing aggregation. Most of the previous results for nanocrystal templating utilized nanocrystals with hydrolysable surface groups that could be removed by the addition of small quantities of water to produce metastable, hydroxyl-terminated nanocrystals.[51,52] Such methods are not general, however, because in many cases removal of the surface groups leads to agglomerated nanocrystals that cannot be templated, limiting the types of nanocrystal-based nanoporous materials that can be produced.

One reason that nanocrystal-templating is so important is that we have recently shown that nanocrystal-based nanoporous titania demonstrates high levels of pseudocapacitive charge storage accompanied by fast charging/discharging rates.[35] These materials were synthesized from nanocrystals that contained hydrolysable surface ligands, as discussed above.[51,52] In that

work, enhancement of electrochemical properties resulted from the unique combination of open porosity, which allowed facile electrolyte diffusion throughout the material, and the high density of electrochemically active surface redox sites, which results from the high surface area of the nanocrystal building blocks that made up the pores walls.[35] In order to be able to extend this approach to a broader array of nanocrystals, a more broadly applicable method for templating ligand-stripped nanocrystals is needed. Because of this interest in materials for electrochemical supercapacitors, the materials that we have chosen to explore in this work are either conductors or redox active transition metal oxides. The technique should be applicable, however, to any nanocrystal system that is stable under the calcination conditions required to remove the polymer template.

Recently, there have been few reports on methods to strip native ligands off the surface of nanocrystals to produce bare, soluble nanocrystals that can be dissolved in polar solvents.[53-55] The first example was work by Murray and co-workers, who reported a method that employed nitrosonium tetrafluoroborate ($NOBF_4$).[53] The authors speculate that NO^+ reacts with trace water to form nitrous and/or fluoroboric acid which protonate basic ligands such as carboxylic acids and amines so that they desorb from the surface of nanocrystals, accompanied by phase transfer of the nanocrystals from nonpolar to polar solvents.[53] In that work, the native organic ligands are removed and replaced by some combination of protons and dimethylformamide (DMF), to produce dispersible, cationic nanocrystals that are charge-balanced by BF_4^- anions. Milliron and coworkers used this method to prepare nanocomposite films containing Sn-doped In_2O_3 (ITO) nanocrystals in transition metal oxide matrices.[56] Recently, related but milder ligand stripping methods have also been reported, so that ligands can now be removed non-destructively from a broad range of nanocrystals.[55]

In this work, we build from our previous work on templating nanocrystals into porous architectures and describe a general route to prepare hierarchical nanocrystal-based mesoporous films of various systems. The $NOBF_4$ ligand-exchange strategy is utilized to prepare dispersible nanocrystals of various oxide systems including ITO,[56-58] manganese oxide (Mn_3O_4),[59] and manganese ferrite ($MnFe_2O_4$).[60] We demonstrate the generality of this approach by varying the composition and size of the nanocrystals. In addition, nanocrystals are templated with a range of di-block copolymers containing variable block compositions and molecular weights. Films are produced by various coating methods including dip-coating, spin-coating, and drop-casting. We further show that even greater material diversity is accessible through solid-state conversion reactions. For example, the $MnFe_2O_4$ system can be converted to a mixed manganese-iron oxide $(Mn,Fe)_2O_3$ with retention of the original porous architecture. Taken together, the results demonstrated in this work describe a powerful approach to templating diverse nanocrystal systems and, therefore, a simple recipe for preparing functional nanoscale architectures from preformed nanocrystal building blocks.

4.2 Results and Discussion

4.2.1 Preparation of Mesoporous Nanocrystal-based Films

The synthesis of mesoporous nanocrystal-based materials is described in detail in the experimental section. The key steps in the process, however, are discussed here. The overall synthetic process involves nanocrystal synthesis, ligand removal, and templating of the desired nanocrystal system. In all cases, nanocrystals were synthesized using previously reported high-temperature solution-phase syntheses that utilize organic ligands with either amine or carboxylic

acid functional groups to stabilize the nanocrystal surface.[56-60] As-synthesized nanocrystals dispersed in hexane were then stripped of their surface ligands and phase transferred into polar media by treatment with $NOBF_4$ in DMF, as described above.[53] In a typical film synthesis, ethanolic dispersions of the ligand-exchanged pre-formed nanocrystals, with ~10% DMF (v/v), were mixed with a block copolymer template, dissolved in pure ethanol, to prepare the coating solution. Thin-films were dip-coated onto clean polar substrates through an evaporation-induced self-assembly process.[61] In solution, the polymer forms micelles and, upon evaporation of the solvent, the micelles co-assemble with the pre-formed nanoparticles and both components self-organize into a mesostructured organic/inorganic composite. Next, the organic polymer template is thermally decomposed in air to leave behind a mesoporous inorganic architecture that exhibits three-dimensionally interconnected porosity.

Dispersible, ligand-free nanocrystal building blocks are essential to this process. Figure 4.1 shows the transmission electron microscopy (TEM) images of three different compositions of nanocrystals, both before and after ligand-stripping with $NOBF_4$. The images show ITO (Figure 4.1a-b), $MnFe_2O_4$ (Figure 4.1c-d), and Mn_3O_4 (Figure 4.1e-f) nanocrystals with ligand-stripped samples in panels b, d, and f. As can be seen in Figure 4.1b, $NOBF_4$-treated ITO nanocrystals are not agglomerated or fused together, suggesting they form stable dispersions.[53] A closer look at the particles after $NOBF_4$ treatment reveals a shorter inter-particle distance which is consistent with removal of the native ligands.[53] In addition, the average particle size (7.3 ± 0.7 nm) does not change suggesting no etching of the surface of the nanocrystals during the $NOBF_4$ treatment. Similar results were observed for both $MnFe_2O_4$ (Figure 4.1c-d) and Mn_3O_4 (Figure 4.1e-f) nanocrystals. There is no apparent agglomeration or change in particle size for either $MnFe_2O_4$ (4.6 ± 0.5 nm) or Mn_3O_4 (4.8 ± 0.5 nm) nanocrystals after $NOBF_4$ treatment. Taken together, the

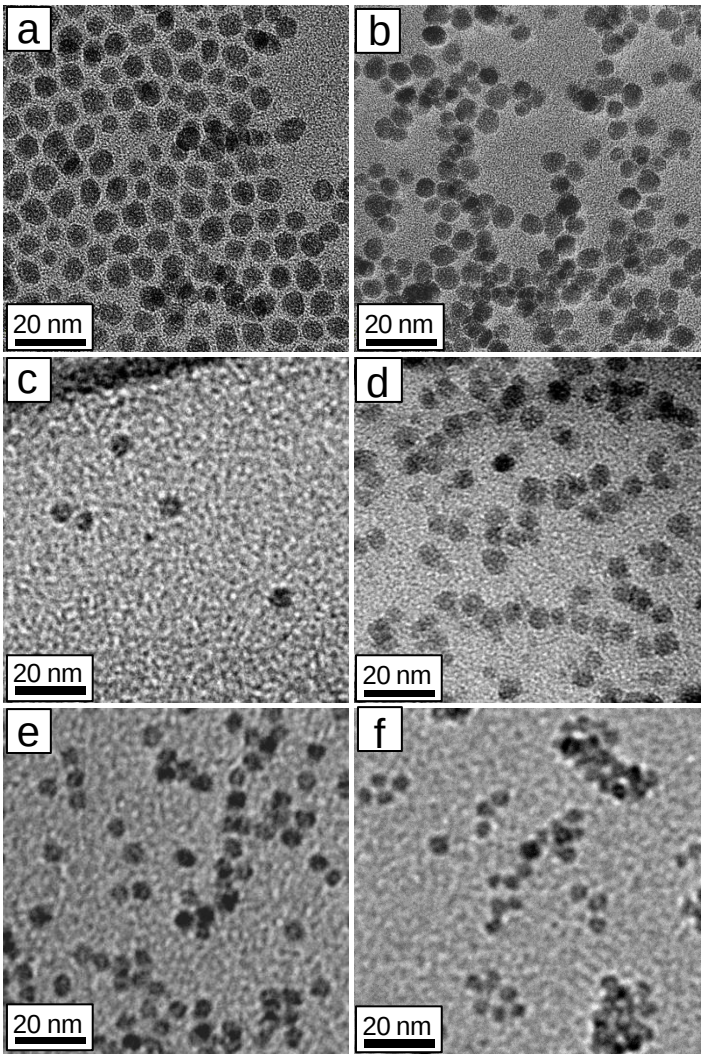

Figure 4.1. TEM images of ITO nanocrystals as-synthesized (a) and after the ligand-exchange process (b); $MnFe_2O_4$ nanocrystals as-synthesized (c) and after the ligand-exchange process (d); and Mn_3O_4 nanocrystals as-synthesized (e) and after the ligand-exchange process (f). In all cases, the particles do not agglomerate and maintain a uniform size and shape after the ligand removal process.

TEM data for all three systems reveal the nanocrystals have a uniform size and shape that is not altered by the ligand removal process. These data suggest that $NOBF_4$ stripping is a viable method that can be utilized to prepare dispersions of many nanocrystals compositions for use in polymer templating.

To this end, figure 4.2 shows top view scanning electron microscope (SEM) images of mesoporous films produced from these same three nanocrystal systems including: ITO (Figure 4.2a-b), Mn_3O_4 (Figure 4.2c-d) and $MnFe_2O_4$ (Figure 4.2e-f). For all three systems the block copolymer template utilized was poly(ethylene-*alt*-propylene)-*block*-poly(ethylene oxide), (PEP-*b*-PEO) (polydispersity index (PDI) = 1.05), which was thermally decomposed between 350 and 450 °C in air to produce the porous materials. This class of amphiphilic block copolymers has been shown to produce well-ordered, periodic mesoporous inorganic materials.[16,35,62-72] In the synthesis, we begin with ligand-exchanged nanocrystals that are stabilized in solution by a combination of dative bonds from the DMF solvent and electrostatic repulsion from the charged nanocrystal surface. Upon addition of the polymer, the PEO block likely coordinates to the nanocrystal surface so that upon solvent evaporation the nanocrystals preferentially segregate to the PEO region of the composite film. Thermal treatment is then used to thermally degrade the polymer and fuse the nanocrystals together. The thermal stability of the hydrophobic polymer block ensures that the nanocrystals are well fused before full thermal decomposition of the template, resulting in a rigid inorganic porous structure.

The films in Figure 4.2a-b were prepared from ITO nanocrystals with a diameter of 7.3 ± 0.7 nm.[56] Figure 4.2a shows a low-magnification image of an ITO film where the mesopores are locally disordered, but they are macroscopically homogeneous with an average diameter of 15 ± 3 nm. The pore walls range from 1 – 3 nanocrystals across, with approximately 2 nanocrystals

representing the majority of pore walls in the film. Given an average nanocrystal diameter of 7.3 ± 0.7 nm, the sum of the pore diameter and the average wall thickness is in reasonable agreement with two-dimensional small-angle X-ray scattering (see below, 2D-SAXS, Figure 6a) data where the average repeat distance was found to be 32 nm. These films are crack-free and the pores are open at the surface. Figure 4.1b shows a high-magnification image where the presence of individual nanocrystals can also be seen; the voids between these nanocrystals give rise to micropores that significantly increase surface area.

Figure 4.2c shows a top view low-magnification image of PEP-*b*-PEO templated Mn_3O_4 nanocrystals with an average diameter of 4.8 ± 0.5 nm.[59] A high-magnification image of Mn_3O_4 films is shown in Figure 4.2d. Similarly, low-magnification (Figure 4.2e) and high magnification (Figure 4.2f) images of $MnFe_2O_4$ nanocrystal-based films with an average particle diameter of 4.6 ± 0.5 nm [60] are also shown. For these two films, just as for ITO, the mesopores are locally disordered, with an average pore diameter of 17 ± 4 nm for Mn_3O_4 films and 16 ± 2 nm for $MnFe_2O_4$ films. In the high-magnification images for both Mn_3O_4 and $(Mn,Fe)_2O_3$, the presence of individual nanocrystals that give rise to micropores are again visible. In all three types of nanocrystal-based films, ITO, Mn_3O_4, and $MnFe_2O_4$, the pore walls are comprised of nanocrystals that fuse only at point contact and retain their generally spherical shape. Because the nanocrystals in the pore walls do not fully fuse to form a dense wall, microposity is generated. This figure thus demonstrates that our templating approach can be applied to nanocrystals with a broad range of compositions, producing films with nearly identical nanometer scale architecture.

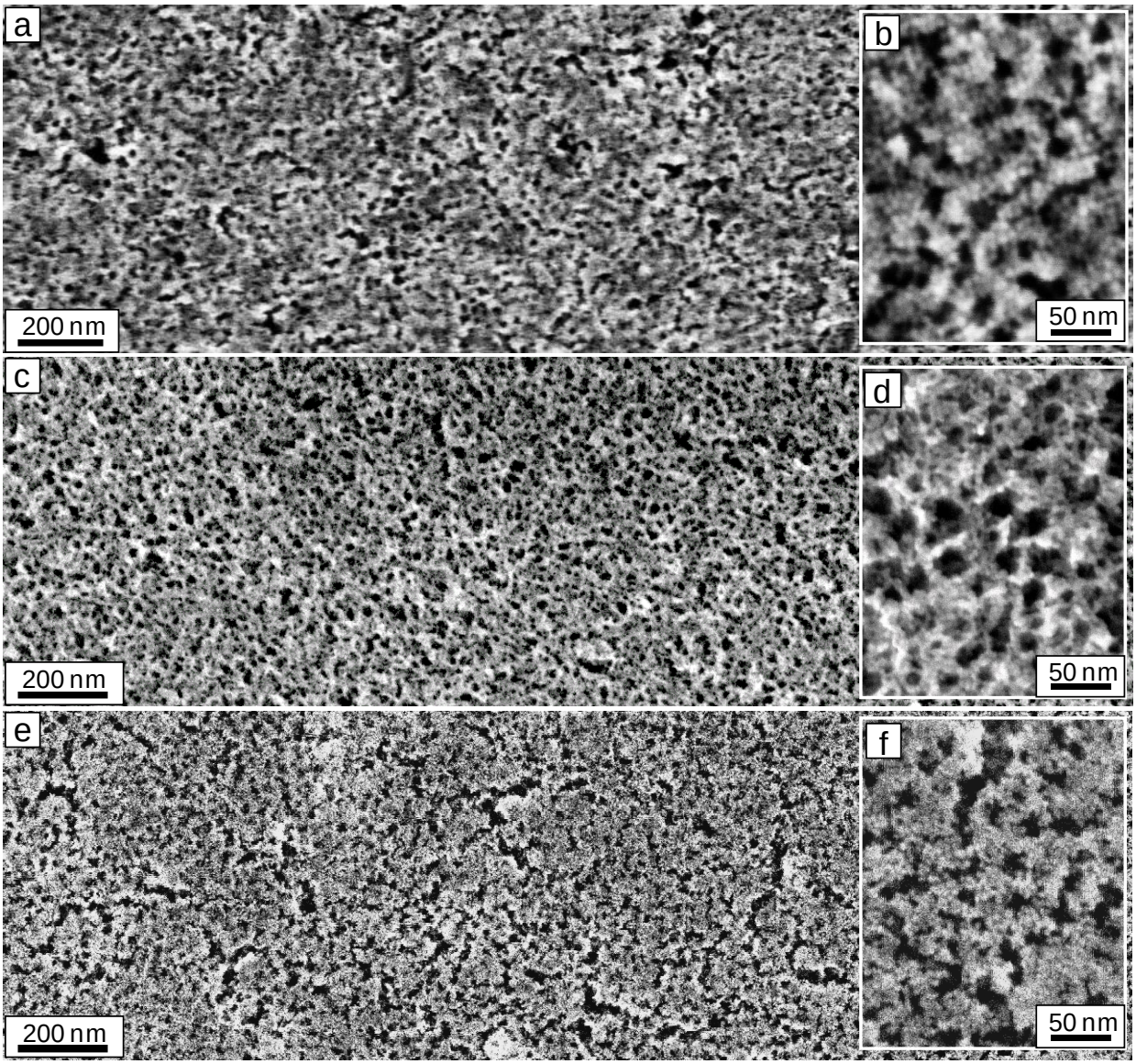

Figure 4.2. SEM images of various templated nanocrystal-based porous films. (a) Low-magnification and (b) high-magnification top-view SEM images of PEP-*b*-PEO templated ITO nanocrystals. (c) Low-magnification and (d) high-magnification top-view SEM images of PEP-*b*-PEO templated Mn_3O_4 nanocrystals. (e) Low-magnification and (f) high-magnification top-view SEM images of PEP-*b*-PEO templated $MnFe_2O_4$ nanocrystals.

4.2.2 Synthetic and Structural Tunability

To demonstrate the extent of synthetic tunability in our approach we explored several different parameters including choice of block copolymer, coating technique and size of the nanocrystal. In addition to the PEP-*b*-PEO polymer used to prepare the films in Figure 4.2, we can template films with poly(butadiene(1,2 addition))-*block*-poly(ethylene oxide) (PB-*b*-PEO),[72] and poly(butylene oxide)-*block*-poly(ethylene oxide) (PBO-*b*-PEO). Chemically speaking, all three polymers have a PEO hydrophilic block that may vary in length and a hydrophobic block which may also vary in length. To investigate the architectural effects from each polymer template the differences in the weight fraction and molecular weight for each block must also be considered. Here, the weight fraction for the PEO block, f_w PEO, in PEP-*b*-PEO is defined as f_w PEO = M_w PEO / (M_w PEO + M_w PEP), where M_w PEO and M_w PEP are the molecular weights for the individual blocks. Using this definition, the weight fractions for PEP-*b*-PEO are f_w PEP = 0.49 (M_w = 3900 g/mol) and f_w PEO = 0.51 (M_w = 4000 g/mol), for PB-*b*-PEO they are f_w PB = 0.52 (M_w = 5500 g/mol) and f_w PEO = 0.48 (M_w = 5000 g/mol), and for PBO-*b*-PEO they are f_w PBO = 0.57 (M_w = 6500 g/mol) and f_w PEO = 0.43 (M_w = 5000 g/mol). All polymers have similar hydrophilic:hydrophobic block ratios, but the total molecular weights and the chemical nature of the hydrophobic block varies significantly. A more detailed description of the block length, molecular weight and weight fraction for each block in all three block copolymers can be found in the experimental section.

Figure 3a-b shows top-view SEM images of PB-*b*-PEO templated ITO nanocrystals with an average diameter of 7.3 ± 0.7 nm prepared by spin-coating (Figure 4.3a) and dip-coating (Figure 4.3b). Similar to the PEP-*b*-PEO templated ITO nanocrystals in Figure 4.2a-b, these films demonstrate a locally disordered mesostructure with macroscopically homogeneous

porosity. PB-*b*-PEO templated films have an average pore diameter of 28 ± 3 nm and the pore walls are approximately one to three nanocrystals thick. In agreement with these values, the average distance between pores was found to be fairly large (around 36 nm) from 2D-SAXS data, Figure 4.6e. The variation in pore diameter and pore wall thickness for PB-*b*-PEO- versus PEP-*b*-PEO-templated ITO films can be explained by their structural difference. Our PB-*b*-PEO is a larger polymer with $M_{w,total}$ = 10500 g/mol, compared to PEP-*b*-PEO with $M_{w,total}$ = 7900 g/mol. Therefore, it is expected to form larger micelles in solution leading to larger pores. In addition, the PEO block in PB-*b*-PEO is larger than the PEO block in PEP-*b*-PEO which should lead to thicker pore walls, since the particles co-assemble with the PEO block of the micelles to form the pore walls during synthesis.

Figure 4.3c-d shows top-view SEM images of Mn_3O_4 nanocrystals with an average diameter of 4-5 nm that were templated with PBO-*b*-PEO by dip-coating (Figure 4.3c) and spin-coating (Figure 4.3d). Both PB-*b*-PEO and PBO-*b*-PEO templates were thermally decomposed at 450 °C in air. Interestingly, the total molecular weight of PBO-*b*-PEO is larger than that of PB-*b*-PEO and PEP-*b*-PEO, however, the average pore diameter was found to be 13 ± 1 nm with an average pore wall thickness of 6-8 nm which are both smaller. This is corroborated with 2D-SAXS data (Figure 4.6f), which shows an average pore-to-pore distance of 28 nm, which is smaller than the averages for the PB-*b*-PEO- or PBO-*b*-PEO-templated systems. The smaller mesostructure can be attributed to the less hydrophobic/more hydrophilic nature of the PBO block compared to PB and PEP. Some nanoparticles may associate with the nominally hydrophobic block, leading to a smaller pore. More likely, because of the increased solubility of the PBO-*b*-PEO polymer in polar solvents, the polymer may have a lower aggregation number,

which could also lead to smaller-sized micelles in solution. Lower aggregation number also explains the combination of a smaller average pore diameter and a smaller pore wall thickness, which would lead to the shorter pore-to-pore distance observed in SAXS.

Figure 4.3e shows a top-view SEM image of ITO nanocrystals with an average diameter of 7.3 ± 0.7 nm that were templated with PEP-*b*-PEO by drop-casting. To prepare these films, nanocrystal/polymer solution was drop cast onto a polar substrate and the solvent was allowed to evaporate in air at room temperature. The films were heated to 450 °C to thermally decompose the polymer template. The film in Figure 4.3e had an average thickness of 2.0 ± 0.1 μm based on profilometry measurements. The average pore diameter was found to be 15 ± 3 nm, which is in agreement with the films in Figure 4.2 that were also templated with PEP-*b*-PEO. The drop-cast films show somewhat more disordered porosity, compared with dip-coated and spin-coated films. However, it is important to note that these films are at least one order of magnitude thicker than either dip-coated or spin-coated films and from a macroscopic perspective, the porosity is still homogeneous.

As described above, the method used to deposit films plays a role in the final film architecture. On average, spin-coating produces the thinnest films ranging from 100 to 120 nm thick after calcination by profilometry measurements. A single dip-coating process produces films ranging from 120 to 220 nm after calcination. It was also found that multiple coatings could be used to make thicker films; for example, double-dipped films up to 400 nm could be produced. To produce thicker films, drop-casting can be used. Drop casting is a viable method for generating films in the 1 – 5 μm range.

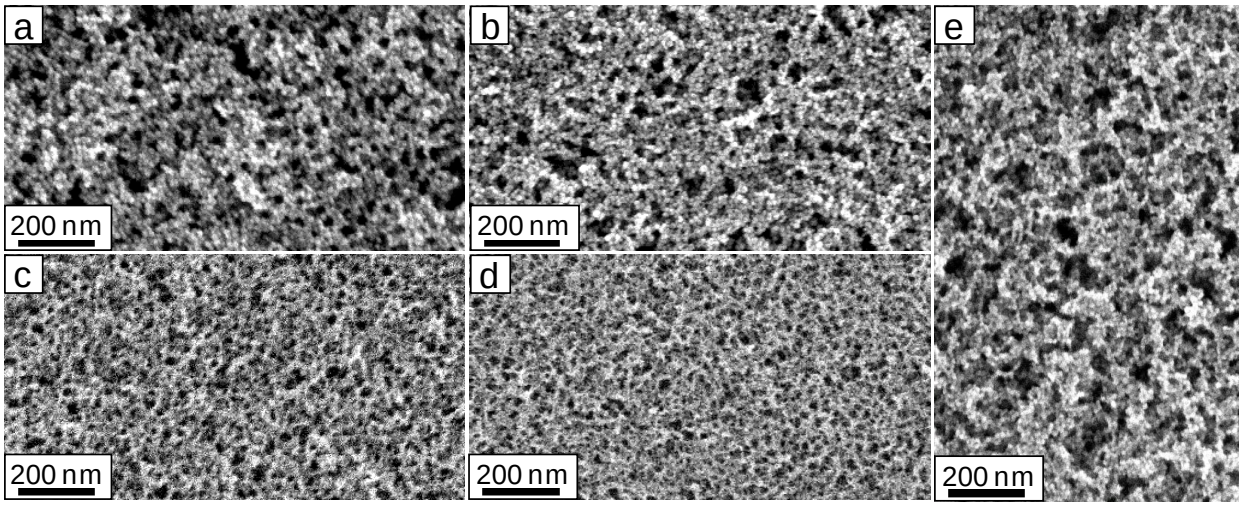

Figure 4.3. SEM images of templated nanocrystal-based porous films demonstrating variability of the template and coating method. Low-magnification top-view SEM images of PB-*b*-PEO templated ITO nanocrystals prepared by dip-coating (a) and spin-coating (b). Low-magnification top-view SEM images of PBO-*b*-PEO templated Mn_3O_4 nanocrystals prepared by dip-coating (c) and spin-coating (d). (e) SEM image of PEP-*b*-PEO templated ITO nanocrystals prepared by drop-casting.

A comparison of films prepared by dip-coating (Figure 4.3a and 4.3c), spin-coating (Figure 4.2b and 4.2d) and drop-casting (Figure 4.3e) reveals that surface roughness increases from spin-coated < dip-coated < drop-casted films. This can be explained by differences in the drying kinetics for each coating technique. In drop-casted films, the solvent evaporates very slowly and this can lead to inhomogeneous drying, especially near the surface of the film. During dip-coating, the solvent evaporates faster than for drop-casted films but slower than spin-coated films, and these variations in evaporation rate can lead to small variations in surface roughness. On the other hand, spin-coating involves very fast evaporation of the solvent, producing films with a more homogeneous thickness. For most sol-gel based block copolymer template materials, spin coating produces significantly less ordered materials because there is not enough time for hydrolysis and condensation reactions to occur during the film deposition process.[73-75] In this case, however, no chemistry occurs during film deposition, and so the pore structure in all cases is similar, indicating that all methods are viable routes to film deposition. This combination of results demonstrates the robustness of this nanocrystal-templating strategy and indicates that homogeneous, nanoporous nanocrystal-based films can likely be made by any solution phase deposition route, including industrially scalable methods such as doctor-blading or roll-to-roll deposition.

Another route to structural variation in these materials focuses on the ability to perform thermally induced solid-state conversion reactions in nanoporous materials with retention of the intrinsic nanostructure.[68,76] While many different kinds of nanocrystals can be produced, there are still more materials that have not yet been made as soluble nanocrystals. Solid state transformation thus provides a route to expand the palate of accessible materials. Thermal treatments stringent enough to drive a solid-solid transformation can, however, lead to

destruction of the periodicity and obstruction of the porosity from grain growth particularly at high temperatures. Here, we show one example of a transformation that can occur with-in our nanocrystal based nanoporous materials with retention of nanometer scale architecture.

It is well known that spinel structured ferrites can be converted to materials with a hematite structure upon thermal treatment in air.[77] The data in Figure 4.4 demonstrates this type of solid-state conversion reaction in a PEP-*b*-PEO-templated $MnFe_2O_4$ nanocrystal thin-film. The spinel ferrite (Figure 4.4a), is converted to a mixed oxide $(Mn,Fe)_2O_3$ system (Figure 4.4b). The conversion of bulk spinel (cubic) $MnFe_2O_4$ phase to the hematite (rhombohedral) $(Mn,Fe)_2O_3$ phase in air at elevated temperatures (>650 °C) has been reported to occur by oxidation of the Mn^{2+} in the spinel to Mn^{3+} resulting in a solid solution of Fe_2O_3 and Mn_2O_3 with a hematite crystal structure.[77] The films in Figure 4.4a were heated to 350 °C to thermally decompose the polymer template while still retaining the ferrite phase. Interestingly, in the templated nanocrystal-based films, thermal conversion to hematite occurs at only 400 °C which is significantly lower than the bulk conversion temperature. This result is consistent with the established fact that phase transitions in nanocrystals can occur at very different points than those in the bulk systems.[78,79] More importantly, the films retain the nanoscale architecture and open porosity. Figure 4.4c shows WAXD data collected on converted $(Mn,Fe)_2O_3$ films. The peaks can be indexed to the hematite phase of iron oxide with a rhombohedral crystal structure (JCPDS reference card no. 08-2902) with no indication of the spinel phase suggesting complete conversion. Scherrer analysis of the peak widths gives an average grain size of ~40 nm indicating that there is grain growth during thermal conversion. Some nanocrystals can still be seen in the SEM image, however, suggesting an inhomogeneous distribution of grain sizes. Interestingly, the grain growth observed during the ferrite to hematite transition implies that the

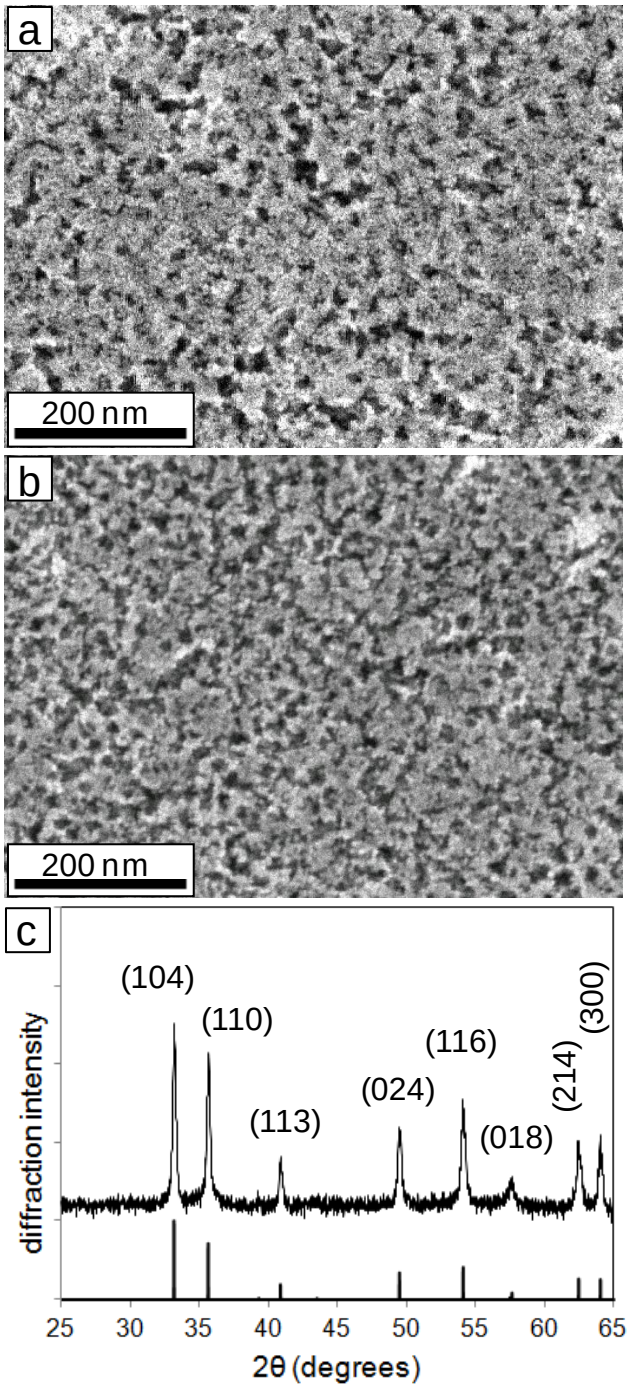

Figure 4.4. (a) SEM image of PEP-*b*-PEO templated $MnFe_2O_4$ nanocrystal-based films. (b) SEM image of $MnFe_2O_4$ films in (a) that were thermally converted to $(Mn,Fe)_2O_3$ at 400 °C demonstrating retention of mesostrucuture. (c) WAXD data suggests full conversion from $MnFe_2O_4$ to $(Mn,Fe)_2O_3$.

many nanocrystals of ferrite can convert into larger single hematite crystals with large diameters and while preserving the pore structure. The key feature to note is that the nanostructure is not destroyed, and that comparison of Figures 4.4a and b shows qualitatively similar porosity. This type of conversion reaction can become important when recipes for producing nanocrystals of a particular composition are not available.

4.2.3 Structural Characterization

While the SEM images presented in Figures 4.2 – 4.4 provide the most direct route to visualize these porous networks, they provide information only about a small surface region of the film, and they provide no information about the atomic scale structure of the films. To further characterize the structure of these nanocrystal-based nanoporous materials, we utilize a combination of low and high angle X-ray scattering, combined with ellipsometric porosimetry. Analysis of the crystal structure was carried out using wide angle X-ray diffraction (WAXD) measurements. Figure 4.5a shows WAXD patterns for ITO nanocrystals as-synthesized (A), after $NOBF_4$ treatment (B) and after templating with PEP-*b*-PEO (C). In all three patterns (A-C), the evolution of the main peaks can be indexed to the cubic phase (bixbyite) of In_2O_3 with Sn doped into the lattice (JCPDS reference card no. 06-0416). Scherrer analysis of the peak widths for ITO nanocrystals as-synthesized (A) and after $NOBF_4$ treatment (B) gives in an average domain size of 7-8 nm which is consistent with the particle size found in TEM data (Figure 4.1a-b). In (C), the average domain size of nanocrystals does not change after templating with PEP-*b*-PEO which is consistent with SEM data (Figure 4.2a-b) that shows individual nanocrystals comprising the pore walls of the films. The relative intensities of the peaks also suggest the nanocrystals embedded in the pore walls are randomly oriented. The fact that there is no phase-transformation or grain

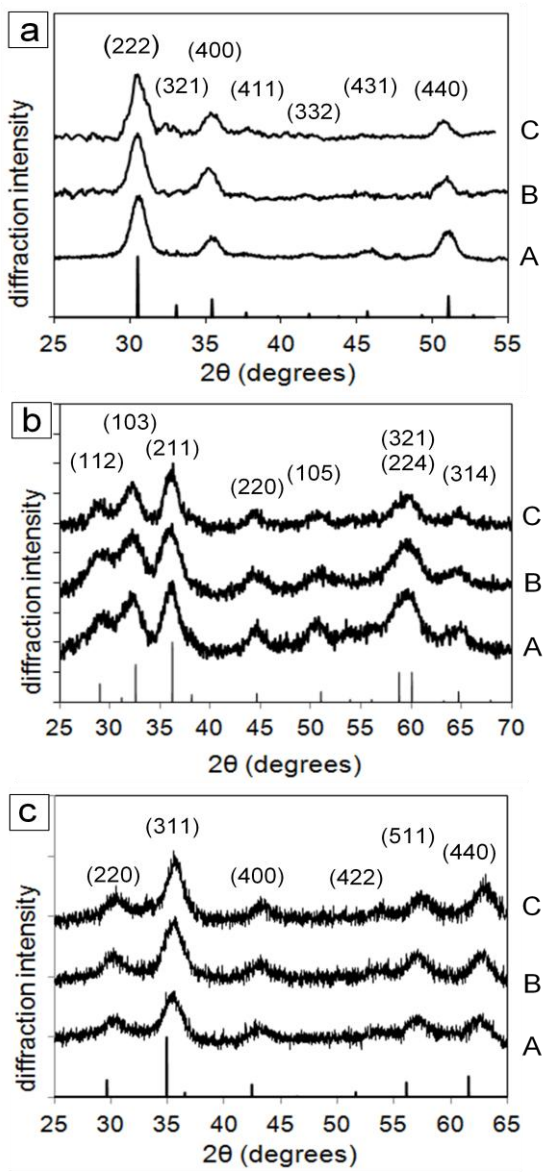

Figure 4.5. (a) WAXD patterns of as-synthesized ITO nanocrystals (A), ITO nanocrystals after the ligand-exchange process (B) and a templated ITO nanocrystal-based film (C). (b) WAXD patterns of as-synthesized Mn_3O_4 nanocrystals (A), Mn_3O_4 nanocrystals after the ligand-exchange process (B), and a templated Mn_3O_4 nanocrystal-based film (C). (c) WAXD patterns of as-synthesized $MnFe_2O_4$ nanocrystals (A), $MnFe_2O_4$ nanocrystals after the ligand-exchange process (B), and a templated $MnFe_2O_4$ nanocrystal-based film (C).

growth during thermal decomposition of the polymer suggests the nanocrystals are thermally stable.

Similar trends were observed in both Mn_3O_4 (Figure 4.5b) and $MnFe_2O_4$ (Figure 4.5c) systems when examined by WAXD. Figure 4.5b shows patterns for Mn_3O_4 nanocrystals as-synthesized (A), after $NOBF_4$ treatment (B) and after templating with PEP-*b*-PEO (C). The XRD patterns for (Figure 4.5b (A-C)) can be assigned to the tetragonal Mn_3O_4 (hausmannite) structure (JCPDS reference card no. 80-0382). Scherrer analysis of the peak widths in all three patterns gives an average size of 4-5 nm, which is in agreement with TEM data (Figure 4.1e-f). Finally, for the $MnFe_2O_4$ system (Figure 4.5c), the main peaks in all three patterns, as-synthesized (A), after $NOBF_4$ treatment (B) and after templating with PEP-*b*-PEO (C), can be indexed to the cubic phase of manganese ferrite (JCPDS reference card no. 02-8666). The average grain size for (A-C) was found to be 4-5 nm (Scherrer analysis) again confirming that the particle size is not affected by the $NOBF_4$ treatment[53] or thermal treatments, corroborating TEM (Figure 4.1c-d) and SEM data (Figure 4.4a). As in the case for ITO, analysis of the peak intensities for both Mn_3O_4 and $MnFe_2O_4$ also reveal that the pore walls are made up of nanocrystals with random orientations. Overall, the WAXD data shown here confirm the nanocrystals for all three systems are chemically stable during $NOBF_4$ treatment[53] and thermally stable during the decomposition of the polymer. In addition, the data indicates that the nanocrystals are fully crystalline before the templating step, confirming they are in fact pre-formed and ready to serve as architectural building blocks.

The nanoscale architecture was further characterized by 2D-SAXS experiments, which were collected on beamline 1-4 at the Stanford Synchrotron Radiation Laboratory. Measurements were carried out in reflection mode with the incoming beam at grazing or near

grazing incidence. Here we define the incident angle (i.e. the angle between the X-ray beam and the plane of the substrate) as β. Higher β angles bias the diffraction against the out-of-plane scattering and are thus used for the more ordered samples to produce more even intensities around the ring. Figure 4.6 shows 2D-SAXS patterns collected for PEP-*b*-PEO templated films of ITO at β = 1.25° (a), Mn_3O_4 at β = 2.25° (b), $MnFe_2O_4$ β = 0.80° (c) and $(Mn,Fe)_2O_3$ β = 0.80°. In the ITO-based films (a) the evolution of a diffuse ellipsoidal ring with a strong in-plane scattering maxima along the x-direction is observed corresponding to an average repeat distance of 32 nm. The observed pattern is characteristic of a disordered material with a homogeneous length scale. During thermal decomposition of the polymer template, the films experience anisotropic contraction of the pores in the direction perpendicular to the plane of the substrate, which also explains the ellipsoidal shape.

The observed 2D-SAXS data for Mn_3O_4 (Figure 4.6b) shows strong in-plane scattering maxima with an average repeat distance of 32 nm. The pattern shows a less-defined ellipsoidal ring with less scattering in the z-direction. This type of pattern often occurs in partly disordered thin film systems. Because there are only 10-20 pore repeats through the thickness of the film, this is insufficient to produce strong constructive interference in the out-of plane direction when disorder is included. The scattering length in the x- and y-directions is much greater, however, so constructive interference is observed even in partly disordered systems. The in-plane scattering maxima for both $MnFe_2O_4$ (Figure 4.6c) and $(Mn,Fe)_2O_3$ (Figure 4.6d) films also corresponds to an average repeat distance 32 nm.

The fact that all four types of films exhibit a similar average repeat distance is consistent with the fact that the PEP-b-PEO template directs the mesostructure and nanoscale architecture. Moreover, an average repeat distance of 32 nm is approximately commensurate with the sum of

the average pore diameter and pore wall thickness that was estimated from SEM for all the PEP-*b*-PEO templated nanocrystal-based materials discussed thus far. For the PB-*b*-PEO film shown in Figure 4.6e, a large repeat distance is observed, again consistent with SEM and the large polymer size employed in the synthesis. Finally, for the PBO-*b*-PEO templated samples shown in Figure 4.6f, a smaller repeat distance is found. The reasons this polymer produces a smaller repeat distance were discussed above. While the specific repeat distances shown in Figure 4.6 corroborate the conclusions from SEM, the SAXS data also provide additional information. Specifically, all of the SEM images in Figures 4.2 – 4.4 appear to show similar levels of disorder. Examination of the SAXS data, however, shows that PEP-*b*-PEO template films are actually somewhat more ordered at the nanometer scale than films synthesized using PB-*b*-PEO or PBO-*b*-PEO. Perhaps more importantly, the fact that scattering data can be observed for all films in 2D-SAXS regardless of the level of disorder, confirms that all films show homogeneity of the porosity at the nanoscale. For most applications, it is this homogeneity of pore size and wall thickness, rather than pore periodicity that is most important.[35]

To study the effects of nanocrystal size on the porous architecture, ITO nanocrystals with an average diameters of 4.6 ± 0.4 nm (Figure 4.7a) and 7.3 ± 0.7 nm (Figure 4.7e)[56-58] were templated with PEP-*b*-PEO. For both films the average size of the mesopores by SEM was found to be 17 ± 3 nm arising from the template. TEM images of 4.6 ± 0.4 nm ITO (Figure 4.7b) and 7.3 ± 0.7 nm ITO (Figure 4.7f) nanocrystals after $NOBF_4$ treatment show the particles are free of agglomeration with a uniform size and shape.[53] The micro- and mesoporosity was further analyzed by ellipsometric porosimetry measurements using toluene as the adsorbate.[80] Adsorption-desorption isotherms for both templated 4.6 ± 0.4 nm ITO (Figure 4.7c) and 7.3 ± 0.7 nm ITO (Figure 4.7g) nanocrystals show typical type IV behavior.[81] For this type of

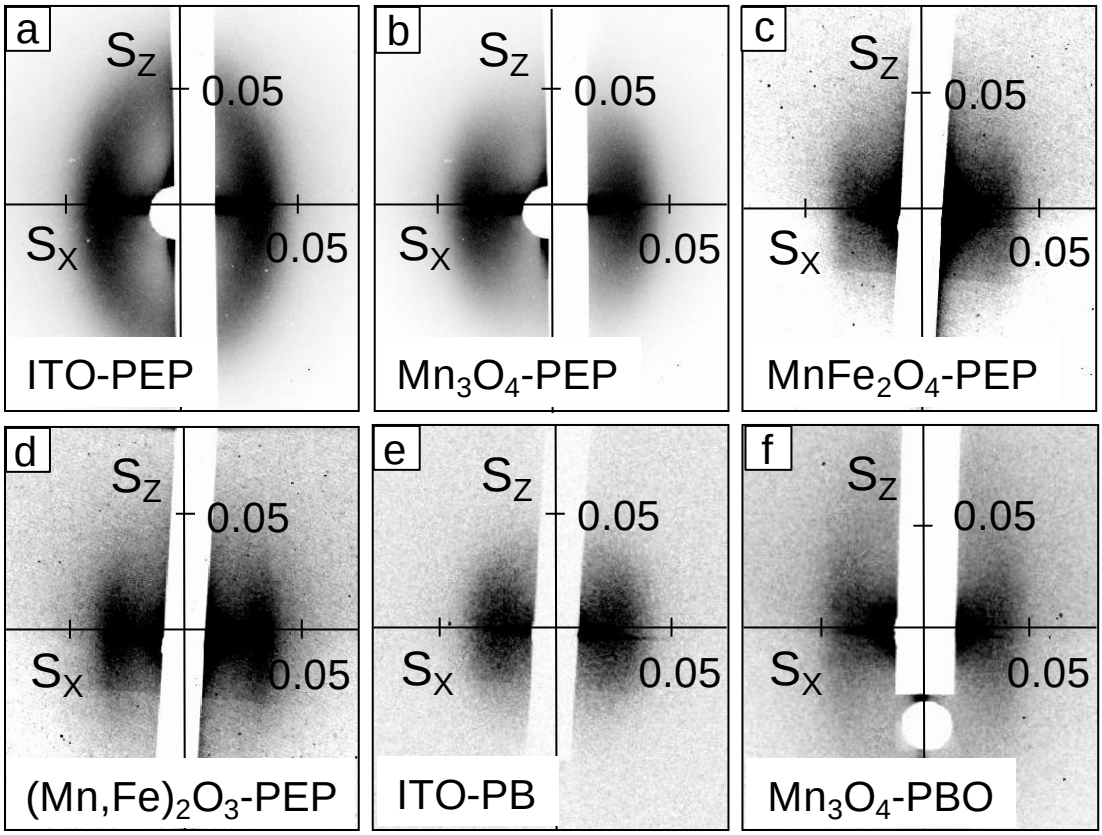

Figure 4.6. 2D-SAXS patterns obtained on PEP-*b*-PEO templated ITO-based films (a), Mn_3O_4-based films (b), $MnFe_2O_4$-based films (c), and $(Mn,Fe)_2O_3$-based films (d). Patterns for PB-*b*-PEO templated ITO nanocrystal-based films (e) and PBO-*b*-PEO templated Mn_3O_4 nanocrystal-based films. Data were collected at an angle of incidence β = 1.25° for (a), β = 2.25° for (b), β = 0.80° for (c), and β = 0.80° for (d), β = 0.80° for (e) and β = 0.60° for (f). Scattering vector s components are given in 1/nm.

physisorption behavior, the presence of a hysteresis loop at higher relative pressures is representative of a mesoporous structure with interconnected porosity. The adsorption curve describes the pore size of the cages, and the desorption curve reveals the pore size of the necks. For 4.6 ± 0.4 nm ITO, a Kelvin model fit to the isotherm (Figure 4.7c) produces a pore diameter distribution centered at 22 nm and a neck-diameter distribution centered at 12 nm, as shown in Figure 4.7d. The Dubinin-Radushkevich model was further fit to the isotherm at lower relative pressures to examine the micropores in these materials. Average micropore sizes for films made from 4.6 ± 0.4 nm ITO nanocrystals were 1.2 nm (cage diameter from adsorption) and 0.8 nm (neck diameter from desorption). These micropores arise from the spaces in between the randomly agglomerated nanocrystals that make up the pore walls. A fit to the 7.3 ± 0.7 nm ITO isotherm (Figure 4.7g) gives a mesopore diameter size distribution centered on 22 nm with an average neck diameter centered on 12 nm as shown in Figure 4.7h, as expected, since both films were prepared with the same polymer template. Interestingly, the micropores in this case were found to have 1.6 nm cages and 1.0 nm necks, which are larger, confirming that the size of the nanocrystals defines the micropore structure. The isotherm for the 4.6 ± 0.4 nm ITO templated films shows a 55% toluene-accessible porous volume, while for the 7.3 ± 0.7 nm ITO templated films it shows a 50% total pore volume.

Additional ellipsometric porosimetry measurements were carried out for PB-*b*-PEO templated 7.3 ± 0.7 nm ITO nanocrystals (Figure 4.8a-b) and PEP-*b*-PEO templated 4.8 ± 0.5 nm Mn_3O_4 nanocrystals (Figure 4.8c-d). For PB-*b*-PEO ITO, a fit to the isotherm (Figure 4.8a) gives a pore diameter size distribution centered on 30 nm with an average neck diameter centered on 15 nm as shown in Figure 4.8b. The larger mesopores determined by porosimetry are in

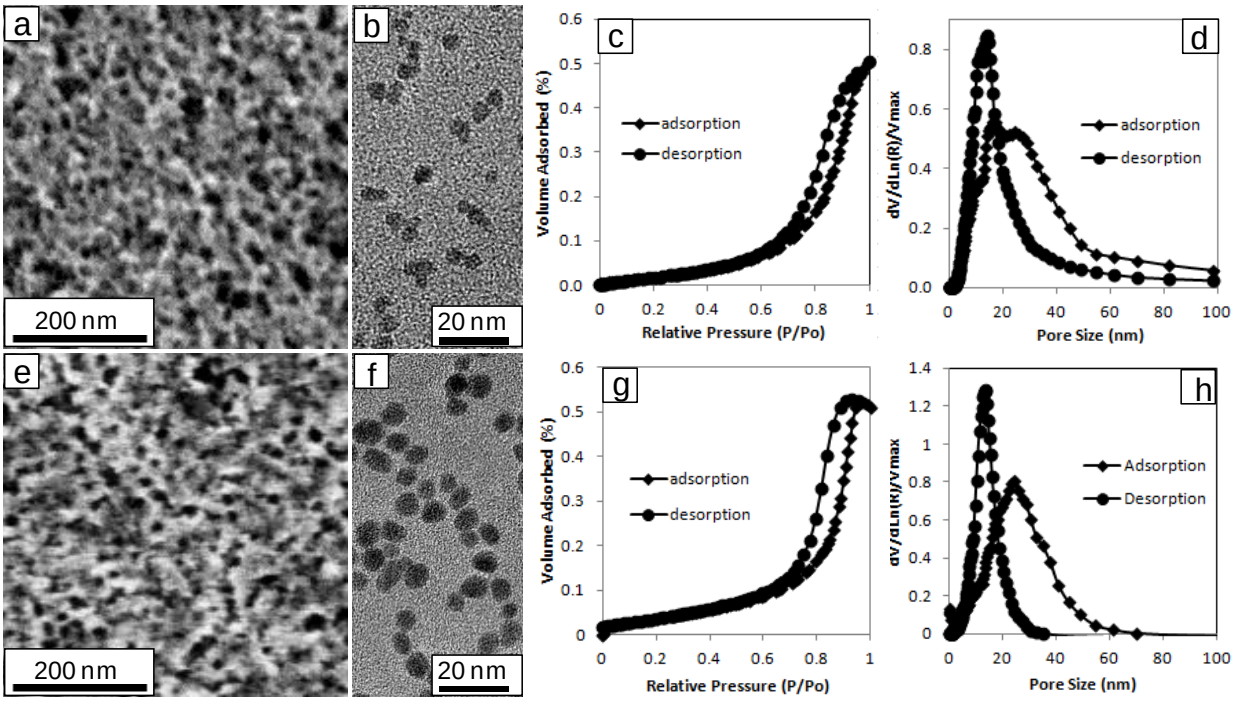

Figure 4.7. (a) SEM image of PEP-*b*-PEO templated ITO nanocrystals with a diameter of 4-5 nm. (b) TEM image of the $NOBF_4$-treated ITO nanocrystals. (c) A typical toluene adsorption-desorption isotherm showing characteristic mesoporous behavior for films shown in (a). (d) Pore size distribution data obtained from the isotherm in (c). (e) SEM image of 7-8 nm ITO nanocrystals templated with PEP-*b*-PEO. (f) TEM image of the $NOBF_4$-treated ITO nanocrystals. (g) Toluene adsorption-desorption isotherm showing characteristic mesoporous behavior. (h) Pore size distribution data obtained from the isotherm in (g).

reasonable agreement with SEM and 2D-SAXS discussed earlier arising from the larger size of the PB-*b*-PEO template. The micropores, however, show 1.6 nm cages and 1.0 nm necks, similar to that of 7.3 ± 0.7 nm ITO templated with PEP-*b*-PEO, again confirming that the nanocrystal size dictates the microporous structure. Figure 4.8c shows a typical isotherm obtained for PEP-*b*-PEO templated Mn_3O_4 films. In this case, the mesopores were found to be similar to those obtained from the data in Figure 4.7c and g, with an average pore and neck size of 23 nm and 13 nm – as expected from the fact that all three samples used the same PEP-*b*-PEO template. The micropores were found to have 1.4 nm cages and 1.0 nm necks. The isotherm for the PB-*b*-PEO ITO shows a 45% toluene-accessible porous volume, while PEP-*b*-PEO Mn_3O_4 shows a 70% total pore volume. Table 1 summarizes the porosity data showing nanocrystal-based templated films exhibit a bimodal porosity where the micropore size can be tuned by changing the size of the pre-formed nanocrystals and the mesopores size can be tuned by changing the size and chemical nature of the template. Overall, the pore analyses found here corroborate the observations from SEM, TEM, WAXD and 2D-SAXS described earlier in all systems studied.

To demonstrate the advantage of our high surface area mesoporous architecture materials we examined the electrochemical properties of a templated Mn_3O_4 nanocrystal-based mesoporous film and compared it to an untemplated film, cast from the same ligand-free nanocrystals. Figure 4.9 shows a comparison of charging times calculated from cyclic voltammetric data at various sweep rates for a PEP-*b*-PEO templated Mn_3O_4 nanocrystal-based mesoporous film (squares) and an untemplated Mn_3O_4 nanocrystal film (circles) cycled in a non-aqueous electrolyte. The data shows significant differences in charging behavior for the two films. The most obvious trend is the total capacity – after 500 s, the total charge stored in the

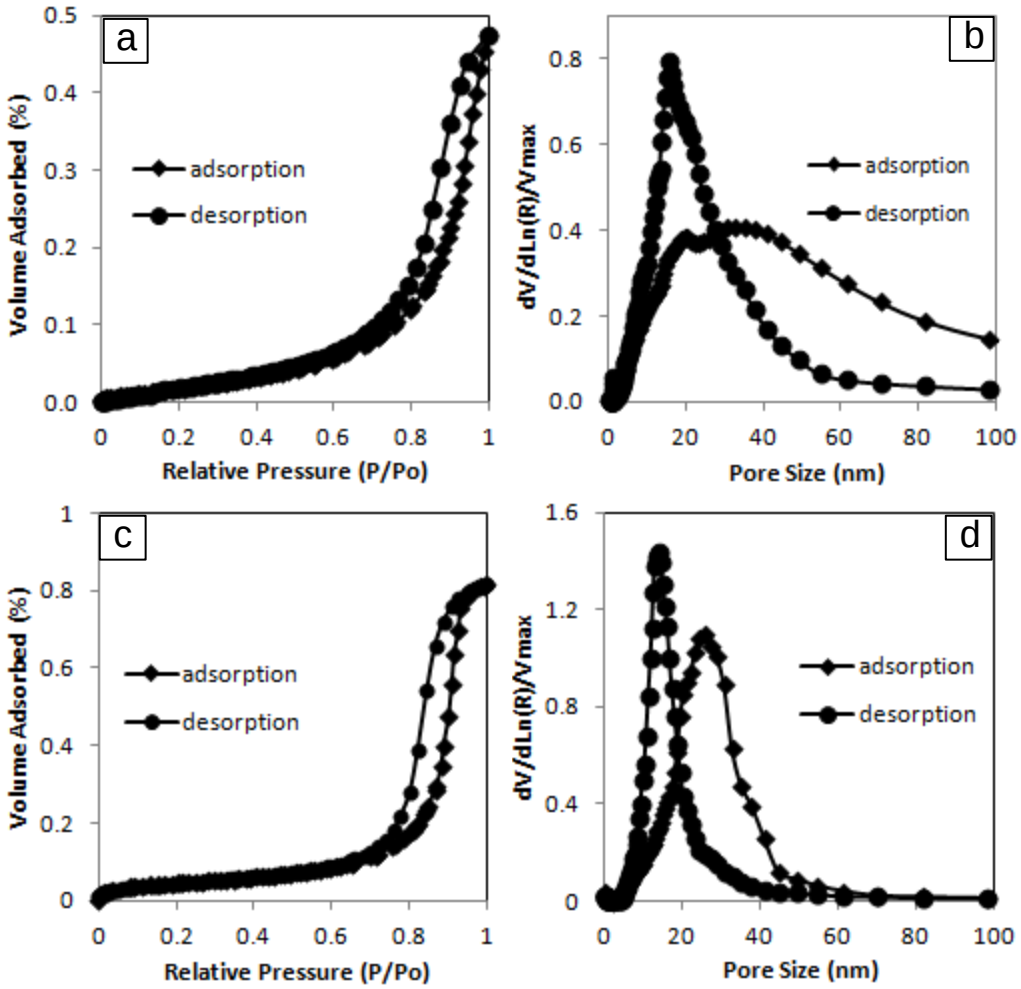

Figure 4.8. Toluene adsorption-desorption isotherms for PB-*b*-PEO templated ITO nanocrystals with a diameter of 7-8 nm (a) and PEP-*b*-PEO templated Mn_3O_4 nanocrystals with a diameter of 4-5 nm (c). Corresponding pore size distribution data for PB-*b*-PEO templated ITO (b) and PEP-*b*-PEO templated Mn_3O_4 (d) obtained from the isotherms.

Table 4.1 Summary of mesopore size arising from the block copolymer template and micropore size arising from nanocrystal size.

Polymer / Nanocrystal Size	$M_{w,total}$[a] (g/mol)	f_w hydrophobic block[b]	f_w PEO block[c]	Cage Size (nm)[d] (mesopore from Polymer) (micropore from Nanocrystal)	Neck Size (nm)[e] (mesopore from Polymer) (micropore from Nanocrystal)
PEP-*b*-PEO	7900	0.49	0.51	22	12
PB-*b*-PEO	10500	0.52	0.48	30	15
PBO-*b*-PEO	1500	0.57	0.43	16	9
ITO – 4.6 nm				1.2	0.8
ITO – 7.3 nm				1.6	1.0
Mn_3O_4 – 4.8 nm				1.4	1.0

[a] Total molecular weight of the block copolymer template, [b] weight fraction for the hydrophobic block, [c] weight fraction for the PEO block, [d] average cage size for mesopores arising from the template or micropores arising from the nanocrystal size, [e] average neck size for mesopores arising from the template or micropores arising from the nanocrystal size.

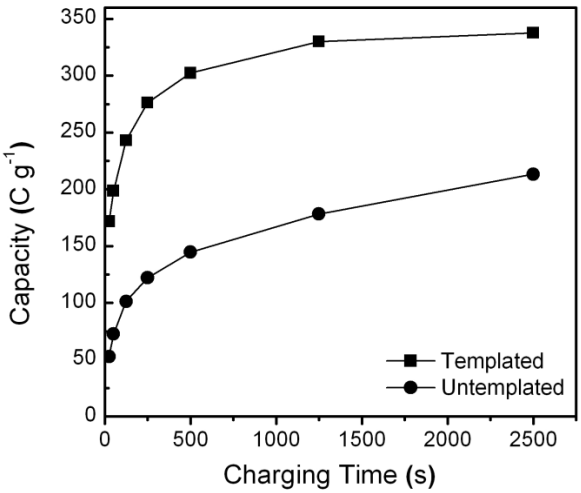

Figure 4.9. Comparison of capacity at various charging times calculated from cyclic voltammetric data at various sweep rates for a PEP-*b*-PEO templated Mn_3O_4 nanocrystal-based mesoporous film (squares) and an untemplated Mn_3O_4 nanocrystal film (circles).

templated film is about 300 C/g, twice the amount of charge compared to the untemplated film (150 C/g). Perhaps more important is the time dependant trends. After 1200 s the templated film is fully charged while the capacity in the untemplated films is still increasing at 2500 s. The templated film stores more charge than the untemplated film because the pore structure maximizes surface area and thus accessible redox sites. Moreover, comparison of the templated film to the untemplated film shows that the open and interconnected porosity enhances charge storage kinetics by facilitating ion/electrolyte diffusion to the redox sites.

4.3 Conclusions

In this work, we describe a general route for assembling pre-formed nanocrystals into hierarchical mesoporous architectures. By tailoring the nanocrystal composition and size along with the block copolymer template type and size, the methodology presented here can offer a high degree of synthetic and structural control over the final architecture of the material. In addition, the ability to perform solid state conversion reactions while retaining the structure/porosity was also demonstrated. The $NOBF_4$ ligand-exchange method used here resulted in soluble nanocrystals without any particle etching or growth, or change in crystal structure, suggesting this general method may be extended to a wider range of functional nanocrystals. As a demonstration of the utility of these materials we show enhanced charge storage kinetics for porous Mn_3O_4 films. Many of the polymer templates used here are commercially available, indicating that this is a generally accessible route to the production of nanocrystal based nanoporous materials. Moreover, while the materials presented here showed homogeneous, but disordered porosity, recent advances using custom synthesized polymers indicate that highly ordered materials can also be produced from ligand-stripped nanocrystals.[82]

Taken together, this work provides a general strategy for harnessing the incredible synthetic diversity of nanocrystal-based materials and using it for the production of nanoporous materials. This general route should be applicable to many nanocrystals systems for a wide range of applications.

4.4 Experimental

4.4.1 Materials. The following chemicals were purchased and used as received: oleylamine (90% Aldrich), oleic acid (90%, Aldrich), stearic acid (95%, Aldrich), xylene (98%, Aldrich), manganese(II) acetate (98%, Aldrich), indium acetylacetonate (99.99+%, Aldrich), tin bis(acetylacetonate) dichloride (98%, Aldrich), manganese(II) acetylacetonate (Aldrich), iron(III) acetylacetonate (97% Aldrich), 1,2-hexadecanediol (90%, aldrich), benzyl ether (98%, aldrich), nitrosonium tetrafluoroborate (95%, Aldrich). Poly(butadiene(1,2 addition))-*b*-poly(ethylene oxide), with a mass ratio of PB(5500)-*b*-PEO(5000), a block ratio of PB_{102}-*b*-PEO_{114}, and with a polydispersity index (PDI) = 1.05, was purchased from Polymer Source, Inc. Poly(butylene oxide)-*b*-poly(ethylene oxide), with a mass ratio of PBO(5000)-*b*-PEO(6500), a block ratio PBO_{90}-b-PEO_{114}, and with a PDI = 1.09 was purchased from Advanced Polymer Materials Inc. Poly((ethylene-*alt*-propylene)-*block*-poly(ethylene oxide), with a mass ratio of PEP(3900)-*b*-PEO(4000), a block ratio of PEP_{56}-*b*-PEO_{91}, and with a PDI = 1.05, was synthesized using reported methods.[83-84] Briefly, polyisoprene was grown by anionic polymerization, terminated with an -OH group and then hydrogenated over Pd/C. The resulting PEP-OH was subsequently extended by anionic polymerization of ethylene oxide.

*4.4.2 Synthesis and Ligand-exchange of Nanocrystals***.** Previously reported procedures were followed to synthesize 7-8 nm and 4-5 nm ITO nanocrystals,[56-58] 4-5 nm $MnFe_2O_4$ nanocrystals,[60] and 4-5 nm Mn_3O_4 nanocrystals,[59] all of which were stabilized by either oleylamine or oleic acid ligands. All as-synthesized nanocrystals were purified and dispersed in hexane (10-15 mg/mL). To carry out the ligand-exchange process, as-synthesized nanocrystals were treated with $NOBF_4$ according to a recently reported procedure.[53] In a typical ligand-exchange reaction, 5 mL of nanocrystal dispersion in hexane was combined with 5 mL of $NOBF_4$ solution in N, N-dimethylformamide (DMF) (10 mg/mL) with stirring (5 min), or until the nanocrystals were transferred to the DMF phase. The nanocrystals were precipitated with toluene then centrifuged, followed by multiple washings with DMF/toluene. The ligand-stripped nanocrystals were dispersed in DMF/ethanol (1:10 v/v) to give a final concentration of 15-20 mg/mL.

*4.4.3 Synthesis of Mesoporous Nanocrystal-based Films***.** In a typical synthesis, 40 mg of the desired diblock copolymer was dissolved in 0.5 mL of ethanol with gentle heating. To this solution, 3 mL of the desired nanocrystals in DMF/ethanol (20 mg/mL) was added. From this mixture, thin films were produced by dip-coating onto polar substrates at a constant withdrawal rate of 1-10 mm/s with a constant 30% relative humidity. Thin films were also prepared by spin-coating onto polar substrates at 1000 to 2000 rpm for 60 s. Finally, thick films could be produced by drop casting onto polar substrates. In most cases, some optimization of the exact concentration of diblock copolymer and nanocrystal was required for mesostructure optimization. The films were dried using a 3 h ramp up to 175 °C, followed by a 3 h soak. Thermal decomposition of the template was done after the drying step using a 6 h ramp from 175 °C to 450 °C for ITO and Mn_3O_4 films and to 350 °C for $MnFe_2O_4$ films, followed by a 3 h soak.

4.4.4 Methods. Transmission electron microscopy (TEM) images were obtained using an FEI/PHILIPS CM120 electron microscope operating at 120 kV, as well as a JEOL-2100 electron microscope operating at 200 kV. Scanning electron microscopy (SEM) images were obtained using a JEOL model 6700F electron microscope with beam energy 5 kV, and with a Zeiss Gemini Ultra-55 Analytical electron microscope with beam energy 5 kV. Conventional wide-angle X-ray diffraction (WAXD) measurements were carried out on a Bruker D8-GADDS diffractometer with $Cu_{K\alpha}$ radiation, and on a Panalytical XPert PRO MPD diffractometer, again with $Cu_{K\alpha}$ radiation. 2D small-angle X-ray scattering (2D-SAXS) data were collected at the Stanford Synchrotron Radiation Laboratory using beamline 1-4 using the Rayonix165 large angle CCD detector. All measurements were performed in reflection geometry. Ellipsometric porosimetry was performed on a PS-1000 instrument from Semilab using toluene and as the adsorbate. A UV–visible CCD detector adapted to a grating spectrograph analyzes the signal reflected by the sample. The light source is a 75 W Hamamatsu Xenon lamp and measurements were performed on the spectral range from 1.24-4.5 eV. Data analysis was performed using the associated WinElli II software. Electrochemical measurements were carried out in a three-electrode cell using a PAR EG&G 273A potentiostat in an argon-filled glovebox, with oxygen and water levels <1 ppm. The working electrode consisted of ITO glass upon which Mn_3O_4 films were deposited. The electrolyte solution used was 1.0 M $LiClO_4$ in propylene carbonate (PC) and lithium metal foils were used as the counter and reference electrodes. Cyclic voltammetry was performed using cutoff voltages at 4 and 1.5 V vs. Li/Li^+.

4.5 References

[1] Kresge, C. T.; Leonowicz, M. E.; Roth, W. J.; Vartuli, J. C.; Beck, J. S. Ordered Mesoporous Molecular Sieves Synthesized by a Liquid-Crystal Template Mechanism. *Nature* **1992**, *359*, 710-712.

[2] Beck, J. S.; Vartuli, J. C.; Roth, W. L.; Leonowicz, M. E.; Kresge, C. T.; Schmidt, K. D.; Chu, C. T.-W.; Olson, D. H.; Sheppard, E. W.; McCullen, S. B.; Higgins, J. B.; Schlenker, J. L. A New Family of Mesoporous Molecular Sieves Prepared with Liquid Crystal Template. *J. Am. Chem. Soc.* **1992,** *114*, 10834-10843.

[3] Zhao, D. Y.; Feng, J. L.; Huo, Q. S.; Melosh, N.; Fredrickson, G. H.; Chmelka, B. F.; Stucky, G. D. Triblock Copolymer Syntheses of Mesoporous Silica with Periodic 50 to 300 Angstrom Pores. *Science* **1998**, *279*, 548-552.

[4] Yanagisawa, T.; Shimizu, T.; Kuroda, K.; Kato, C. The Preparation of Alkyltrimethylamnonium-Kaneinite Complexes and Their Conversion to Microporous Materials. *Bull. Chem. Soc. Jpn.* **1990**, *63*, 988-992.

[5] Inagaki, S.; Fukushima, Y.; Kuroda, K. Synthesis of Highly Ordered Mesoporous Materials From a Layered Polysilicate. *J. Chem. Soc. Chem. Commun.* **1993**, 680-682.

[6] Ogawa, M. Formation of Novel Oriented Transparent Films of Layered Silica-Surfactant Nanocomposites. *J. Am. Chem. Soc.* **1994**, *116*, 7941-7942.

[7] Antonelli, D. M.; Ying, J. Y. Synthesis of Hexagonally Packed Mesoporous TiO2 by a Modified Sol–Gel Method. *Angew. Chem., Int. Ed. Engl.* **1995**, *34*, 2014-2017.

[8] Yang, H.; Kuperman, A.; Coombs, N.; Mamiche-Afara, S.; Ozin, G. A. Synthesis of Oriented Mesoporous Silica Films on Mica. *Nature* **1996**, *379*, 703-705.

[9] Monnier, A.; Schuth, F.; Huo, Q.; Kumar, D.; Margolese, D.; Maxwell, R. S.; Stucky, G. D.; Krishnamurty, M.; Petroff, P.; Firouzi, A.; Janicke, M.; Chmelka, B. F. Cooperative Formation of Inorganic-Organic Interfaces in the Synthesis of Silica Mesostructures. *Science* **1993**, *261*, 1299-1303.

[10] Brezesinski, K.; Haetge, J.; Wang, J.; Mascotto, S.; Reitz, C.; Rein, A.; Tolbert, S. H.; Perlich, J.; Dunn, B.; Brezesinski, T. Ordered Mesoporous α-Fe2O3 (Hematite) Thin-Film Electrodes for Application in High Rate Rechargeable Lithium Batteries. *Small* **2011**, *7*, 407-414.

[11] Sun, D.; Riley, A. E.; Cadby, A. J.; Richman, E. K.; Korlann, S. D.; Tolbert, S. H. Hexagonal Nanoporous Germanium Through Surfactant-driven Self-Assembly of Zintl clusters. *Nature* **2006**, *441*, 1126-1130.

[12] Stefik, M.; Sai, H.; Epps, T. H.; Bates, F. S.; Gruner, S. M.; DiSalvo, F. J.; Wiesner, U. Ordered Three- and Five-ply Nanocomposites from ABC Block Terpolymer Microphase Separation with Niobia and Aluminosilicate Sols. *Chem. Mater.* **2009**, *21*, 5466-5473.

[13] Deng, Y.; Yu, T.; Wan, Y.; Shi, Y.; Meng, Y.; Gu, D.; Zhang, L.; Huang, Y.; Liu, C.; Wu, X.; Zhao, D. Ordered Mesoporous Silicas and Carbons with Large Accessible Pores Templated from Amphiphilic Diblock Copolymer Poly(ethylene oxide)-b-polystyrene. *J. Am. Chem. Soc.* **2007**, *129*, 1690-1697.

[14] Cheng, Y. J.; Gutmann, J. S. Morphology Phase Diagram of Ultrathin Anatase TiO2 Films Templated by a Single PS-b-PEO Block Copolymer. *J. Am. Chem. Soc.* **2006**, *128*, 4658-4674.

[15] Mamak, M.; Coombs, N.; Ozin, G. Mesoporous Yttria–Zirconia and Metal–Yttria–Zirconia Solid Solutions for Fuel Cells. *Adv. Mater.* **2000**, *12*, 198-202.

[16] Warren, S. C.; Perkins, M. R.; Adams, A. M.; Kamperman, M.; Burns, A. A.; Arora, H.; Herz, E.; Suteewong, T.; Sai, H.; Li, Z.; *et. al*. A Silica Sol–Gel Design Strategy for Nanostructured Metallic Materials. *Nat. Mater.* **2012**, *11*, 460-467.

[17] Stefik, M.; Lee, J.; Wiesner, U. Nanostructured Carbon–Crystalline Titania Composites from Microphase Separation of Poly(ethylene oxide-b-acrylonitrile) and Titania Sols *Chem. Commun.* **2009**, 2532-2534.

[18] Tian, B. Z.; Liu, X. Y.; Tu, B.; Yu, C. Z.; Fan, J.; Wang, L. M.; Xie, S. H.; Stucky, G. D.; Zhao, D. Y. Self-Adjusted General Synthesis of Ordered Stable Mesoporous Minerals by Acid-Base Pairs. *Nat. Mater.* **2003**, *2*, 159-163.

[19] Finnemore, A. S.; Scherer, M. R. J.; Langford, R.; Mahajan, S.; Ludwigs, S.; Meldrum, F.; Steiner, U. Nanostructured Calcite Single Crystals with Gyroid Morphologies. *Adv. Mater.* **2009**, *21*, 3928-3932.

[20] Brezesinski, B.; Wang, J.; Senter, R.; Brezesinski, K.; Dunn, B.; Tolbert, S. H. On the Correlation Between Mechanical Flexibility, Nanoscale Structure, and Charge Storage in Periodic Mesoporous CeO2 Thin Films. *ACS Nano* **2010,** 4, 967-977.

[21] Yang, P.; Deng, T.; Zhao, D.; Feng, P.; Pine, D.; Chmelka, B.; Whitesides, G.; Stucky, G. D. Hierarchically Ordered Oxides. *Science* **1998**, *282*, 2244-2246.

[22] Freer, E. M.; Krupp, L. E.; Hinsberg, W. D.; Rice, P. M.; Hedrick, J. L.; Cha, J. N.; Miller, R. D.; Kim, H. C. Oriented Mesoporous Organosilicate Thin Films *Nano Lett.* **2005**, *5*, 2014-2018.

[23] Brezesinski, T.; Groenewolt, M.; Gibaud, A.; Pinna, N.; Antonietti, M.; Smarsly, B. M. Evaporation-Induced Self-Assembly (EISA) at Its Limit: Ultrathin, Crystalline Patterns by Templating of Micellar Monolayers. *Adv. Mater.* **2006**, *18*, 2260-2263.

[24] Grosso, D.; Boissière, C.; Smarsly, B.; Brezesinski, T.; Pinna, N.; Albouy, P. A.; Amenitsch, H.; Antonietti, M.; Sanchez, C. Periodically Ordered Nanoscale Islands and Mesoporous Films Composed of Nanocrystalline Multimetallic Oxides *Nat. Mater.* **2004**, *3*, 787-792.

[25] Kuemmel, M.; Grosso, D.; Boissière, U.; Smarsly, B.; Brezesinski, T.; Albouy, P. A.; Amenitsch, H.; Sanchez, C. Thermally Stable Nanocrystalline γ-Alumina Layers with Highly Ordered 3D Mesoporosity. *Angew. Chem., Int. Ed.* **2005**, *44*, 4589-4592.

[26] Docamp, P.; Guldin, S.; Stefik, M.; Tiwana, P.; Orilall, M. C.; Huttner, S.; Sai, H.; Wiesner, U.; Steiner, U.; Snaith, H. J. Control of Solid-State Dye-Sensitized Solar Cell Performance by Block-Copolymer-Directed TiO_2 Synthesis. *Adv. Func. Mater.* **2010**, *20*, 1787-1796.

[27] Zhao, D.; Huo, Q.; Feng, J.; Chmelka, B. F.; Stucky, G. D. Nonionic Triblock and Star Diblock Copolymer and Oligomeric Surfactant Syntheses of Highly Ordered, Hydrothermally Stable, Mesoporous Silica Structures. *J. Am. Chem. Soc.* **1998**, *120*, 6024-6036.

[28] Kondo, J. N.; Domen, K. Crystallization of Mesoporous Metal Oxides. *Chem. Mater.* **2008**, *20*, 835-847.

[29] Crepaldi, E. L.; Soler-Illia, G. J. A. A.; Grosso, D.; Sanchez, C. Nanocrystallised Titania and Zirconia Mesoporous Thin Films Exhibiting Enhanced Thermal Stability. *New J. Chem.* **2003**, *27*, 9-13.

[30] Crepaldi, E. L.; Soler-Illia, G. J. A. A.; Grosso, D.; Cagnol, F.; Ribot, F.; Sanchez, C. Controlled Formation of Highly Organized Mesoporous Titania Thin Films: from Mesostructured Hybrids to Mesoporous Nano-anatase TiO_2. *J. Am. Chem. Soc*. **2003**, *125*, 9770-9786.

[31] Warren, S. C.; Messina, L. C.; Slaughter, L. S.; Kamperman, M.; Zhou, Q.; Gruner, S. M.; DiSalvo, F. J.; Wiesner, U. Ordered Mesoporous Materials from Metal Nanoparticle-Block Copolymer Self-Assembly. *Science* **2008**, *320*, 1748-1752.

[32] Corma, A.; Atienzar, P.; Garcia, H.; Chane-Ching, J. Y. Hierarchically Mesostructured Doped CeO_2 with Potential for Solar-Cell Use. *Nat. Mater.* **2004**, *3*, 394-397.

[33] Deshpande, A. S.; Pinna, N.; Smarsly, B.; Antonietti, M.; Niederberger, M. Controlled Assembly of Preformed Ceria Nanocrystals into Highly Ordered 3D Nanostructures. *Small* **2005**, *1*, 313-316.

[34] Ba, J. H.; Polleux, J.; Antonietti, M.; Niederberger, M. Non-aqueous Synthesis of Tin Oxide Nanocrystals and Their Assembly into Ordered Porous Mesostructures. *Adv. Mater.* **2005**, *17*, 2509-2512.

[35] Brezesinski, B.; Wang, J.; Polleux, J.; Dunn, B.; Tolbert, S. H. Templated Nanocrystal-Based Porous TiO_2 Films for Next-Generation Electrochemical Capacitors. *J. Am. Chem. Soc.* **2009,** *131*, 1802-1809.

[36] Szeifert, J. M.; Feckl, J. M.; Fattakhova-Rohlfing, D.; Liu, Y.; Kalousek, V.; Rathousky, J.; Bein, T. Templated Nanocrystal-Based Porous TiO_2 Films for Next-Generation Electrochemical Capacitors. *J. Am. Chem. Soc.* **2010,** *132*, 12605-12611.

[37] Sun, S.; Murray, C. B. Synthesis of Monodisperse Cobalt Nanocrystals and Their Assembly Into Magnetic Superlattices. *J. Appl. Phys.* **1999**, *85*, 4325-4330.

[38] Boyer, J.-C.; Vetrone, F.; Cuccia, L. A.; Capobianco, J. A. Templated Nanocrystal-Based Porous TiO2 Films for Next-Generation Electrochemical Capacitors. *J. Am. Chem. Soc.* **2006**, *128*, 7444-7445.

[39] Shevchenko, E. V.; Talapin, D. V.; Rogach, A. L.; Kornowski, A.; Haase, M.; Weller, H. Colloidal Synthesis and Self-Assembly of $CoPt_3$ Nanocrystals. *J. Am. Chem. Soc.* **2002**, *124*, 11480-11485.

[40] Manna, L.; Milliron, D. J.; Meisel, A.; Scher, E. C.; Alivisatos, A. P. Controlled Growth of Tetrapod-Branched Inorganic Nanocrystals *Nat. Mater.* **2003**, *2*, 382-385.

[41] Hines, M. A.; Guyot-Sionnest, P. Synthesis and Characterization of Strongly Luminescing Zn-S Capped CdSe Nanocrystals. *J. Phys. Chem.* **1996**, *100*, 468-471.

[42] Peng, X.; Schlamp, M. C.; Kadavanich, A. V.; Alivisatos, A. P. Epitaxial Growth of Highly Luminescent CdSe/CdS Core/Shell Nanocrystals with Photostability and Electronic Accessibility. *J. Am. Chem. Soc.* **1997**, *119*, 7019-7029.

[43] Xia, Y.; Xiong, Y. J.; Lim, B.; Skrabalak, S. E. Shape-Controlled Synthesis of Metal Nanocrystals: Simple Chemistry Meets Complex Physics? *Angew. Chem., Int. Ed*. **2009**, *48*, 60-103.

[44] Yu, W. W.; Falkner, J. C.; Shih, B. S.; Colvin, V. L. Preparation and Characterization of Monodisperse PbSe Semiconductor Nanocrystals in a Noncoordinating Solvent. *Chem. Mater.* **2004**, *16*, 3318-3322.

[45] Murray, C. B.; Norris, D. J.; Bawendi, M. G. Synthesis and Characterization of Nearly Monodisperse CdE (E = Sulfur, Selenium, Tellurium) Semiconductor Nanocrystallites *J. Am. Chem. Soc.* **1993**, *115*, 8706-8715.

[46] Chen, O.; Chen, X.; Yang, Y.; Lynch, J.; Wu, H.; Zhuang, J.; Cao, Y. C. Synthesis of Metal–Selenide Nanocrystals Using Selenium Dioxide as the Selenium Precursor. *Angew. Chem., Int. Ed.* **2008**, *47*, 8638-8641.

[47] Sun, Y.; Xia, Y. Shape-Controlled Synthesis of Gold and Silver nanoparticles. *Science* **2002**, *298*, 2176-2179.

[48] Peng, X.; Manna, L.; Yang, W.; Wickham, J.; Scher, E.; Kadavanich, A.; Alivisatos, A. P. Shape Control of CdSe Nanocrystals. *Nature*, **2000**, *404*, 59-61.

[49] Gaponik, N.; Talapin, D. V.; Rogach, A. L.; Hoppe, K.; Shevchenko, E. V.; Kornowski, A.; Eychmuller, A.; Weller, H. Thiol-Capping of CdTe Nanocrystals: An Alternative to Organometallic Synthetic Routes. *J. Phys. Chem. B* **2002**, *106*, 7177-7185.

[50] Talapin, D. V.; Yu, H.; Shevchenko, E. V.; Lobo, A.; Murray, C. B. Synthesis of Colloidal PbSe/PbS Core−Shell Nanowires and PbS/Au Nanowire−Nanocrystal Heterostructures. *J Phys. Chem. C* **2007**, *111*, 14049-14054.

[51] Niederberger, M.; Bartl, M. H.; Stucky, G. D. Benzyl Alcohol and Titanium Tetrachloride – A Versatile reaction System for the Nonaqueous and Low-temperature Preparation of Crystalline and Luminescent Titania Nanoparticles. *Chem. Mater.* **2002**, *14*, 4364-4370

[52] Niederberger, M.; Garnweitner, G.; Krumeich, F.; Nesper, R.; Colfen, H.; Antonietti, M. Tailoring the Surface and Solubility Properties of Nanocrystalline Titania by a Nonaqueous In Situ Functionalization Process. *Chem. Mater.* **2004**, *16*, 1202-1208.

[53] Dong, A.; Ye, X.; Chen, J.; Kang, Y.; Gordon, T.; Kikkawa, J. M.; Murray, C. B. A Generalized Ligand-Exchange Strategy Enabling Sequential Surface Functionalization of Colloidal Nanocrystals. *J. Am. Chem. Soc*. **2011,** *133*, 998-1006.

[54] Nag, A.; Kovalenko, M. V.; Lee, J-S.; Liu, W.; Spokoyny, B.; Talapin, D. V. Metal-free Inorganic Ligands for Colloidal Nanocrystals: S^{2-}, HS^{-}, Se^{2-}, HSe^{-}, Te^{2-}, HTe^{-}, TeS_3^{2-}, OH^{-}, and NH^{2-} as Surface Ligands. *J. Am. Chem. Soc*. **2011,** *133*, 10612-10620.

[55] Rosen, E. L.; Buonsanti, R.; Llordes, A.; Sawvel, A. M.; Milliron, D. J.; Helms, B. A. Exceptionally Mild Reactive Stripping of Native Ligands from Nanocrystal Surfaces by Using Meerwein's Salt. *Angew. Chem. Int. Ed*. **2012,** *51*, 684-689.

[56] Llordes, A.; Hammack, A. T.; Buonsanti, R.; Tangirala, R.; Aloni, S.; Helms, B. A.; Milliron, D. J. Polyoxometalates and Colloidal Nanocrystals as Building Blocks for Metal Oxide Nanocomposite Films. *J. Mater. Chem.* **2011,** *21*, 11631-11638.

[57] Choi, S. I.; Nam, K. M.; Park, B. K.; Seo, W. S.; Park, J. T. Preparation and Optical Properties of Colloidal, Monodisperse, and Highly Crystalline ITO Nanoparticles. *Chem. Mater.* **2008**, *20*, 2609-2611.

[58] Giltsrap, R. A.; Capozzi, C. J.; Carson, C. G.; Gerhardt, R. A.; Summers, C. J. Synthesis of a Nonagglomerated Indium Tin Oxide Nanoparticle Dispersion. *Adv. Mater.* **2008**, *20*, 4163–4166.

[59] Yu, T.; Moon, J.; Park, J.; Park, Y. I.; Bin Na, H.; Kim, B. H.; Song, I. C.; Moon, W. K.; Hyeon, T. Various-Shaped Uniform Mn_3O_4 Nanocrystals Synthesized at Low Temperature in Air Atmosphere. *Chem. Mater.* **2009,** *21*, 2272-2279.

[60] Masala, O.; Seshadri, R. Magnetic Properties of Capped, Soluble MnFe2O4 Nanoparticles. *Chemical Physics Letters* **2005**, *402*, 160-164.

[61] Lu, Y.; Ganguli, R.; Drewien, C. A.; Anderson, M. T.; Brinker, C. J.; Gong, W.; Guo, Y.; Soyez, H.; Dunn, B.; Huang, M. H.; Zink, J. I. Continuous Formation of Supported Cubic and Hexagonal Mesoporous Films by Sol-Gel Dip-Coating. *Nature*, **1997**, *389*, 364-368.

[62] Garcia, B. C.; Kamperman, M.; Ulrich, R.; Jain, A.; Gruner, S. M.; Wiesner, U. Morphology Diagram of a Diblock Copolymer-Aluminosilicate Nanoparticle System *Chem. Mater.* **2009**, *21*, 5397-5405.

[63] Brezesinski, B.; Wang, J.; Tolbert, S. H.; Dunn, B. Ordered Mesoporous Alpha-MoO3 with Iso-Oriented Nanocrystalline Walls for Thin-Film Pseudocapacitors. *Nat. Mater.* **2010,** *9*, 146-151.

[64] Haetge, J.; Hartmann, P.; Brezesinski, K.; Janek, J.; Brezesinski, T. Ordered Large-Pore Mesoporous Li4Ti5O12 Spinel Thin Film Electrodes with Nanocrystalline Framework for High Rate Rechargeable Lithium Batteries: Relationships among Charge Storage, Electrical Conductivity, and Nanoscale Structure. *Chem. Mater.* **2011**, *23*, 4384-4393.

[65] Sallard, S.; Brezesinski, T.; Smarsly, B. M. Electrochromic Stability of WO3 Thin Films with Nanometer-Scale Periodicity and Varying Degrees of Crystallinity. *J. Phys. Chem. C* **2007**, *111*, 7200-7206.

[66] Quickel, T. E.; Le, V. H.; Brezensinski, T.; Tolbert, S. H. On the Correlation Between Nanoscale Structure and Magnetic Properties in Ordered Mesoporous Cobalt Ferrite (CoFe2O4) Thin Films. *Nano Lett.* **2010**, *10*, 2982-2988.

[67] Haetge, J.;Suchomski, C.; Brezesinski, T. Ordered Mesoporous MFe2O4 (M = Co, Cu, Mg, Ni, Zn) Thin Films with Nanocrystalline Walls, Uniform 16 nm Diameter Pores and High Thermal Stability: Template-Directed Synthesis and Characterization of Redox Active Trevorite. *Inorg. Chem.* **2010**, *49*, 11619-11626.

[68] Richman, E. K.; Kang, C. B.; Brezesinski, T.; Tolbert, S. H. Ordered Mesoporous Silicon through Magnesium Reduction of Polymer Templated Silica Thin Films. *Nano Lett.* **2008**, *8*, 3075-3079.

[69] Suchomski, C.; Reitz, C.; Brezesinski, K.; Tavares de Sousa, C.; Rohnke, M.; Iimura, K.; Esteves de Araujo, J. P.; Brezesinski, T. Structural, Optical, and Magnetic Properties of Highly Ordered Mesoporous MCr_2O_4 and $MCr_2–xFe_xO_4$ (M = Co, Zn) Spinel Thin Films with Uniform 15 nm Diameter Pores and Tunable Nanocrystalline Domain Sizes. *Chem. Mater.* **2012**, *24*, 155-165.

[70] Brezesinski, K.; Wang, J.; Haetge, J.; Reitz, C.; Steinmueller, S. O.; Tolbert, S. H.; Smarsly, B. M.; Dunn, B.; Brezesinski, T. Pseudocapacitive Contributions to Charge Storage in Highly Ordered Mesoporous Group V Transition Metal Oxides with Iso-Oriented Layered Nanocrystalline Domains. *J. Am. Chem. Soc.* **2010**, *132*, 6982-6990.

[71] Templin, M.; Franck, A.; Chesne, A. D.; Leist, H.; Zhang, Y.; Ulrich, R.; Schadler, V.; Wiesner, U. Organically Modified Aluminosilicate Mesostructures from Block Copolymer Phases. *Science* **1997**, *278*, 1795-1798.

[72] Kuemmel, M.; Smatt, J.-H.; Boissiere, C.; Nicole, L.; Sanchez, C.; Linden, M.; Grosso, D.; *J.* Hierarchical Inorganic Nanopatterning (INP) Through Direct Easy Block-Copolymer Templating. *Mater. Chem.*, **2009**, *19*, 3638-3642.

[73] Baroch, P.; Hieda, J.; Saito, N.; Takai, O. Atmospheric Plasma-Calcination of Mesoporous Tungsten Oxide Utilizing Plasma Dielectric Barrier Discharge. *Thin Solid Films* **2007**, *515*, 4905-4908.

[74] Maruo, T.; Tanaka, S.; Nishiyama, N.; Motoda, K.; Funayama, K.; Egashira, Y.; Ueyama, K. Low-Index Mesoporous Silica Films Modified With Trimethylethoxysilane *Colloids and Surfaces A* **2008**, *318*, 84-87.

[75] Besson, S.; Gacoin, T.; Jacquiod, C.; Ricolleau, C.; Babonneau, D.; Boilot, J.-P. Structural Study of 3D-Hexagonal Mesoporous Spin-coated Sol-Gel Films *J. Mater. Chem.* **2000**, *10*, 1331-1336.

[76] Brezesinski, T.; Groenewolt, M.; Antonietti, M.; Smarsly, B. Crystal-to-Crystal Phase Transition in Self-Assembled Mesoporous Iron Oxide Films. *Angew. Chem. Int. Ed.* **2006**, *45*, 781-784.

[77] Schleich, D. M.; Zhang, Y. Preparation of Some Metal Ferrite MFe2O4 Thin Films Through a Nonaqueous Sol Method *Mater. Res. Bull.* **1995**, *30*, 447-452.

[78] Jiang, X.; Xie, Y.; Lu, J.; He, W.; Zhu, L.; Qian, Y. Preparation and Phase Transformation of Nanocrystalline Copper Sulfides (Cu_9S_8, Cu_7S_4 and CuS). *J. Mater. Chem*., **2000**, *10*, 2193-2196.

[79] Chernyshova, I. V.; Hochella, M. F.; Madden, A. S. Size-dependent Structural Transformations of Hematite Nanoparticles. 1. Phase transition. *Phys. Chem. Chem. Phys*. **2007**, *9*, 1736-1750.

[80] Baklonov, M. R.; Mogilnikov, K. P.; Polovinkin, V. G.; Dultsev, F. N. Determination of Pore Size Distribution in Thin Films by Ellipsometric Porosimetry. *J. of Vac. Sci. & Tech. B* **2000**, *18*, 1385-1391.

[81] Gregg, S. J.; Sing, K. S. W.; Adsorption, Surface Area, and Porosity. 2nd ed. (Academic, London, 1982).

[82] Buonsanti, R.; Pick, T. E.; Krins, N.; Richardson, T. J.; Helms, B. A.; Milliron, D. J.; submitted.

[83] Hillmyer, M. A.; Bates, F. S. Synthesis and Characterization of Model Polyalkane–Poly(ethylene oxide) Block Copolymers. *Macromolecules* **1996**, *29*, 6994-7002.

[84] Allgaier, J.; Poppe, A.; Willner, L.; Richter, D. Synthesis and Characterization of Poly[1,4-Isoprene-b-(ethylene oxide)] and Poly[ethylene-co-propylene-b-(ethylene oxide)] Block Copolymers. *Macromolecules* **1997**, *30*, 1582-1586.

Chapter 5

Nanostructured Pseudocapacitors Based on Atomic Layer Deposition of V_2O_5 onto Conductive Nanocrystal-Based Mesoporous ITO Scaffolds

5.1 Introduction

Electrochemical energy storage devices known as pseudocapacitors have attracted much attention because they have the ability to attain high energy densities while maintaining high power densities.[1] Pseudocapacitors store charge through fast and reversible faradaic processes that involve surface or near-surface redox reactions. These charge storage mechanisms are different than those in traditional batteries because they are not limited by the diffusion of ions into the bulk material. Therefore, pseudocapacitors can offer several benefits when compared to batteries including fast charge/discharging within seconds, good charge/discharge cycling stability, and the ability to deliver >10x more power.[2] An ideal pseudocapacitor electrode architecture should comprise a redox-active material (e.g. a metal oxide) that has a nanodimensional structure to accommodate shorter ion diffusion lengths. In addition, the material should have a high surface area in order to maximize electrolyte accessible redox-active sites, and, have an open interconnected porosity to facilitate solvent diffusion to all of these redox-active sites. Finally, electrical conductivity should be integrated and wired into the redox-active component in order to simultaneously achieve both higher energy and power densities in one structure.

The improvements to electrochemical energy storage resulting from building electrical conductivity into electrode materials are well established in the literature. Carbon-based materials such as carbon nanotubes (CNT) and graphene have been shown to act as good

conductive platforms for the construction of composite electrodes. For example, CNT-based composites of manganese oxide (MnO_2),[3] titanium oxide (TiO_2),[4] tin oxide (SnO_2),[4] lithium manganese oxide ($LiMn_2O_4$),[5] and V_2O_5[6],[7],[8],[9],[10] have been reported. Graphene-based composites of $LiMn_2O_4$,5 iron oxide (Fe_3O_4),[11] SnO_2,[12] $Ni(OH)_2$,[13] and MnO_2[14] have also been produced as well as other carbon scaffolds with interesting architectures.[15],[16] In addition to carbon-based conductors, metals have also been integrated into composite electrodes with unique architectures including an interpenetrated nickel inverse opal,[17] nanoporous gold,[18] nickel porous foams,[19],[20] copper pillar arrays,[21] and stainless steel meshes.[22] In the examples above, the conductive component provided a network for good electrical transport throughout the active material which resulted in improvements to the electrochemical performance.

Electrical conductivity is important for enabling the charge transfer which leads to faradaic reactions in pseudocapacitor materials, but that in itself is not enough to convert a standard intercalation based battery material into a pseudocapacitive material. In addition, a high interfacial area in contact with the electrolyte is also necessary. For example, we reported significant enhancements to the capacitive charge storage behavior in nanocrystal-based mesoporous TiO_2 pseudocapacitors templated using poly(ethylene oxide-*block*-hydrocarbon) [PEO-XXX] type polymers.[23] In that work, the porous titania architectures demonstrated high levels of pseudocapacitive charge storage that were accompanied by rapid charging/discharging rates.[23] The improved performance resulted from the unique architecture, which exhibited an open interconnected porosity that facilitated rapid solvent diffusion throughout the material, as well as a high density of redox-active surface sites arising from the nanocrystals within the pore walls. Bein and coworkers have also reported the preparation of mesoporous films from TiO_2 nanocrystalline particles that demonstrated high Li insertion capacities and fast charging rates

resulting from the high surface to bulk ratio of the nanocrystals and the easily accessible mesoporous structures.[24] The literature includes a variety of other examples of this type of polymer templated nanocrystal-based co-assembly to prepare porous architectures.[25]–[28]

More recently, we have developed a general route for assembling pre-formed ligand-stripped[29] nanocrystals into hierarchical mesoporous architectures,[30] and it is those chemistries that are used in this work. Model redox-active systems included Mn_3O_4, $(Mn,Fe)_2O_3$, and tin-doped indium oxide (ITO), and similar to our TiO_2 nanocrystal-based materials,[23] we found that templated Mn_3O_4 nanocrystal-based films exhibited enhanced charge storage behavior compared to untemplated nanocrystals, again demonstrating the efficacy of a nanocrystal based nanoporous electrode architecture.[30] Moreover, we demonstrated high synthetic tunability where the mesoporosity could be tuned by varying the polymer template, and the microporosity could be tuned by varying the size of the nanocrystal.[30] We also showed that the method could be applied to non-oxide systems.[31] Other recent studies showed that this method also works with polymers containing non-PEO polar blocks. [32]

While our polymer templated nanocrystal-based mesoporous materials provide an attractive and effective electrode architecture, they will ultimately be limited by electrical conductivity when scaled up to prepare thick electrodes. Therefore, in order to build electrodes with more ideal architectures, we need to integrate a conductor into our materials while still retaining the high surface area and open interconnected porosity. Here, we use solution-phase methods to construct porous conductive scaffolds by templating ITO nanocrystals into mesoporous architectures and subsequently coating the ITO with V_2O_5 via atomic layer deposition (ALD) to produce pseudocapacitor electrode composites. The Rubloff group recently developed and optimized a new ALD V_2O_5 process that resulted in highly conformal and

crystalline V_2O_5 films that demonstrated high performance electrochemical energy storage.[10],[33], [34] We use this process to coat porous ITO with two different thicknesses: 2 nm and 7 nm V_2O_5 layers. We also study crystallinity effects in the V_2O_5 layers by heating to various temperatures and examine the pseudocapacitive response.

In addition to our examination of model pseudocapacitor architectures, this work allows us to explore some fundamental questions related to pseduocapacative charge storage. For example, by using two different vanadia film thicknesses, this unique system allows us to explore the kinetics of Li^+ motion into vanadia layers of different thicknesses. Specifically, we try to answer the question – how thick can a vanadia film be before the charge storage has a significant non-capacitive contribution? The answer should have significant ramifications in the rational design of nanoscale pseudocapacitors.

5.2 Results and Discussion

5.2.1 Synthesis of ITO-V_2O_5 Composites.

We previously reported the synthesis of mesoporous ITO nanocrystal-based films.[30] Here, we use poly(ethylene-*alt*-propylene)-*block*-poly(ethylene oxide), (PEP-*b*-PEO) as the block copolymer template. ITO nanocrystals capped with amine functional ligands were synthesized according to literature procedures.[35]–[37] Next, the as-synthesized nanocrystals were stripped of their ligands using an $NOBF_4$ treatment to produce bare nanocrystals that were charge-stabilized.[**Error! Bookmark not defined.**] Figure 5.1b shows a TEM image of ligand-stripped ITO nanocrystals with an

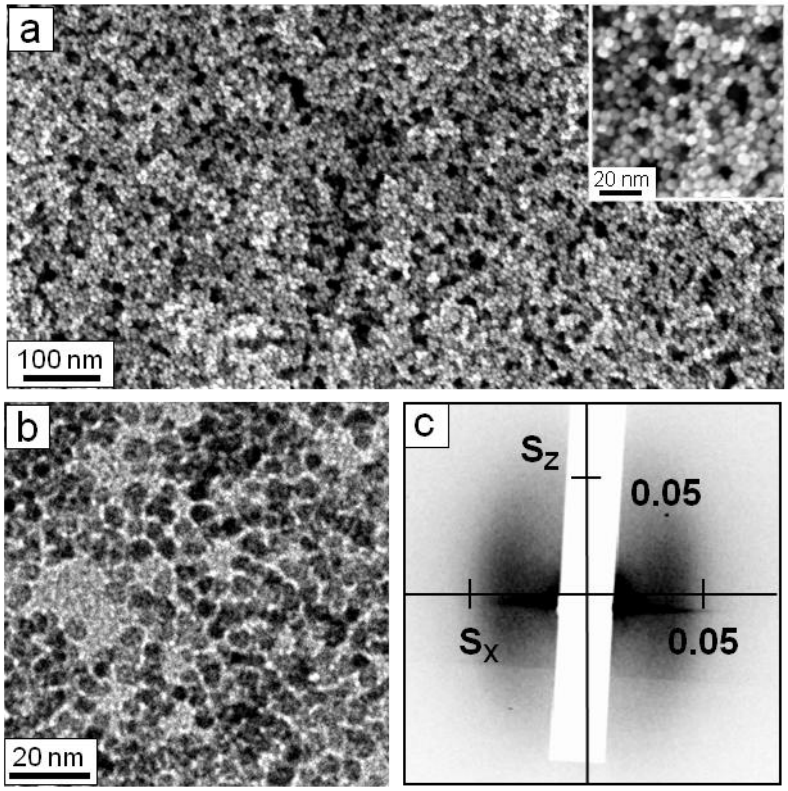

Figure 5.1. (a) Low-magnification SEM image of a templated ITO nanocrystal-based mesoporous film. Inset: higher-magnification image showing pore walls comprising individual ITO nanocrystals. (b) TEM image of ligand-stripped ITO nanocrystals with an average diameter of 4.6 ± 0.4 nm. (c) 2D-SAXS pattern obtained on a ITO nanocrystal-based porous film, collected at an angle of incidence β = 1.25°. The pattern shows strong in-plane scattering, indicative of a well-defined pore size, but no long range periodicity of the pores. Scattering vector *S* components are given in 1/nm.

average diameter of 4.6 ± 0.4 nm demonstrating they are uniform in shape and size, and free of agglomeration. Ligand-stripped ITO nanocrystals, dispersed in ethanol with ~10% dimethylformamide (DMF) (v/v), were mixed with PEP-*b*-PEO, dissolved in pure ethanol, to prepare the coating solution. Thin-films were then either dip-coated or spin-coated onto clean polar substrates through an evaporation-induced self-assembly process.[38] In solution, the polymer self-assembles to form micelles and, upon evaporation of the solvent, the ITO nanocrystals associate with the polar PEO block to yield a mesostructured organic/inorganic composite. The polymer template was then thermally decomposed by heating the films to 450 °C, resulting in ITO nanocrystal-based mesoporous architectures.

Figure 5.1a shows a low-magnification SEM image of a mesoporous ITO film exhibiting a bimodal porosity with a combination of mesopores, created by the polymer template, and micropores which arise from the spaces between the nanocrystals that make up the pore walls. The mesopores, with an average pore size of 15 ± 3 nm, are locally disordered; however, they do retain a macroscopically homogeneous porosity. The films are crack-free and maintain open porosity at the surface. A closer look at a high-magnification image (inset of Figure 5.1a) shows individual ITO nanocrystals that comprise the pore walls, which are approximately 1 – 3 nanocrystals thick. Because the nanocrystals do not completely fuse to form a dense wall, the voids between them gives rise to micropores that significantly increase the surface area of the material.

To further characterize the nanoscale architecture we performed two-dimensional small-angle X-ray scattering (2D-SAXS) and ellipsometric porosimetry measurements. Figure 5.1c shows the 2D-SAXS pattern obtained for mesoporous ITO films, collected at an angle of incidence β = 1.25°. The pattern shows a diffuse ellipsoidal ring with strong in-plane scattering,

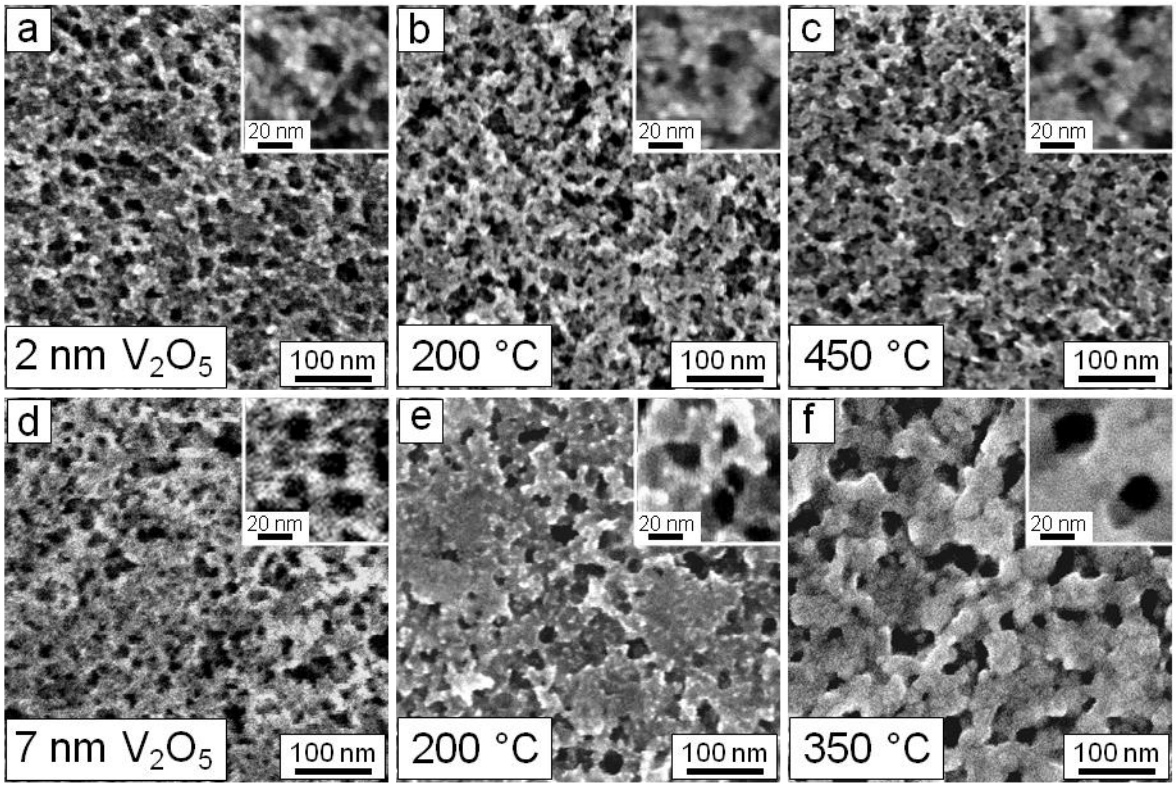

Figure 5.2. (a–c) Low-magnification SEM images of mesoporous ITO films coated with a 2 nm layer of V_2O_5 as-deposited (a) (inset: higher-magnification image showing individually coated nanocrystals); heated to 200 °C (b) (inset: higher-magnification image showing grain growth of the V_2O_5 around the nanocrystals); and, heated to 450 °C (c) (inset: higher-magnification image showing grain growth of the V_2O_5 around the nanocrystals). (d–f) Low-magnification SEM images of mesoporous ITO films coated with a 7 nm layer of V_2O_5 as-deposited (d) (inset: higher-magnification image showing spaces in between nanocrystals are filled in with V_2O_5); heated to 200 °C (e) (inset: higher-magnification image showing grain growth of V_2O_5 leads to partially fused pores); and, heated to 350 °C (f) (inset: higher-magnification image showing grain growth of the V_2O_5 leads to significant loss of mesostructure).

indicative of a homogenous but non-periodic pore structure with a characteristic pore + wall distance of 32 nm. The porosity of the ITO films was analyzed by ellipsometric porosimetry using toluene as the adsorbate.[39] Figure 5.4a shows an adsorption-desorption isotherm for a mesoporous ITO film that exhibits typical type IV behavior.[40] The hysteresis present at higher relative pressures is indicative of a mesostructured material an open interconnected porosity. The adsorption and desorption curves describe the cage and neck sizes of the mesopores. A Kelvin model fit to the isotherm produces pore size distributions for the cages centered at 25 nm, and for the necks at 11 nm, as shown in Figure 5.4b. The data confirm that the template nanocrystal based ITO films exhibit bimodal porosity that leads to high surface area combined with interconnected, open porosity. The isotherm in Figure 5.4a shows a 53% toluene-accessible pore volume. It should be noted that the average mesopore sizes found by porosimetry (Figure 5.4 a – b) agree with lengthscales determined by 2D-SAXS (Figure 5.1c) and SEM (Figure 5.2 b – c). In addition, the pore size can be varied by changing the polymer to nanocrystal ratio, allowing many different pores sizes can be produced. In this work, ITO frameworks with pore sizes varying from about 15 nm to about 25 nm were used.

The ITO films discussed below function as high surface area, porous, conductive scaffolds. Once prepared, we coated the ITO scaffolds with thin film layers of V_2O_5 via an ALD process.[33] ALD is a low temperature thin film growth technique where the surface to be coated is sequentially exposed to various precursors, leading to predictable monolayer growth with superb uniformity even over demanding topography, such as high-aspect ratio nanostructures.[41],[42] In this process, we explored two ALD processes using different oxidants-water and ozone. We also studied two different thicknesses, ~2 nm and ~7 nm V_2O_5 layers, where the thickness is controlled by the number of ALD cycles (see experimental details).

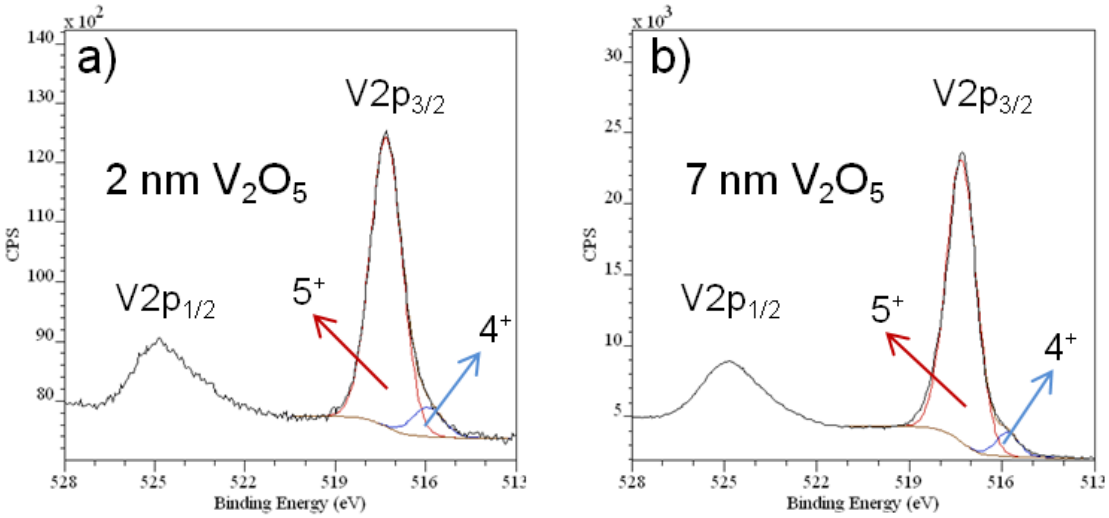

Figure 5.3. XPS spectra for porous ITO films coated with a 2 nm (a) and 7 nm (b) layer of V_2O_5. The survey scans show the V 2p core regions, with peaks for both $2p_{3/2}$ and $2p_{1/2}$ core levels. The red arrows point to the V^{5+} peak and the blue arrows points to the V^{4+} after deconvolution of the $V2p_{3/2}$ peaks.

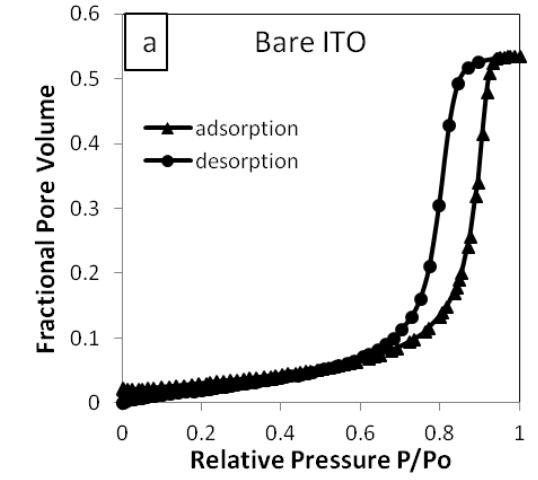
a
Bare ITO
adsorption
desorption
Fractional Pore Volume
Relative Pressure P/Po
0.6
0.5
0.4
0.3
0.2
0.1
0
0
0.2
0.4
0.6
0.8
1

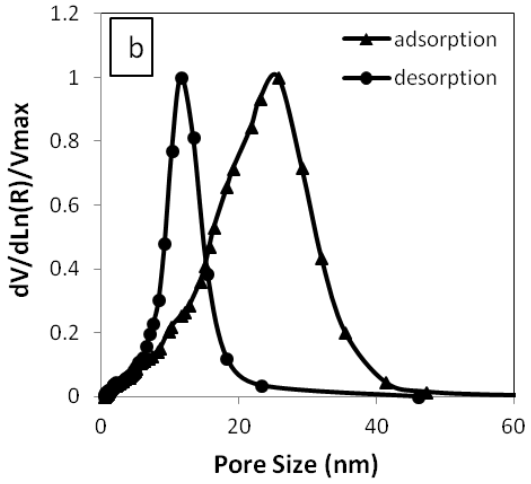
b
adsorption
desorption
dV/dLn(R)/Vmax
Pore Size (nm)
1.2
1
0.8
0.6
0.4
0.2
0
0
20
40
60

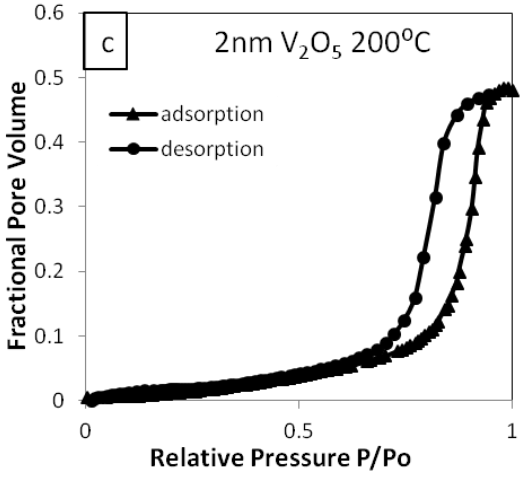
c
2nm V2O5 200°C
adsorption
desorption
Fractional Pore Volume
Relative Pressure P/Po
0.6
0.5
0.4
0.3
0.2
0.1
0
0
0.5
1

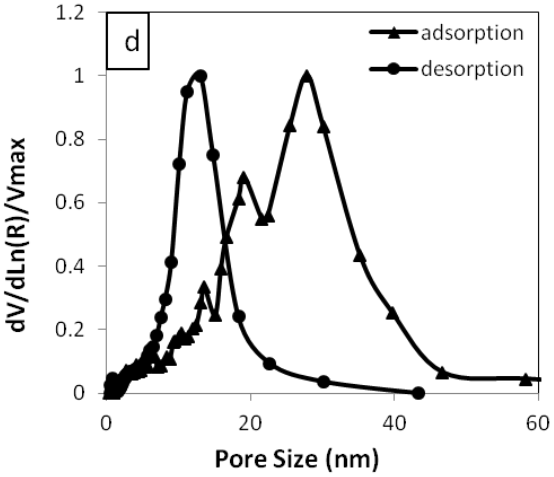
d
adsorption
desorption
dV/dLn(R)/Vmax
Pore Size (nm)
1.2
1
0.8
0.6
0.4
0.2
0
0
20
40
60

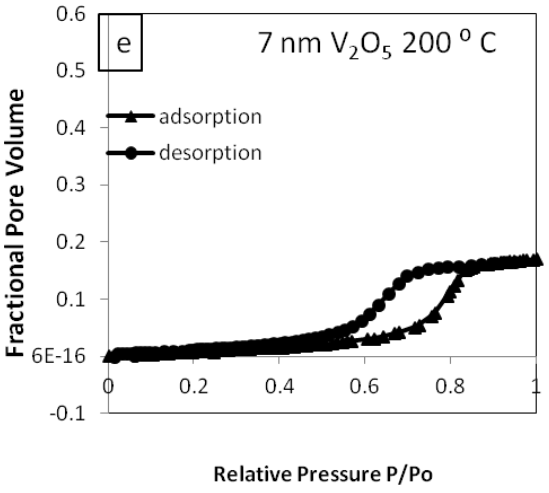
e
7 nm V2O5 200 ° C
adsorption
desorption
Fractional Pore Volume
Relative Pressure P/Po
0.6
0.5
0.4
0.3
0.2
0.1
6E-16
-0.1
0
0.2
0.4
0.6
0.8
1

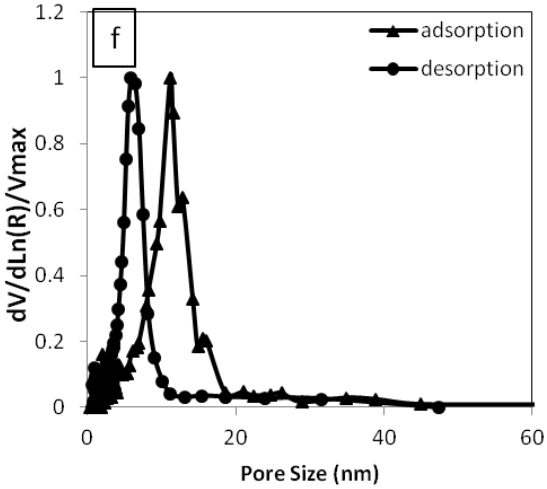
f
adsorption
desorption
dV/dLn(R)/Vmax
Pore Size (nm)
1.2
1
0.8
0.6
0.4
0.2
0
0
20
40
60

Figure 5.4. Toluene adsorption-desorption isotherms showing characteristic mesoporous behavior for a mesoporous ITO nanocrystal-based film (a), mesoporous ITO film coated with a 2 nm layer of V_2O_5 heated to 200 °C (c), mesoporous ITO film coated with a 7 nm layer of V_2O_5 heated to 200 °C (e). Pore size distribution data obtained from the 1isotherms for a mesoporous ITO nanocrystal-based film (b), mesoporous ITO film coated with a 2 nm layer of V_2O_5 heated to 200 °C (d), mesoporous ITO film coated with a 7 nm layer of V_2O_5 heated to 200 °C (f).

The composites were then annealed using rapid thermal annealing (RTA) in air at various temperatures allowing us to study the effects of crystallinity in the V_2O_5 layers. X-ray photoelectron spectroscopy (XPS) measurements (Figure 5.3) confirmed that heated samples contained pre-dominantly penta-valent vanadium, with 91% of vanadium atoms in the 5+ valence state and 9% in the 4+ valence state for 2 nm layers, and 96% in the 5+ valence state and 4% in the 4+ valence state for 7 nm layers. The observed binding energies for V^{5+} and V^{4+} were also found to be in agreement with literature values,[43] and the trends with film thickness indicate that the small amount of the V^{4+} was probably at the surface of the thin ALD films.

5.2.2 Structure and Electrochemical Properties of 2 nm V_2O_5 Layers.

Figure 5.2a – c shows top-view SEM images of smaller pore ITO films that were coated with a 2 nm layer of V_2O_5 (ozone-based, 100 ALD cycles) as-deposited (Figure 5.2a), heated to 200 °C (Figure 5.2b), and heated to 450 °C (Figure 5.2c). All three composites feature open porosity with visible mesopores with average diameters of 18 ± 3 nm (Figure 5.2a), 16 ± 3 nm (Figure 5.2b), and 15 ± 3 nm (Figure 5.2c). These values are all basically equivalent, given the statistical error, and are in agreement with the average diameter of 15 ± 3 nm determined for uncoated mesoporous ITO (Figure 5.1a). Importantly, in the higher-magnification images (insets) of Figure 5.2a – c, the presence of individually coated nanocrystals is visible, demonstrating that this process produces conformal vanadia layers around the ITO scaffold. Closer examination indicates that there is some grain growth of the V_2O_5 around the nanocrystals in the layers heated to 200 °C, while the layers heated 450 °C show clear grain growth. These results illustrate one of the challenges of this synthetic method, which is that V_2O_5 crystallization and coarsening are coupled processes and one cannot induce one without the other. As a result, we expect samples

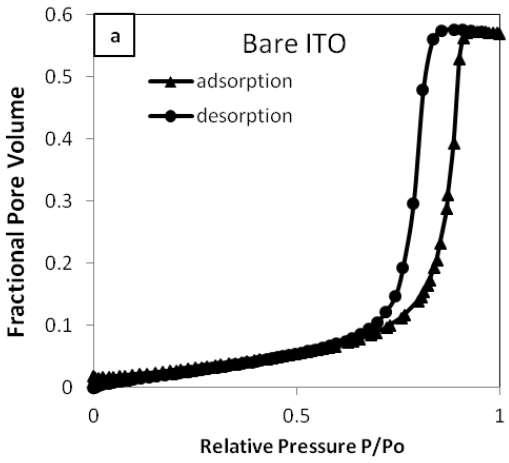
a
Bare ITO
adsorption
desorption
Fractional Pore Volume
Relative Pressure P/Po
0
0.1
0.2
0.3
0.4
0.5
0.6
0.5
1

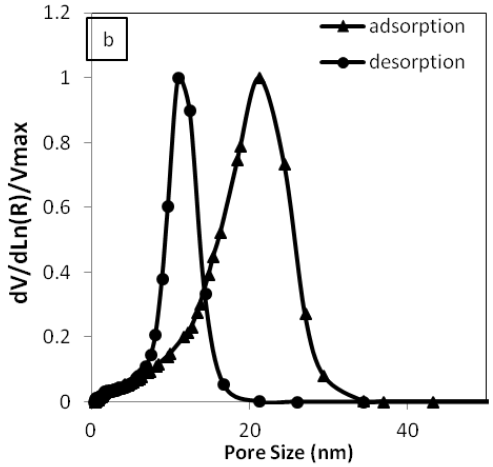
b
adsorption
desorption
dV/dLn(R)/Vmax
Pore Size (nm)
0
0.2
0.4
0.6
0.8
1
1.2
20
40

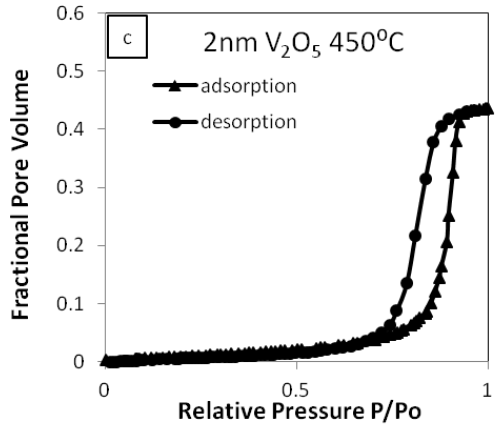
c
2nm V2O5 450°C
adsorption
desorption
Fractional Pore Volume
Relative Pressure P/Po
0
0.1
0.2
0.3
0.4
0.5
0.6
0.5
1

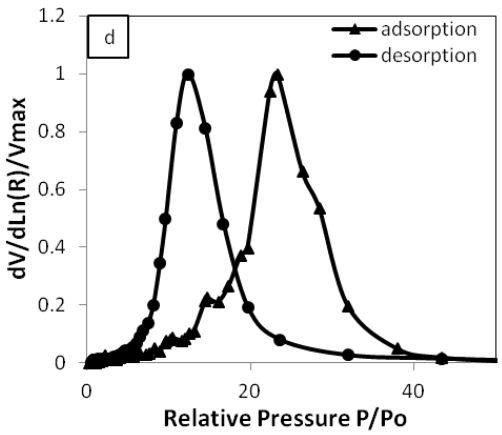
d
adsorption
desorption
dV/dLn(R)/Vmax
Relative Pressure P/Po
0
0.2
0.4
0.6
0.8
1
1.2
20
40

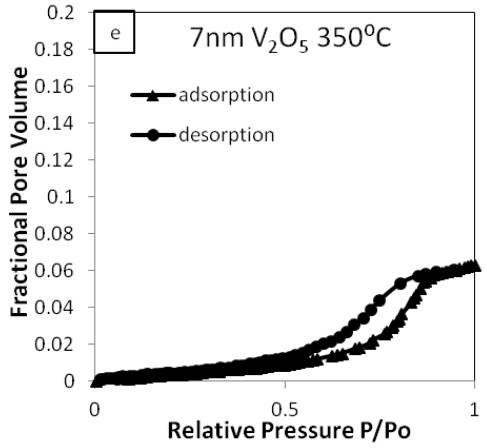
e
7nm V2O5 350°C
adsorption
desorption
Fractional Pore Volume
Relative Pressure P/Po
0
0.02
0.04
0.06
0.08
0.1
0.12
0.14
0.16
0.18
0.2
0.5
1

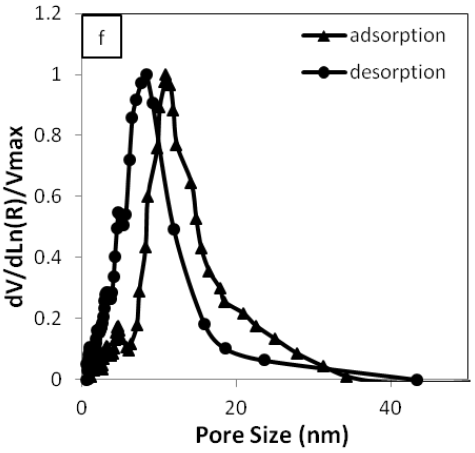
f
adsorption
desorption
dV/dLn(R)/Vmax
Pore Size (nm)
0
0.2
0.4
0.6
0.8
1
1.2
20
40

Figure 5.5. Toluene adsorption-desorption isotherms showing characteristic mesoporous behavior for a mesoporous ITO nanocrystal film (a), mesoporous ITO film coated with a 2nm layer of V_2O_5 heated to 450 °C (c), and mesoporous ITO film coated with 7nm layer of V_2O_5 heated to 350 °C (e). Pore size distribution data obtained from the isotherms for a mesoporous ITO nanocrystal film (b), mesoporous ITO film coated with a 2nm layer of V_2O_5 heated to 450 °C (d), and mesoporous ITO film coated with 7nm layer of V_2O_5 heated to 350 °C (f).

crystallized at higher temperatures to show smaller mesopore pore size and some filling of the micropores. We used ellipsometric porosimetry to analyze the porosity of the composites after coating, focusing first on a large pore ITO with a 2 nm thick V_2O_5 coating. For this sample, the uncoated porous ITO film showed a pore size distribution for the cages centered at 25 nm, and for the necks at 11 nm, (Figure 5.4b). The total pore volume is 53%. Adsorption-desorption isotherms for vanadia coated films heated to 200 °C (Figure 5.4c) and 450 °C (Figure 5.5c) show typical type IV behavior with hysteresis at higher relative pressures suggesting the composites are mesoporous with open interconnected porosity. The total pore volume for the sample heated to 200 ºC is 48% and is 43% for the sample heated to 450 ºC. A Kelvin model fit to the isotherms produces pore size distributions centered around 26 nm (cage) and 13 nm (neck) for films heated to 200 °C (Figure 5.4b), and 23 nm (cage) and 12 nm (neck) for films heated to 450 °C (Figure 5.5). Mesopore size is thus similar to the bare ITO film for both samples suggesting that 2nm of V_2O_5 does not significantly perturb the pore structure in either film. Table 5.1 summarizes porosimetry data for thin films heated to 200, 350 and 450 ºC. For all thin films, the toluene-accessible pore volume is lower than the pore volume observed for the parent, uncoated ITO.

Cyclic voltammetry (CV) was performed to examine the charge storage behavior of the 2nm V_2O_5 layers. The Li^+ insertion process can be expressed by $V_2O_5 + xLi^+ + xe^- \leftrightarrow Li_xV_2O_5$, where x represents the mole fraction of inserted lithium ions.[44] Figure 5.6a compares the charge storage dependence of 2 nm V_2O_5 heated to 200, 350 and 450 °C at sweep rates in the range between 2 mV/s to 100 mV/s. In all curves, the capacity increases with decreasing sweep rate, indicating that full storage has not been reached at the fastest rates. The V_2O_5 layer heated to

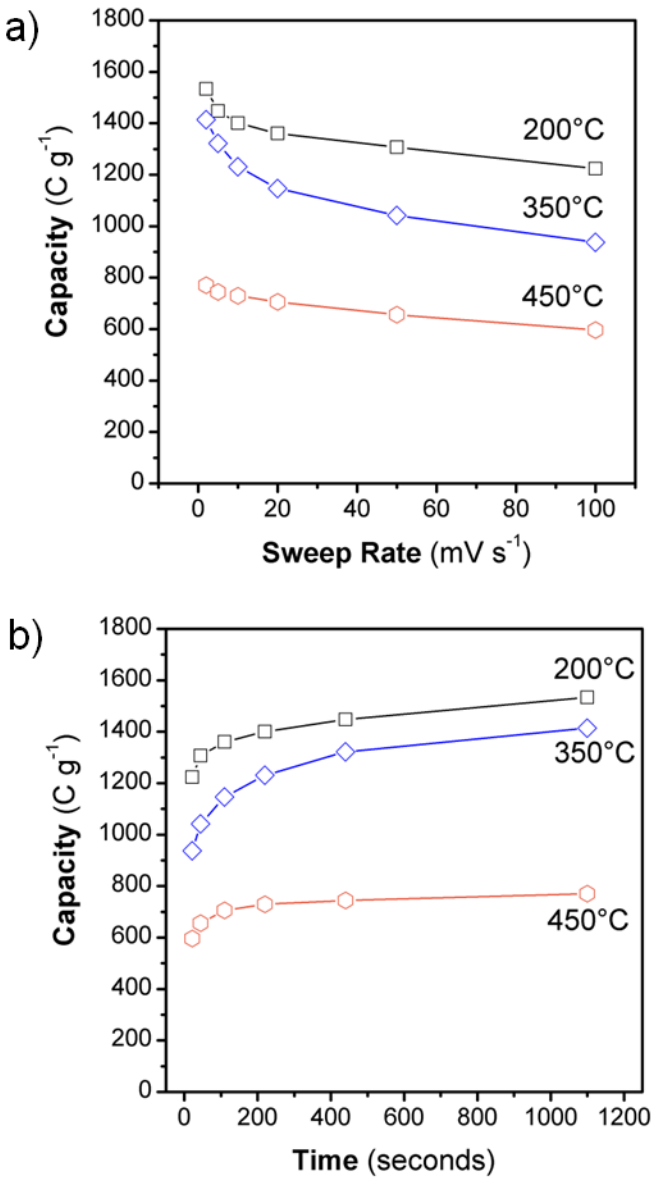

Figure 5.6. (a) Charge storage dependence on sweep rate for mesoporous ITO films coated with a 2 nm layer of V_2O_5 heated to 200, 350 and 450 °C. (b) Comparison of charging rates calculated from cyclic voltammetric data at various sweep rates for mesoporous ITO films coated with a 2 nm layer of V_2O_5 heated to 200, 350 and 450 °C.

200 °C stores almost twice as much charge as the 2 nm layer heated to 450 °C. Figure 5.6b shows the charge storage dependence of 2 nm V_2O_5 heated to 200, 350 and 450 °C plotted as capacity versus charging time, as calculated from the various sweep rates in Figure 5.6a using a 2.2 V potential window. In this type of plot, the slow sweep rate behavior is more apparent and the region of mostly constant capacity after 440 sec indicates that the material is fully charged at this timescale. After a charging time of 200 s, the total charge stored for 200 °C treated samples is 1400 C/g, almost twice the amount of charge stored in samples heated to 450 °C. The trend is not linear with temperature, however, as samples heated to 350 °C show a capacity of 1200 C/g. While the majority of charge is stored in only 200 s, there is a measureable increase in capacity going to longer times, indicating that not all redox sites are kinetically accessible.

In Figure 5.6, the differences in the gravimetrically normalized capacity observed between films heated to 200 and 350 °C can be attributed to the loss of porosity, as shown in Table 1. There is likely a small amount of grain growth that clogs a fraction of the smaller pores and leads to a lower total pore volume that can be accessible to the electrolyte. The difference in the capacity observed between films heated to 200 and 450 °C is likely explained by the atomic structure and bonding of the V_2O_5 layer. At 200 °C, the V_2O_5 should have a structure related to the orthorhombic phase, which is known to show facile Li^+ intercalation.[45] The material should also be less ordered, which can also increase redox sites.[45] When V_2O_5 is heated to 450 °C, a phase transition to the monoclinic crystalline structure occurs in bulk samples, leading to a reduction in Li^+ intercalation sites.[46] While redox pseudocapacitance is generally assumed to be a surface phenomenon, this data suggest that near-surface intercalation sites also contribute to redox pseudocapacitance and the lack of those near surface sites can cause a dramatic decrease in capacity.

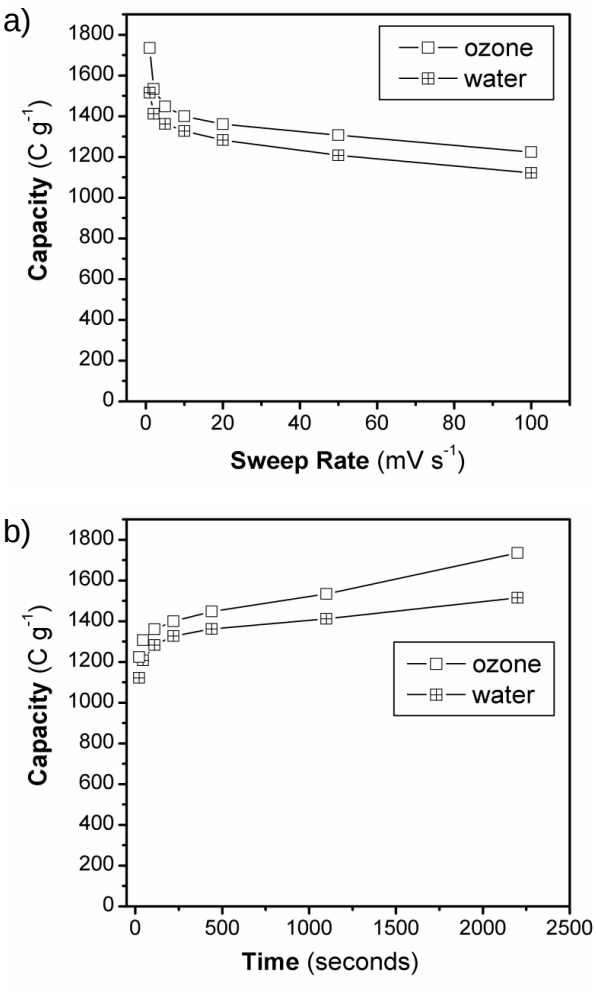

Figure 5.7. (a) Charge storage dependence on sweep rate for porous ITO films coated with a 2 nm of V_2O_5 via ALD using water and ozone as the oxidant, both were heated to 200 °C. (b) Comparison of capacity versus charging times for porous ITO films coated with a 2 nm of V_2O_5 via ALD using water and ozone as the oxidant, both were heated to 200 °C.

We also investigated the effects of using different oxidants during the ALD process by comparing both water- and ozone-based 2 nm V_2O_5 coatings. Figure 5.7a compares the charge storage behavior in 2 nm V_2O_5 coated ITO synthesized with water and ozone and heated to 200 °C, cycled at sweep rates ranging from 1 mV/s to 100 mV/s. For both water- and ozone-based 2 nm V_2O_5 the capacity increases with decreasing sweep rate. Figure 5.7b shows the charge storage dependence plotted as capacity versus charging time. The trend we observe is that while the V_2O_5 films produced by both methods are similar, that ozone-based materials exhibit somewhat higher charge storage behavior than water-based V_2O_5. This result is consistent with our recent study of ozone-based and water-based V2O5 in the application of Li-ion battery cathodes[47]

5.2.3 Structure and Electrochemical Properties of 7 nm V_2O_5 Layers.

We also investigated the effects of a thicker (7nm) V_2O_5 layer. Figure 5.2d – f shows top-view SEM images of porous ITO films that were coated with a 7 nm layer of V_2O_5 (ozone-based, 250 ALD cycles) as-deposited (Figure 5.2d), heated to 200 °C (Figure 5.2e), and heated to 350 °C (Figure 5.2f). Figure 5.2d shows that the thicker V_2O_5 fills most of the micropores but leaves most of the mesopores open. When the V_2O_5 layer is heated to 200 °C, as shown in Figure 5.2e, individual nanocrystals can no longer been seen, indicating that all of the micropores are filled, and V_2O_5 grain growth appears to block some of the mesopores as well. In Figure 5.2f one sees that when the V_2O_5 is heated to 350 °C, significant grain growth of the V_2O_5 leads to significant loss of mesostructure and many of the pores are clogged. The 7 nm V_2O_5 layers thus appear to be too thick to maintain the ideal porosity of these materials and so capacity loss due to pore blockage is expected in these materials. Despite this fact, kinetic studies on samples with thicker vanadia films should still provide insight about the rate of lithium insertion

	Percent porosity	Cage Size (nm)	Neck Size (nm)
Bare ITO	53%	25	11
2 nm V_2O_5 200 °C	48%	26	13
Bare ITO	60%	22	13
2nm V_2O_5 350 °C	45%	23	12
Bare ITO	52%	25	11
2nm V_2O_5 450 °C	43%	23	12
Bare ITO	57%	22	11
7nm V_2O_5 200 °C	17%	12	6
Bare ITO	56%	22	11
7nm V_2O_5 350 °C	6%	12	7

Table 5.1. Ellipsometric porosimetry data summarizing percent porosity, pore size, and neck size for thin 2nm V_2O_5 films heated to 200 ^{0}C, 350 ^{0}C and 400 ^{0}C and for thick V_2O_5 films heated to 200 ^{0}C and 350 ^{0}C compared to their respective bare ITO film.

into the thick layers. We also note that because so much grain growth was observed by 350 °C, we did not attempt to anneal the thick film samples to 450 °C to examine the effects of the phase transition from orthorhombic to monoclinic; we felt that it would not be possible to separate the effects of the phase transition from the effects of grain growth.

Ellipsometric porosimetry measurements were also performed on the 7 nm V_2O_5 composites by using toluene as the adsorbate. Adsorption-desorption isotherms for films heated to 200 °C (Figure 5.4e) and 350 °C (Figure 5.5e) show typical type IV behavior with a hysteresis at higher relative pressures indicating the films are mesoporous. A Kelvin model fit to the isotherms produces pore size distributions centered around 12 nm (cage) and 6 nm (neck) for films heated to 200 °C (Figure 5.4f), and 12 nm (cage) 7 nm (neck) for films heated to 350 °C (Figure 5.5f). The overall decrease in mesopore size is consistent with a thick layer of V_2O_5 coated ITO. The isotherms in Figure 5.4e and Figure 5.5e, also summarized in table 5.1, show ~17% and ~6% toluene-accessible pore volume, respectively, which is lower than the pore volume calculated for uncoated ITO (56%, Figure 5.5a) and 2 nm V_2O_5 coated ITO (48%, Figure 5.4c), also consistent with the fact that the ITO has been coated with a thicker layer of V_2O_5.

The charge storage behavior of the 7 nm V_2O_5 layers was also studied by CV. Figure 5.8a compares the charge storage dependence of 7 nm V_2O_5 heated to various temperatures (200, 250, 300, and 350 °C) at sweep rates ranging from 1 – 100 mV/s. As with the thinner films, for all temperatures, the gravimetrically normalized capacity increases with decreasing sweep rate, suggesting the V_2O_5 layer is not fully charged because of slow diffusion of Li+ ions into the structure, even at the slowest sweep rates used here. At all sweep rates, the films heated to 200

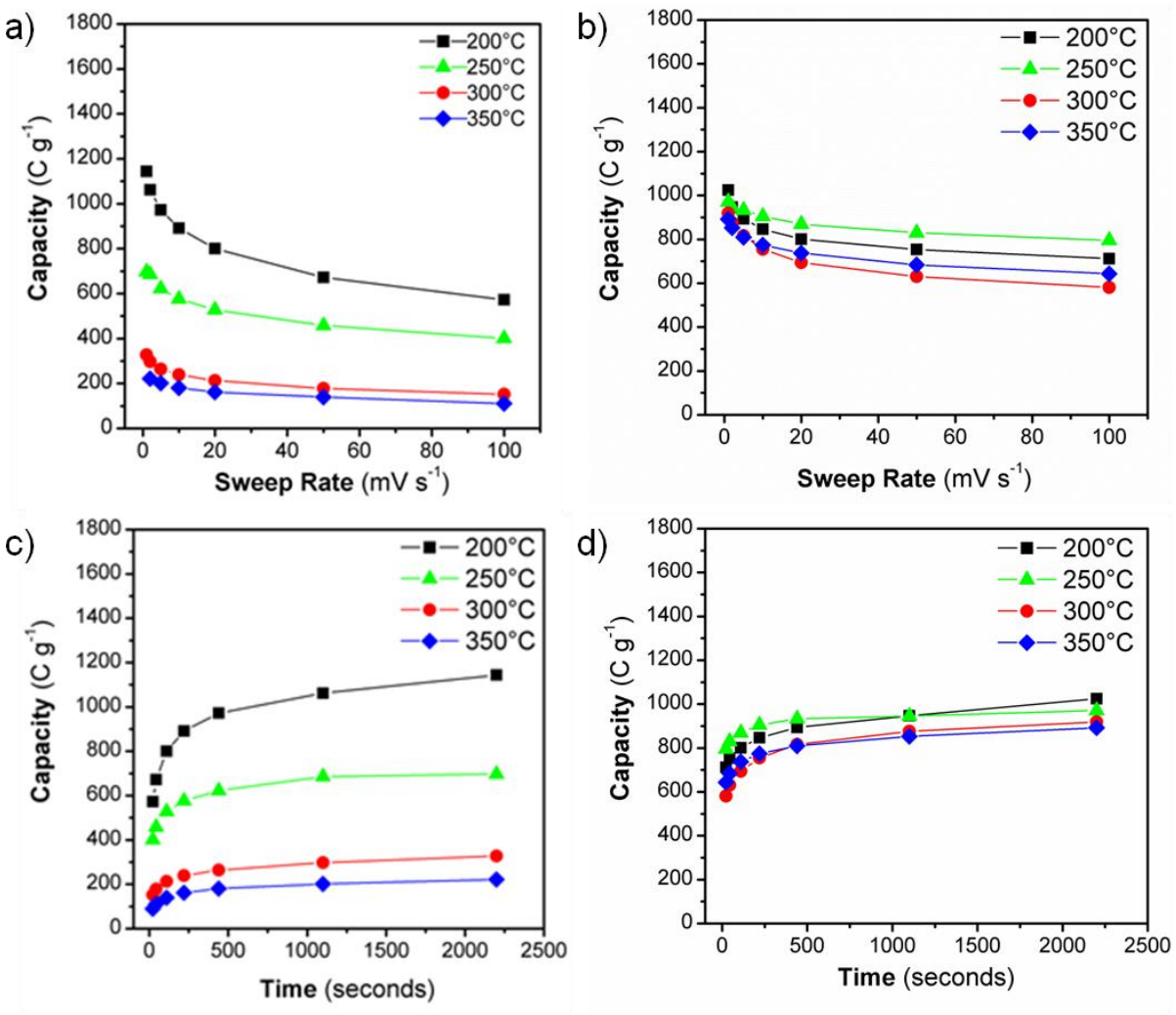

Figure 5.8. (a) Charge storage dependence on sweep rate for mesoporous ITO films coated with a 7 nm layer of V_2O_5 heated to 200, 250, 300 and 350 °C. (b) Charge storage dependence on sweep rate for flat ITO coated with a 7 nm layer of V_2O_5 heated to 200, 250, 300 and 350 °C. (c) Comparison of charging rates calculated from cyclic voltammetric data at various sweep rates for mesoporous ITO films coated with a 7 nm layer of V_2O_5 heated to 200, 250, 300 and 350 °C. (d) Comparison of charging rates calculated from cyclic voltammetric data at various sweep rates for flat ITO coated with a 7 nm layer of V_2O_5 heated to 200 , 250, 300 and 350 °C.

°C have the highest capacity and the capacity decreases by half for films heated to 250 °C. The capacity is nearly lost for films heated to both 300 and 350 °C. Figure 5.8c shows the charge storage dependence, plotted as capacity versus charging times at all temperatures. The same trend is observed for all temperatures, where the capacity increases with longer charging times, again suggesting V_2O_5 is not fully charged at shorter charging times due to slow diffusion of Li^+ ions. In Figure 5.8c, after a charging time of ~200 s, the total charge stored at 200 °C is 900 C/g, compared to 600 C/g 250 °C, and ~200 C/g for both 300 and 350 °C. To better understand the role of intrinsic kinetic limitations arising from lithium transport in the vanadia layer compared to architectural limitations (pore blocking, electrical conductivity, limited electrolyte diffusion, etc.), we performed CV measurements on flat films of V_2O_5 coated

onto flat ITO substrates and heated to the same temperatures (200, 250, 300, and 350 °C). Figure 5.8b compares the charge storage dependence of flat 7 nm V_2O_5 at sweep rates ranging from 1 – 100 mV/s. Interestingly, the capacity at all temperatures is less dependent on the sweep rate for flat films in Figure 5.8b compared to porous films in Figure 5.8a, suggesting that solvent diffusion through the pore system or electrical conductivity in the porous ITO network may contribute to the kinetic limitations. In addition, despite the fact that the films heated to higher temperature are more crystalline, the capacity is similar at all temperatures to within experimental error, a result that makes sense given that grain growth cannot block pores in a flat film. Moreover, none of these films were heated high enough to drive a phase transition to the monoclinic phase. Figure 5.8d shows the charge storage dependence plotted as capacity versus charging times for the flat V_2O_5 films. At all temperatures, the V_2O_5 is fully charged by ~200 s, to within experimental error. This suggests the storage of Li+ ions occurs by fast surface redox reactions at all temperatures, and the kinetic limitations in the porous films result from

architectural factors. Similar experiments were also performed on 2 nm V_2O_5 layers coated onto flat ITO. Unfortunately, the mass loading for flat 2 nm V_2O_5 layers was too low to obtain meaningful gravimetrically normalized capacity data. While the data is not included here and cannot be discussed in detail, it is worth noting that the general trend in the data was very similar to the trends observed in Figures 5.5a and b with sample heated to 450 ºC showing about half the capacity of the low temperature samples, likely due to a crystal growth and phase transition to a less redox active phase at high T.

5.2.4 Pseudocapacitance in ITO-V_2O_5 composites

As discussed above, pore blocking caused by grain growth can have a significant effect on total capacity measurements. Kinetic studies, which ask what fraction of the total capacity is non-diffusion controlled (and thus capacitive), provide an alternative way to analyze the electrochemical results that is less sensitive to this pore blocking. We thus follow previously reported work to quantitatively determine the capacitive contribution to the current response by using the voltammetric sweep rate dependence of the current.[48] In this analysis, the total current can be separated into two components based on their relationship to the sweep rate of a cyclic voltammetry experiment (v, in mV/s). One of these components arises from semi-infinite diffusion processes and varies with $v^{-1/2}$ and the other is related to capacitive (or surface) processes and varies linearly with v. Therefore, the current response (i) at a fixed potential (V) can be described as the combination of these two separate mechanisms:

$$i(\mathrm{V}) = k_1 v + k_2 v^{1/2}$$

where k_1 and k_2 are constants at a particular sweep rate . By determining both k_1 and k_2, we can use the above equation to distinguish between the currents arising from diffusion processes and those from capacitive effects, as previously demonstrated.[**Error! Bookmark not defined.**]

Figure 5.9 shows the total stored charge for mesoporous ITO coated with 2 nm and 7 nm V_2O_5 layers heated to 200 °C at two different sweep rates, 1 and 10 mV/s. The total current or stored charge (total area integrated under the CV curves) is divided into diffusion-controlled and capacitive (non-diffusion) charge storage. In Figure 5.9 a – b and d – e, the shaded area represents the capacitive current and the white area represents the diffusion-controlled current contributions to the total stored charge. The gravimetrically normalized stored charge, divided into capacitive (shaded area) and diffusion-controlled (white area) contributions, is represented in Figure 5.9c (1 mV/s) and Figure 5.9f (10 mV/s).

At a slow sweep rate of 1 mV/s, 2 nm V_2O_5 features a slightly higher diffusion-controlled capacity (~500 C/g) than 7 nm V_2O_5 (~400 C/g). This can be explained by the higher porosity observed in 2 nm V_2O_5 (Figure 5.4c) compared to 7 nm V_2O_5 (Figure 5.4e), resulting in more accessible redox sites with shorter diffusion path lengths for the electrolyte. In addition, 2 nm V_2O_5 shows a higher amount of total stored charge (~1700 C/g) compared to 7 nm V_2O_5 (~1100 C/g), as well as a higher capacitive charge storage (~ 1200 C/g) compared to 7 nm V_2O_5 (~700 C/g). These results suggest that there are more redox sites available for fast charge storage in 2 nm V_2O_5, likely due to a higher surface area resulting from a higher pore volume (Figure 5.4c). These results also reveal that the surface area loss that is observed in 7 nm V_2O_5, due to grain growth that clogs the smaller pores (Figure 5.2e and Figure 5.4e), inhibits capacitive charge storage and impedes diffusion-controlled processes. Despite these differences in total mass

normalized capacity, the fraction of the total stored charge that is capacitive in both materials is similar, indicating similar kinetics for diffusion of Li^+ into both thick and thin vanadia layers.

Figure 5.9f shows the gravimetrically normalized capacities for 2 and 7 nm V_2O_5 cycled at a faster sweep rate (10 mV/s). Since the capacitive charge storage is unaffected by the increase in sweep rate the value is the same as at 1 mV/s for each thickness. This can be explained by the presence of both double-layer and pseudocapacitive processes that are not kinetically limited. By contrast, any slow diffusion of Li+ ions into V_2O_5 is reduced because the Li+ ions have less time to diffuse into the V_2O_5 network. Therefore, the relative capacitive contribution to the total stored charge is greater for both 2 and 7 nm V_2O_5 compared to the contribution from diffusion-controlled mechanisms. Again, both 2 and 7 nm V_2O_5 layers show similar and very high capacitive contributions at 90% and 87%, respectively, of the total stored charge is coming from non-diffusion controlled processes.

All of the data discussed above has been gravimetrically normalized to the total vanadia content, but the samples with 7nm thick vanadia coating obviously contain more vanadia per unit film area. This can be easily seen in the CV curves in Figure 5.9 a – b and d – e, which shows that the total stored charge (area under CV curve, not gravimetrically normalized) is greater for 7 nm V_2O_5 compared to 2 nm V_2O_5. Much less of this vanadia mass is exposed to the electrolyte in the 7 nm thick V_2O_5 samples, however. If we look at the shape of CVs for 2 nm versus 7 nm V_2O_5, there are more defined redox peaks for 7 nm V_2O_5 suggesting the structure is more ordered and feature more specific redox sites in the V_2O_5 lattice. Both of these facts lead us to conclude that the 7 nm thick samples must be storing more charge in the bulk that is pseudocapacitive than samples with 2 nm thick layers (i.e. samples with 7 nm thick layers show higher levels of

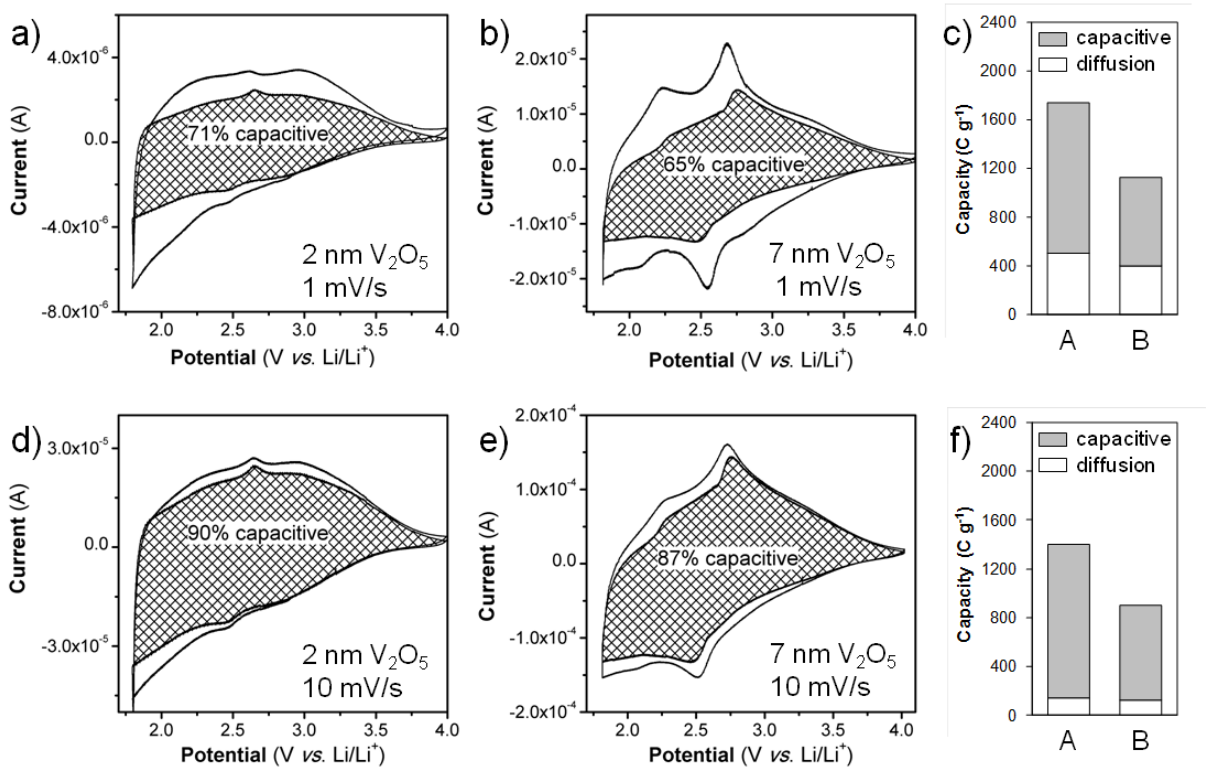

Figure 5.9. Cyclic voltammetric responses for porous ITO films coated with 2 nm (a) and 7 nm (b) layer of V_2O_5 heated to 200°C at sweep rates of 1 mV/s. Cyclic voltammetric responses for the same films, 2 nm (d) and 7 nm (e) layer of V_2O_5, at sweep rates of 10 mV/s. The capacitive contribution to the current is represented as the shaded area. Corresponding comparison of the total stored charge at sweep rates of 1 (c) and 10 (f) mV/s, where A and B represent 2 and 7 nm layer of V_2O_5 heated to 200°C .

intercalation pseudocapacitance).[49] Such conclusions are complicated by overall capacity loss in 7 nm thick samples due to pore blocking, however.

To further investigate the rate capability of the ITO- V_2O_5 composites, we thus examine the normalized capacity versus sweep rate for all conditions as shown in Figure 5.10a. For each curve, the capacity is normalized by setting the total stored charge to a value of 1.0 at slow sweep rates. The 2 nm layer heated to 200 °C shows the best rate capability, but the normalized performance is very similar to that obtained for samples with 2 nm V_2O_5 heated to 350 or 450 °C. This result indicates that the number of redox sites may be limited by phase transitions or pore blocking, but the kinetics of all available redox sites are similarly fast. For samples with a 7 nm thick vanadia film, the rate capability is slower in all cases, in agreement with the idea that this sample must show more intercalation pseudocapacitance with longer diffusion lengths. While there is significant scatter in this data, there is a rough trend that rate capability decreases with increasing temperature, suggesting either that a more crystalline structure leads to slower Li^+ ion diffusion kinetics or that partly blocked pores lead to solution phase barriers for the electrolyte diffusion which add to the solid state barriers for lithium ion diffusion.

Finally, it is important to remember that the ITO conductor is a major component of this system and that ITO has significant mass. Figure 5.10b compares the charge storage and rate capability of mesoporous ITO coated 2 nm and 7 nm layer of V_2O_5 considering only the vanadia mass, the double layer capacity of the bare mesoporous ITO, and both thick and thin ITO-V_2O_5 composites including the mass for both ITO and V_2O_5. As expected, the bare mesoporous ITO electrode shows very high rate capability but low gravimetrically normalized capacity and capacitance arising only from the electrical double-layer. When the mass of the mesoporous ITO scaffold is included in the calculated gravimetrically normalized capacity and capacitance, as

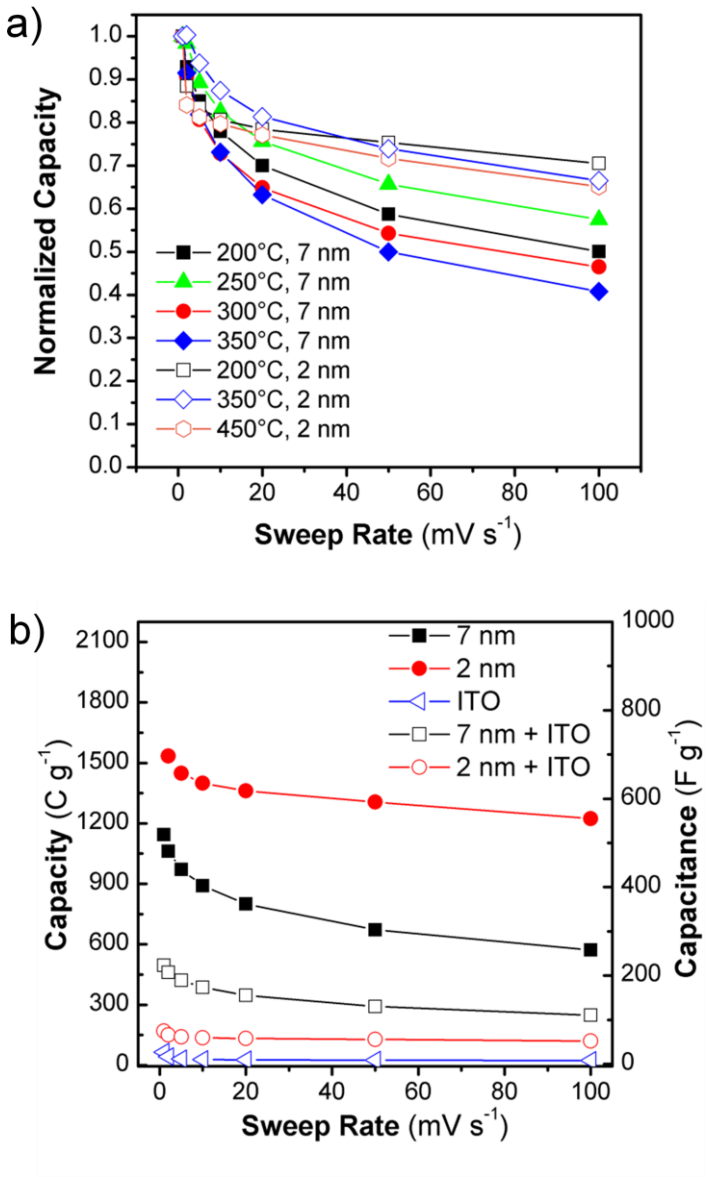

Figure 5.10. (a) Comparison of normalized capacity versus sweep rate calculated from cyclic voltammetric data at various sweep rates for porous ITO coated 2 nm and 7 nm layer of V_2O_5 via ALD heated to various temperatures. (b) Comparison of the rate capability of porous ITO coated 2 nm and 7 nm layer of V_2O_5, bare mesoporous ITO, and ITO-V_2O_5 composites including the mass loading for both ITO and V_2O_5.

expected, the values decrease significantly since both the 2 nm and 7 nm V_2O_5 layers account for only a small fraction of the total electrode mass. While the 2 nm ITO-V_2O_5 composite shows better rate capability than the 7 nm ITO-V_2O_5 composite, the capacity at all sweep rates is about twice as high for the 7 nm ITO-V_2O_5 composite compared to the 2 nm ITO-V_2O_5, stemming from the fact that the thicker layer has a higher V_2O_5 mass loading.

While the mass normalized capacities that include the ITO mass are not particularly high, it is important to note that this is a not meant to be a commercial battery system, but rather a proof-of-concept exploration of architecture. The mass of ITO, which includes two heavy elements, is anomalously high for a conductor, so its total effect on the mass normalized capacity is disproportionately high. The more important results of this work are an increased understanding of the important factors needed to design a core-shell porous network for pseudocapacitive charge storage. Specifically, we observe pseudocapacitance up to a thickness of 7 nm V_2O_5, which is the limit for our system, as any thicker layer leads to blockage of the pores.

5.3 Conclusions

In this work, we explored the design of nanoscale pseudocapacitor architecture, constructed using templating of conducting ITO nanocrystals to form a high surface area mesoporous scaffold, followed by coating these porous conductors with a redox-active layer of V_2O_5 to produce nanoporous composites for pseudocapacitive energy storage. By varying the thickness of the V_2O_5 layer as well as the extent of crystallization through various annealing temperatures, the charge storage behavior and rate capability of the composites were examined.

Thin V_2O_5 layers (2 nm) feature on open interconnected porosity and a high surface area, leading to charge storage arising primarily from capacitive processes. Thicker layers showed increased capacity on an area normalized basis, but reduced capacity on a mass normalized basis, indicating that electrolyte accessible to some of the pores was blocked.

The crystal structure was also found to play a role in the charge storage behavior in our composites. In general, modest heating to crystallize the V_2O_5 to the orthorhombic phase ($T \leq 350$ ºC) led to higher pseudocapacitance. Heating V_2O_5 to temperatures high enough to form the monoclinic phase (>400 ºC) led to a decrease in total charge storage and rate capability, again indicating that intercalation pseudocapacitance plays a role, even in samples with 2 nm vanadia films. In thick porous layers, heating V_2O_5 led to significant grain growth that blocked access of the electrolyte to the redox sites, which led to a significant drop in capacity. The capacity of flat V_2O_5 films did not decrease with heating, however, indicating that the reduced capacity in the porous samples with 7 nm thick vanadia layers stemmed from architectural changes upon heating, rather than changes in lithium ion diffusion as the vanadia crystallized.

Taken together, these results provide significant insight on the design of pseudocapacitive materials using a core-shell architecture. Thin shells retain the high surface area of the host conductor and show good kinetics, but the total mass loading of redox active material is not high. Thicker films solve the problem of low mass loading, and if the crystal structure is optimized for Li^+ insertion, near surface redox sites several nm into the material can show fast redox kinetics. Thick films in a core-shell structure can lead to a loss of surface area and pore access, however, and have significant potential for grain growth and structural rearrangement upon thermal processing. Based on our findings, an ideal pseudocapacitor architecture features a high surface area conductor with pores just large enough that they can be coated with an moderately thick

layer of active material to form a high surface area core-shell structure that exhibits an open interconnected porosity. By applying these fundamental design rules, it may become possible to build pseudocapacitor materials that will achieve high charge storage while maintaining fast charging/discharging kinetics.

5.4 Experimental Section

5.4.1 Materials. The following chemicals were purchased and used as received: oleylamine (90% Aldrich), oleic acid (90%, Aldrich), indium acetylacetonate (99.99+%, Aldrich), tin bis(acetylacetonate) dichloride (98%, Aldrich), nitrosonium tetrafluoroborate (95%, Aldrich), Vanadium tri-isopropoxide, (96%, Alfa Aesar). Poly((ethylene-*alt*-propylene)-*block*-poly(ethylene oxide), with a mass ratio of PEP(3900)-*b*-PEO(4000), a block ratio of PEP_{56}-*b*-PEO_{91}, and with a PDI = 1.05, was synthesized using reported methods.[50],[51] Briefly, polyisoprene was grown by anionic polymerization, terminated with an -OH group and then hydrogenated over Pd/C. The resulting PEP-OH was subsequently extended by anionic polymerization of ethylene oxide.

5.4.2 Synthesis and Ligand-exchange of Nanocrystals: Previously reported procedures were followed to synthesize 7–8 nm and 4–5 nm ITO nanocrystals that were stabilized by either oleylamine or oleic acid ligands.[52,53,54] All as-synthesized nanocrystals were purified and dispersed in hexane (10-15 mg/mL). To carry out the ligand-exchange process, as-synthesized nanocrystals were treated with nitrosonium tetrafluoroborate ($NOBF_4$) according to a recently reported procedure.[**Error! Bookmark not defined.**] In a typical ligand-exchange reaction, 5 mL of nanocrystal dispersion in hexane was combined with 5 mL of $NOBF_4$ solution in N, N-

dimethylformamide (DMF) (10 mg/mL) with stirring (5 min), or until the nanocrystals were transferred to the DMF phase. The nanocrystals were precipitated with toluene then centrifuged, followed by multiple washings with DMF/toluene. The ligand-stripped nanocrystals were dispersed in DMF/ethanol (1:10 v/v) to give a final concentration of 15-20 mg/mL.

*5.4.3 Synthesis of Mesoporous Nanocrystal-based Films***:** The synthesis of mesoporous ITO nanocrystal-based films was previously reported.[30] Briefly, in a typical synthesis, 40 mg of the desired diblock copolymer was dissolved in 0.5 mL of ethanol with gentle heating. To this solution, 3 mL of the desired nanocrystals in DMF/ethanol (20 mg/mL) was added. From this mixture, thin films were produced by dip-coating onto polar substrates at a constant withdrawal rate of 1–10 mm/s with a constant 30% relative humidity. Thin films were also prepared by spin-coating onto polar substrates at 1000 to 2000 rpm for 60 s. The films were dried using a 3 h ramp up to 175 °C, followed by a 3 h soak. Thermal decomposition of the template was done after the drying step using a 6 h ramp from 175 °C to 450 °C, followed by a 3 h soak.

*5.4.4 Synthesis of V_2O_5-ITO composites***:** The ALD V_2O_5 process was performed in a commercial BENEQ TFS 500 reactor, which has a base pressure of 2 mbar. Vanadium tri-isopropoxide, $VO(OC_3H_7)_3$ (VTOP), was used as the vanadium precursor, which was kept at 45^{o}C giving a vapor pressure of ~0.29 torr. Ozone or water was used as the oxidant. O_3 with 18wt% was generated from pure O_2 source by a MKS O3MEGA ozone delivery system. Ozone ALD was done at 170 ^{o}C while water ALD was done at 120 ^{o}C. The film thickness was measured ex-situ using a SOPRA GES5 spectroscopic ellipsometer. The 2 and 7 nm V_2O_5 film was done with 100 and 250 ALD cycles respectively. One ALD cycle includes 0.5 s VTOP pulse, 1 s N_2 purge, 2 s oxidant pulse and 1 s N_2 purge. After coated with V_2O_5, the ITO films were post-annealed in oxygen for 60 s using an AG Associates 410 rapid thermal annealer at

200, 250, 300, 350 and 450 ^{o}C. The thickness of the films is estimated based on the number of ALD cycles.

5.4.5 Methods: The mass of the V_2O_5 composites was determined by inductively coupled plasma optical emission spectroscopy (ICP-OES), performed on a TJA RADIAL IRIS 1000**.** Transmission electron microscopy (TEM) images were obtained using an FEI/PHILIPS CM120 electron microscope operating at 120 kV. Scanning electron microscopy (SEM) images were obtained using a JEOL model 6700F electron microscope with beam energy 5 kV. 2D small-angle X-ray scattering (2D-SAXS) data were collected at the Stanford Synchrotron Radiation Laboratory using beamline 1-4 using the Rayonix165 large angle CCD detector. All measurements were performed in reflection geometry. XPS analysis was performed using a Kratos Axis Ultra DLD with a monochromatic (K_α radiation) source. The charge neutralizer filament was used to control charging of the sample. A 20 eV pass energy was used with a 0.05 eV pass energy. Scans were calibrated using the C 1s peak shifted to 284.8 eV. Ellipsometric porosimetry was performed on a PS-1000 instrument from Semilab using toluene as the adsorbate. A UV–visible CCD detector adapted to a grating spectrograph analyzes the signal reflected by the sample. The light source is a 75 W Hamamatsu Xenon lamp and measurements were performed on the spectral range from 1.24-4.5 eV. Data analysis was performed using the associated SEA software with the assumption of slit-like pores. If the actual pores are closer to cylindrical, the real pores sizes will be slightly larger than the values reported here. Data is fit with a contact angle of zero for the solvent. Electrochemical measurements were carried out in a three-electrode cell using a PAR EG&G 273A potentiostat in an argon-filled glovebox, with oxygen and water levels <1 ppm. The working electrode consisted of ITO glass upon which ITO-V_2O_5 films were deposited. The electrolyte solution used was 1.0 M $LiClO_4$ in propylene

carbonate (PC) and lithium metal foils were used as the counter and reference electrodes. Cyclic voltammetry was performed using cutoff voltages at 4 and 1.8 V vs. Li/Li^+.

5.5 References

[1] Conway, B. E.; Pell, W. G. Double-layer and Pseudocapacitance Type of Electrochemical Capacitors and their Applications to the Development of Hybrid Devices. *J. Solid State Electrochem.* **2003**, *7*, 637–644.

[2] Miller, J. R.; Simon, P. Electrochemical Capacitors for Energy Management. *Science* **2008**, *321*, 651–652.

[3] Nam, K.-W.; Lee, C.-W.; Yang, X.-Q.; Cho, B. W.; Yoon, W.-S.; Kim, K.-B. Electrodeposited Manganese Oxides on Three-Dimensional Carbon Nanotubes Substrate: Supercapacitive Behavior in Aqueous and Organic Electrolyes. *J. Power Sources* **2002**, *188*, 323–331.

[4] Reddy, A. L. M.; Ramaprabhu, S. Nanocrystalline Metal Oxides Dispersed Multiwalled Carbon Nanotubes as Supercapacitor Electrodes. *J. Phys. Chem. C* **2007**, *111*, 7727–7734.

[5] Zhao, X.; Hayner, C. M.; Kung, H. H. Self-Assembled Lithium Manganese Oxide Nanoparticles on Carbon Nanotubes or Graphene as High-Performance Cathode Material for Lithium-Ion Batteries. *J. Mater. Chem.* **2011**, *21*, 17297–17303.

[6] Sathiya, M.; Prakash, A. S.; Ramesha, K.; Tarascon, J.-M.; Shukla, A. K. V_2O_5-Anchored Carbon Nanotubes for Enhanced Electrochemical Energy Storage. *J. Am. Chem. Soc.* **2011**, *133*, 16291–16299.

[7] Chen, Z.; Augustyn, V.; Wen, J.; Zhang, Y.; Shen, M.; Dunn, B.; Lu, Y. High-Performance Supercapacitors based on Intertwined CNT/V_2O_5 Nanowire Nanocomposites. *Adv. Mater.* **2011**, *23*, 791–795.

[8] Kim, I.-H.; Kim, J.-H.; Cho, B.-W.; Kim, K.-B. Pseudocapacitive Properties of Electrochemically Prepared Vanadium Oxide on Carbon Nanotubes Film Substrate. *J. Electrochem. Soc.* **2006**, *153*, A1451–A1458.

[9] Sakamoto, J. S.; Dunn, B.; *Journal of The Electrochemical Society*, **2002**, 149 A26-A30

[10] Chen, X.; Zhu, H.; Chen, Y-C.; Shang, Y.; Cao, A.; Hu, L.; Rubloff, G. MWCNT/V_2O_5 Core/Shell Sponge for High Areal Capacity and Power Density Li-Ion Cathodes. *ACS Nano* **2012**, 6, 7948-7955

[11] Chen, W.; Li, S.; Chen, C.; Yan, L. Self-Assembly and Embedding of Nanoparticles by In Situ Reduced Graphene for Preparation of a 3D Graphene/Nanoparticle Aerogel. *Adv. Mater.* **2011**, *23*, 5679–5683.

[12] Wang, D.; Kou, R.; Choi, D.; Yang, Z.; Nie, Z.; Li, J.; Saraf, L. V.; Hu, D.; Zhang, J.; Graff, G. L.; Liu, J.; Pope, M. A.; Aksay, I. A. Ternary Self-Assembly of Ordered Metal Oxide-Graphene Nanocomposites for Electrochemical Energy Storage. *ACS Nano* **2010**, *4*, 1587–1595.

[13] Wang, H.; Casalongue, H. S.; Liang, Y.; Dai, H. $Ni(OH)_2$ Nanoplates Grown on Graphene as Advanced Electrochemical Pseudocapacitor Materials. *J. Am. Chem. Soc.* **2010**, *132*, 7472–7477.

[14] Yu, G.; Hu, L.; Liu, N.; Wang, H.; Vosgueritchian, M.; Yang, Y.; Cui, Y.; Bao, Z. Enhancing the Supercapacitor Performance of Graphene/MnO_2 Nanostructured Electrodes by Conductive Wrapping. *Nano Lett.* **2011**, *11*, 4438–4442.

[15] Lytle, J. C.; Wallace, J. M.; Sassin, M. B.; Barrow, A. J.; Long, J. W.; Dysart, J. L.; Renninger, C. H.; Saunders, M.P.; Brandella, N. L.; Rolison, D. R. The Right Kind of Interior for Multifunctional Electrode Architectures: Carbon Nanofoam Papers with

Aperiodic Submicrometre Pore Networks Interconnected in 3D. *Energy Environ. Sci*. **2011**, 4, 1913

[16] Long, J. W.; Rolison, D. R. Architectural Design, Interior Decoration, and Three-Dimensional Plumbing en Route to Multifunctional Nanoarchitectures. *Acc. Chem. Res*. **2007**, 40, 854–862

[17] Zhang, H.; Yu, X.; Braun, P. V. Three-Dimensional Bicontinuous Ultrafast-Charge and -Discharge Bulk Battery Electrodes. *Nat. Nanotech*. **2011**, *6*, 277–281.

[18] Lang, X.; Hirata, A.; Fujita, T. Chen, M. Nanoporous Metal/Oxide Hybrid Electrodes for Electrochemical Supercapacitors. *Nat. Nanotech*. **2011**, *6*, 232–236.

[19] Li, J.; Yang, Q. M.; Zhitomirsky, I. Nickel Foam-Based Manganese Dioxide-Carbon Nanotubes Composite Electrodes for Electrochemical Supercapacitors. *J. Power Sources* **2008**, *185*, 1569–1574.

[20] McDonough, J. R.; Choi, J. W.; Yang, Y.; La Mantia, F.; Zhang, Y.; Cui, Y. Carbon Nanofiber Supercapacitors with Large Areal Capacitances. *Appl. Phys. Lett*. **2009**, *95*, 243109(1–3).

[21] Taberna, P. L.; Mitra, S.; Poizot, P.; Simon, P.; Tarascon, J.-M. High Rate Capabilities Fe_3O_4-Based Cu Nano-Architectured Electrodes for Lithium-Ion Battery Applications. *Nat. Mater*. **2006**, *5*, 567–573.

[22] Kim, J.-H.; Myung, S.-T.; Sun, Y.-K. Molten Salt Synthesis of $LiNi_{0.5}Mn_{1.5}O_4$ Spinel for 5V Class Cathode Material of Li-Ion Secondary Battery. *Electrochem. Acta* **2004**, *49*, 219–227.

[23] Brezesinski, T.; Wang, J.; Polleux, J.; Dunn, B.; Tolbert, S. H. Templated Nanocrystal-Based Porous TiO_2 Films for Next-Generation Electrochemical Capacitors. *J. Am. Chem. Soc.* **2009,** *131*, 1802–1809.

[24] Szeifert, J. M.; Feckl, J. M.; Fattakhova-Rohlfing, D.; Liu, Y.; Kalousek, V.; Rathousky, J.; Bein, T. Ultrasmall Titania Nanocrystals and Their Direct Assembly into Mesoporous Structures Showing Fast Lithium Insertion. *J. Am. Chem. Soc.* **2010,** *132*, 12605–12611.

[25] Warren, S. C.; Messina, L. C.; Slaughter, L. S.; Kamperman, M.; Zhou, Q.; Gruner, S. M.; DiSalvo, F. J.; Wiesner, U. Ordered Mesoporous Materials from Metal Nanoparticle-Block Copolymer Self-Assembly. *Science* **2008**, *320*, 1748–1752.

[26] Corma, A.; Atienzar, P.; Garcia, H.; Chane-Ching, J. Y. Hierarchically Mesostructured Doped CeO_2 with Potential for Solar-Cell Use. *Nat. Mater.* **2004**, *3*, 394–397.

[27] Deshpande, A. S.; Pinna, N.; Smarsly, B.; Antonietti, M.; Niederberger, M. Controlled Assembly of Preformed Ceria Nanocrystals into Highly Ordered 3D Nanostructures. *Small* **2005**, *1*, 313–316.

[28] Ba, J. H.; Polleux, J.; Antonietti, M.; Niederberger, M. Non-aqueous Synthesis of Tin Oxide Nanocrystals and Their Assembly into Ordered Porous Mesostructures. *Adv. Mater.* **2005**, *17*, 2509–2512.

[29] Dong, A.; Ye, X.; Chen, J.; Kang, Y.; Gordon, T.; Kikkawa, J. M.; Murray, C. B. A Generalized Ligand-Exchange Strategy Enabling Sequential Surface Functionalization of Colloidal Nanocrystals. *J. Am. Chem. Soc.* **2011,** *133*, 998–1006.

[30] Rauda, I. E.; Buonsanti, R.; Saldarriaga-Lopez, L. C.; Benjauthrit, K.; Schelhas, L. T.; Stefik, M.; Augustyn, V.; Ko, J.; Dunn, B.; Wiesner, U.; Milliron, D. J.; Tolbert, S. H. A

General Method for the Synthesis of Hierarchical Nanocrytal-Based Mesoporous Materials. *ACS Nano*, **2012**, 6, 6386–6399.

[31] Rauda, I. E.; Saldarriaga-Lopez, L. C.; Helms, B. A.; Schelhas, L. T.; Membreno, D.; Milliron, D. J.; Tolbert, S. H. Nanoporous Semiconductors Synthesized Through

Polymer Templating of Ligand-Stripped CdSe Nanocrystals. *Adv. Mater.* **2013**, *25*, 1315–1322

[32] Buonsanti, R.; Pick, T. E.; Krins, N.; Richardson, T. J.; Helms, B. A.; Milliron, D. J.; Assembly of ligand-stripped nanocrystals into precisely controlled mesoporous architectures. *Nano Lett.* **2012**, *12*, 3872–3877.

[33] Chen, X.; Pomerantseva, E.; Banerjee, P.; Gregorczyk, K.;Ghodssi, R.; Rubloff, G. Ozone-Based Atomic Layer Deposition of Crystalline V_2O_5 Films for High Performance Electrochemical Energy Storage. *Chem. Mater*. **2012**, *24*, 1255–1261.

[34] Chen, X.; Pomerantseva, E.; Gregorczyk, K.; Ghodssi, R.; Rubloff, G. Cathodic ALD V_2O_5 Thin Film for High-rate Electrochemical Energy Storage. *RSC Adv*. 2013,3, 4294-4302

[35] Giltsrap, R. A.; Capozzi, C. J.; Carson, C. G.; Gerhardt, R. A.; Summers, C. J. Synthesis of a Nonagglomerated Indium Tin Oxide Nanoparticle Dispersion. *Adv. Mater.* **2008**, *20*, 4163–4166.

[36] Choi, S. I.; Nam, K. M.; Park, B. K.; Seo, W. S.; Park, J. T. Preparation and Optical Properties of Colloidal, Monodisperse, and Highly Crystalline ITO Nanoparticles. *Chem. Mater.* **2008**, *20*, 2609–2611.

[37] Choi, S. I.; Nam, K. M.; Park, B. K.; Seo, W. S.; Park, J. T. Preparation and Optical Properties of Colloidal, Monodisperse, and Highly Crystalline ITO Nanoparticles. *Chem. Mater*. **2008**, *20*, 2609–2611.

[38] Lu, Y.; Ganguli, R.; Drewien, C. A.; Anderson, M. T.; Brinker, C. J.; Gong, W.; Guo, Y.; Soyez, H.; Dunn, B.; Huang, M. H.; *et al.* Continuous Formation of Supported Cubic and Hexagonal Mesoporous Films by Sol-Gel Dip-Coating. *Nature* **1997**, *389*, 364–368.

[39] Baklonov, M. R.; Mogilnikov, K. P.; Polovinkin, V. G.; Dultsev, F. N. Determination of Pore Size Distribution in Thin Films by Ellipsometric Porosimetry. *J. of Vac. Sci. & Tech. B* **2000**, *18*, 1385–1391.

[40] Gregg, S. J.; Sing, K. S. W. *Adsorption, Surface Area, and Porosity*, 2nd ed.; Academic; London, **1982**.

[41] George, S. M. Atomic Layer Deposition: An Overview. *Chemical Reviews* **2010**, *110*, 111–131.

[42] Elam, J. W.; Xiong, G.; Han C. Y.; HauWang, H.; Birrell, J.P.; Welp, U.; Hryn, J.N.; Pellin, M. J.; Baumann, T. F.; Poco, J. F.; Satcher Jr, J. H. *Journal of Nanomaterials*. **2006**, 1–5

[43] Silversmit, G.; Depla, D.; Poelman, H.; Marin, G. B.; De Gryse, R. Determination of the V2p XPS Binding Energies for Different Vanadium Oxidation States (V^{5+} to V^{0+}). J. Electron. Spectrosc. *Relat. Phenom.* **2004**, *135*, 167–175.

[44] Livage, J. Vanadium Pentoxide Gels. *Chem. Mater*. **1991**, *3*, 578–593.

[45] Wang, Y.; Takahashi, K.; Lee, K.; Cao, G. Nanostructured Vanadium Oxide Electrodes for Enhanced Lithium-Ion Intercalation. *Adv. Funct. Mater*. **2006**, *16*, 1133–1144.

[46] Talledo, A.; Valdivia, H. Investigation of Oxide (V_2O_5) Thin Films as Electrodes for Rechargeable Microbatteries Using Li. *J. Va. Sci. Technol. A* **2003**, *21*, 1494–1499.

[47] Chen, X.; Pomerantseva, E.; Gregorczyk , K.; Ghodssi, R.; Rubloff, G. Cathodic ALD V_2O_5 thin film for high-rate electrochemical energy storage. *RSC Adv*. **2013**, 3, 4294-4302

[48] T.-C. Liu, W.G. Pell, B.E. Conway, S.L. Roberson. *J. Electrochem. Soc.* **1998,** 145, 1882–1888.

[49] Augustyn, V.; Come, J.; Lowe, M. A.; Kim, J. W.; Taberna, P-L.; Tolbert, S. H.; Abruña, H. D.; Simon, P.; Dunn, B. High-rate Electrochemical Energy Storage through Li^+ Intercalation Pseudocapacitance. *Adv. Energy Mater*. **2012**, 2, 141–148

[50] Hillmyer, M. A.; Bates, F. S. Synthesis and Characterization of Model Polyalkane-Poly(ethylene oxide) Block Copolymers. *Macromolecules* **1996**, *29*, 6994–7002.

[51] Allgaier, J.; Poppe, A.; Willner, L.; Richter, D. Synthesis and Characterization of Poly[1,4-Isoprene-b-(ethylene oxide)] and Poly[ethylene-co-propylene-b-(ethylene oxide)] Block Copolymers. *Macromolecules* **1997**, *30*, 1582–1586.

[52] Llordes, A.; Hammack, A. T.; Buonsanti, R.; Tangirala, R.; Aloni, S.; Helms, B. A.; Milliron, D. J. Polyoxometalates and Colloidal Nanocrystals as Building Blocks for Metal Oxide Nanocomposite Films. *J. Mater. Chem.* **2011,** *21*, 11631–11638.

[53] Choi, S. I.; Nam, K. M.; Park, B. K.; Seo, W. S.; Park, J. T. Preparation and Optical Properties of Colloidal, Monodisperse, and Highly Crystalline ITO Nanoparticles. *Chem. Mater.* **2008**, *20*, 2609–2611.

[54] Giltsrap, R. A.; Capozzi, C. J.; Carson, C. G.; Gerhardt, R. A.; Summers, C. J. Synthesis of a Nonagglomerated Indium Tin Oxide Nanoparticle Dispersion. *Adv. Mater.* **2008**, *20*, 4163–4166.

CHAPTER 6

Room Temperature Surface Area Measurement of Thin Films by Ellipsometric-Porosimetry

6.1 Introduction

Mesoporous thin films of many types of materials have been successfully prepared recently and there is a vast amount of applications with increasing technological importance, such as support as catalyst, electronic devices, and for uses in electrochemical capacitors and solar cells.[1–6] The full potential of such materials can be realized only if they are well characterized, and such characterization should include accurate measurement of total surface area. Nitrogen porosimetry in conjunction with BET analysis is commonly used for bulk materials that posses a high surface area, where the minimum surface area needed is $1m^2$. In thin films this surface area is difficult to obtain since we are limited by the amount of material in the sample

In thin films surface area is an important measurement to quantify the portion of the architecture that is available for chemistry. For example in batteries and pseudocapacitors there is a need to maximize the surface area of a material to increase the number of redox active sites which controls the capacitance of the film.[2,3,7] Being able to measure surface area allows us to modify [7]the synthesis of the material to maximize this parameter. In heterogeneous catalysis surface area is also important as it maximizes the amount of catalyst that can be loaded.[1,8] And in some types of solar cells where thin films are being used, increasing the surface area of the porous electrode would produce a more efficient solar cell.[4,5]

Few techniques are used to measure surface area currently in thin films. One method used is krypton porosimetry,[9,10] which uses krypton gas at either liquid krypton or liquid nitrogen temperatures. This technique has higher sensitivity measuring films with surface areas of less than 1 m^2/g, because it is using an adsorbate below its boiling point which allows for the quantity of gas in the dead space to be reduced permitting the volume adsorbed to be obtained more accurately. This technique is not useful for characterization of materials with large surface areas[11] because at the low pressures in which the system works, the equilibrium liquid-vapor pressure of krypton is either not fully reached or it reaches the point of solidification, not allowing for the solvent to fully fill the pores.[10]

Another method that can be used to measure surface area of thin films is nitrogen adsorption coupled with a Quartz Crystal Microbalance (QCM), this method works well, as the QCM is extremely sensitive to monolayer adsorption of molecules, however the major limitation here is that films must be deposited directly onto QCM substrates, and those substrate can only tolerate moderately high temperatures.[7] Therefore this method becomes inadequate when a material has to be crystallized or treated at high temperatures to form the needed porous architecture.[12,13]

For several years, a growing effort has been made to develop new simple, rapid, non-destructive and reliable techniques allowing the characterization of the porous structure of thin films for industrial production and laboratory investigations. Ellipsometric Porosimetry (EP), a recently developed technique is very powerful as it allows characterization of the porosity and pore size of micro and mesopores in thin films.[14–16] This technique relies on the change of refractive index of the film upon adsorption and desorption of a solvent controlled by changes in the partial pressure in the sample chamber at room temperature. For the measurement to be

accurate, the film must be of good optical quality. However, there are no limits to the substrate that can be used. Currently a commercially available EP device is produced by SEMILAB[17] which has incorporated 4 different solvents to measure porosity and pore size distribution depending on the material being analyzed.

Still one challenge that remains is the measurement of a surface area. With the conventional EP system, at room temperature, the BET region is compressed using toluene, isopropanol or water. The boiling point of these solvents is much higher than room temperature and the sample chamber is not temperature controlled so multilayer adsorption of the solvent occurs fast and no BET region can be obtained.

BET theory is used to determine of the amount of the adsorbate or adsorptive gas required to cover the external and the accessible internal pore surface of a solid with a complete monolayer of adsorbate allowing us to calculate a surface area of the material.[18,19] This monolayer capacity can be calculated from the adsorption isotherm by means of the BET equation

$$\frac{\mathrm{P}}{\mathrm{Vads}(\mathrm{Po}-\mathrm{P})}=\frac{1}{\mathrm{VmC}}+\frac{(\mathrm{C}-1)}{\mathrm{VmC}}*\frac{\mathrm{P}}{\mathrm{Po}}$$

where V_{ads} is the amount of gas adsorbed, V_m is the volume of the monolayer and C is a parameter related to the binding energy between the adsorbate and the surface for the first monolayer and a second binding energy for adsorption of subsequent monolayers. From the linear plot of $P/V_{ads}(P-P_o)$ vs P/P_o, C and V_m can be extracted and a surface area can be calculated. BET theory assumes a strong interaction of the solvent to the surface in the first monolayer and this is plays a significant role in the linear plot as parameter C in the above equation. If the heat of adsorption is stronger than the heat of liquefaction then BET holds reasonably well and the assumption that monolayer by monolayer build up occurs is appropriate.

However if the interaction of the solvent to the surface is not strong enough then multilayer adsorption will occur because the interaction of the solvent with itself is stronger and BET theory may not hold in the relative pressure range from 0.05 to 0.3.[20,21]

In this work, we describe methods for using ellipsometric-porosimetry at room temperature to measure surface area of a mesoporous film. For this we need to choose a set of solvents that first are compatible with the instrument, have a boiling point near room temperature, and hopefully will have a strong enough interaction with the surface of the film get monolayer adsorption.

One solvent that is compatible with the instrument and has a boiling point near room temperature is isopentane. Isopentane is a good candidate for this type of measurement with a boiling point of 27.7 ºC near room temperature it allows us to be at the liquid-vapor equilibrium and to promote monolayer adsorption of the solvent on the internal pore structure of the film. Non-polar solvents in general, such as isopentane, can have very weak interactions with the surface and this can become a problem if monolayer adsorption is not achieved producing on overestimate of the surface area measurement. To avoid this issue, we have also chosen another solvent, methanol, which is also compatible with the instrument. Methanol should have a stronger interaction with the surface of the film given its polar nature. It is known that one can do porosimetry with gases below their boiling point temperature, as in the case of krypton porosimetry, therefore methanol can serve as a good model system to test the surface area measurement and compare to the area obtained using isopentane giving us two solvent options to measure surface area.

6.2 Results and Discussion

Mesoporous cobalt ferrite films were chosen to do surface area measurements because they are stable in air have an accessible pore surface using toluene porosimetry and have good optical quality.

6.2.1 Structural characterization

A scanning electron microscopy image of a cobalt ferrite film is shown in figure 6.1a. This film was produced from the co-assembly of iron and cobalt precursors around a block copolymer that was calcined at 500 ºC to produce a porous network. The image presented in figure 6.1 shows that the film has an open porosity throughout, it is continuous with no cracks, which is necessary for solvent diffusion, and it is optically of good quality.

6.2.2 Porosimetry and surface area measurements

Toluene adsorption desorption isotherms were obtained on the calcined film to determine the porosity and pore size distribution of the cobalt ferrite film. Figure 6.2a shows a type IV isotherm typical of mesoporous films with an interconnected porosity revealing the film is 30% porous. When a Kelvin model is fit to the isotherm the pore size distribution graphs in figure 6.2b reveal pores with a diameter of 18 nm while the necks have a diameter of 10 nm, this data agrees with what is observed in the SEM images. The isotherm presents a hysteresis typical of mesoporous materials with large pores interconnected by smaller necks. At lower pressures, a fit to the BET region, usually between 0.05 and 0.3 P/P_o, does not produce a linear graph indicating multilayer adsorption on the surface rather than the slow buildup monolayer by monolayer.

Isopentane adsorption and desorption isotherms were also measured for the surface area analysis as well as for comparison to the isotherm with toluene to confirm that the porous part of the film has to be accessible to the solvent. The data obtained using isopentane in figure 6.3a shows an isotherm that reaches a porosity of 30% very similar to the one obtained with toluene,

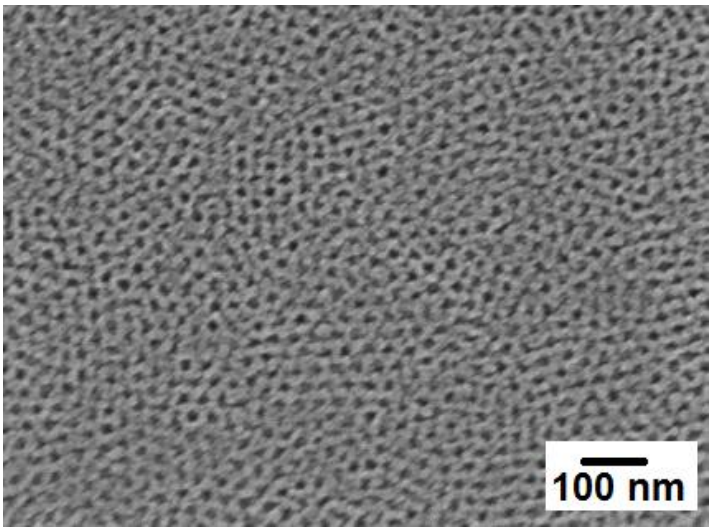

Figure 6.1. Scanning Electron Microscope image of a CFO films calcined at 500 ºC. The film is porous throughout and no blockage of the pores is observed.

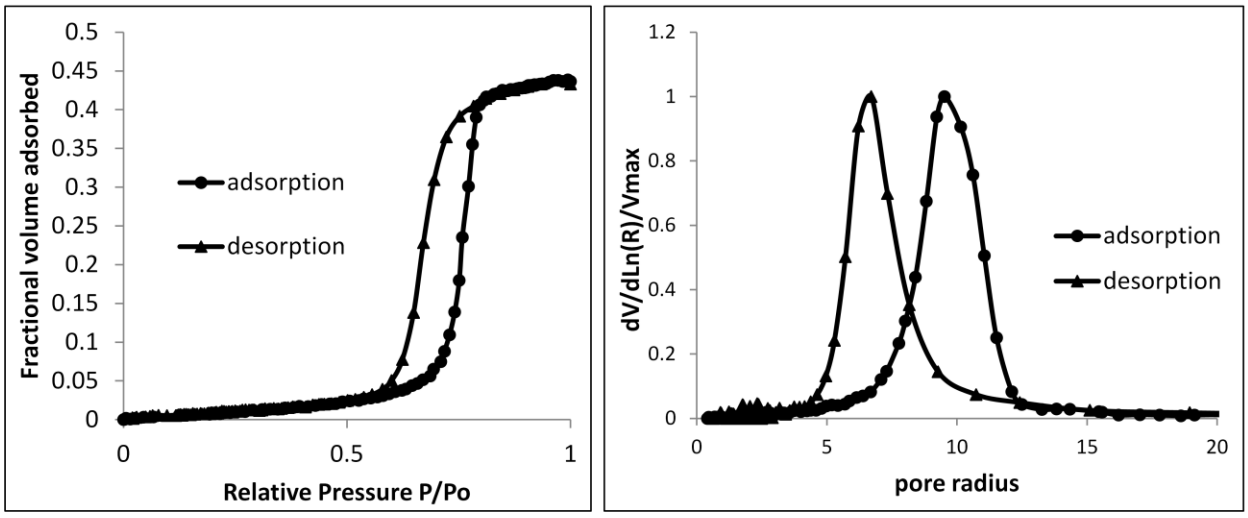

Figure 6.2. Toluene adsorption-desorption isotherm showing characteristic behavior for a mesoporous thin film of cobalt ferrite (a) Pore size distribution data obtained from the isotherm for a mesoporous cobalt ferrite film (b)

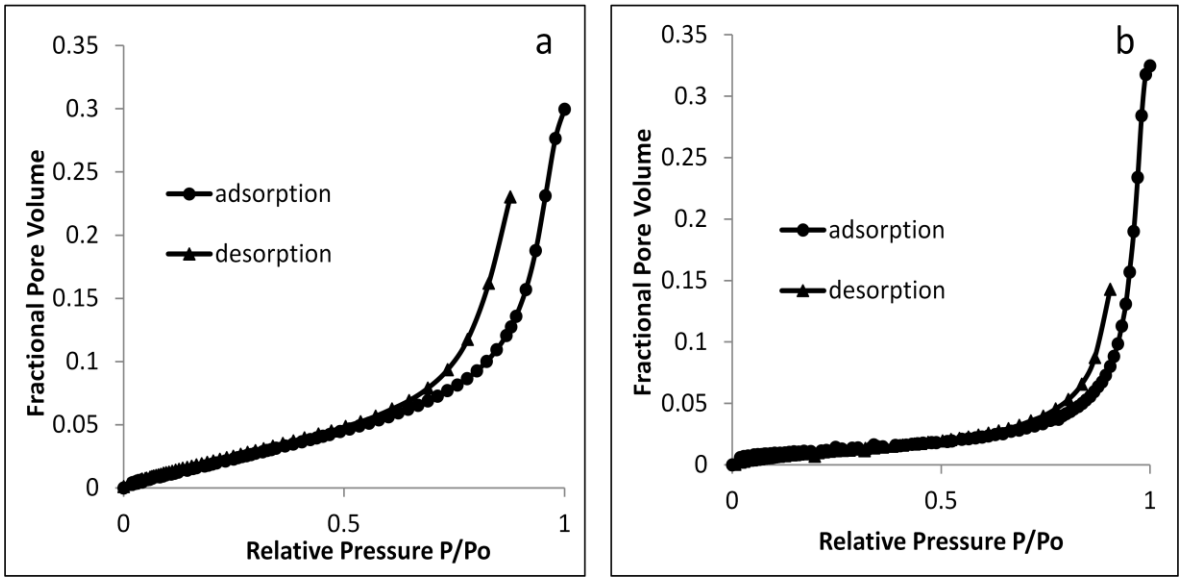

Figure 6.3. Isopentane absorption-desorption isotherm characteristic of a mesoporous thin film of cobalt ferrite (a) Adsorption-desorption isotherm for a CFO film using methanol (b)

however the hysteresis present, is at a higher relative pressure compared to that of toluene suggesting that the pore size is larger than what was previously observed. This difference in part occurs because we are using isopentane which is a new solvent in an already existing instrument therefore the solvent specific parameters are not specified for each fit. To determine the surface area of this film in figure 6.4a we show the BET fit to the isotherm obtained from isopentane adsorption. The range used to fit the data is from 0.1 to 0.3 relative pressure where the data was more linear than the generally used 0.05 - 0.3 range. The calculated area obtained from the analysis produces a surface area of approximately 207 m^2/cm^3 which corresponds to 85 m^2/g.

To calculate specific surface area of these films, we estimated the density based on the percent porosity of the film and the bulk density of cobalt ferrite. We assume this is a good approximation based on a correlation that exists for silica where the density decreases with porosity in proportional way.[22] For our calculations we assume a bulk density of cobalt ferrite[23] ($CoFe_2O_4$) of 3.45 g/cm^3. From the data in figure 6.2 we determined the film was 30% porous therefore we calculate a density for a porous CFO film of 2.4 g/cm^3.

Using methanol as the solvent, porosity measurements in figure 6.3b show a film that is also approximately 30% porous, which agrees with both toluene and isopentane isotherms. However, the hysteresis present, is at higher relative pressures than expected and this can be explain by a difference in wetting of methanol with the film. A BET fit to the isotherm shown in figure 6.4b using methanol over the range of 0.1 to 0.2 relative pressure produces a surface area of 230 m^2/cm^3, which corresponds to a specific surface area of 94 m^2/g. The difference produced by the two solvents can be attributed to the difference in the heat of adsorption of the first monolayer to the surface with the heat of liquefaction of the solvent. When the C parameter from the BET equation is calculated for both isopentane and methanol we obtain a value near 20. This

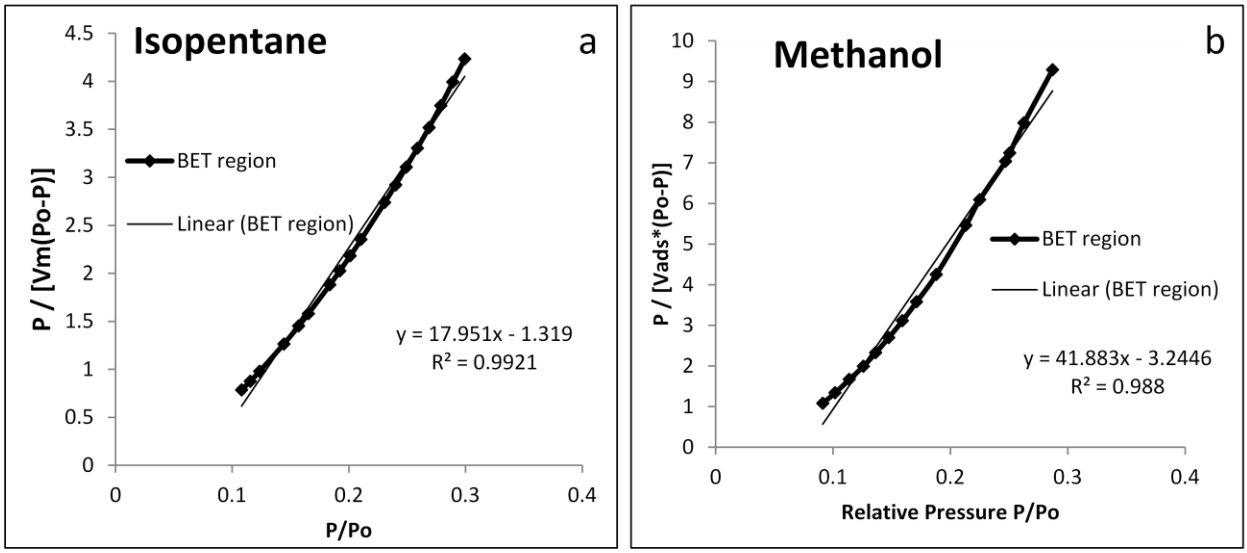

Figure 6.4. Linear fit to the BET region of a cobalt ferrite film isotherm using isopentane as the solvent (a) Linear fit to the BET region of a cobalt ferrite film isotherm using methanol as the solvent (b)

value of C is often considered too small, suggesting that the solvent-solvent interaction is greater with itself than with the surface being analyzed. This assumption will lead an overestimate of the surface area.

To further verify that the surface area obtained from isopentane and methanol are reasonable we also estimated the surface area of these types of films using a geometric analysis based on the percent porosity and pore size obtained from the toluene porosimetry measurement. Assuming the film to be 30% porous with spherical pores of 18 nm diameter and no other types of pores, we calculate a surface area of 112 m^2/cm^3 or 46 m^2/g. This value should underestimate the actual, surface area, however, as we are considering only the large pores and not the small necks. If, instead, we assumed that the film was made up of equal numbers of pores, half with 18 nm diameters and half with 10 nm diameters, we calculate a higher surface area of 146 m^2/cm^3 or 61 m^2/g.

6.3 Conclusions

Materials with high surface area have high demand for various applications, and full characterization of these materials is not generally done since there are a limited number of techniques available to measure the surface area of thin films. We proposed a new method to obtain the surface area of thin films using an already well-known technique, ellipsometric-porosimetry. By using two different solvents, isopentane and methanol, we obtained BET regions from where a surface area can be estimated. By exploring these two solvents we were able to overcome the limitation of doing ellipsometric-porosimetry at room temperature and thus we can generate a BET region that allows for the calculation of surface area in thin films. This method provides more flexibility for materials where surface area measurements are needed.

6.4 Experimental

6.4.1 Synthesis of mesoporous CFO films: Porous sol-gel films were made by dip-coating using a traditional Evaporation Induced Self-Assembly (EISA) process. In a typical synthesis $Fe(NO_3)_3 \cdot 9H_2O$ (0.31 g) and $Co(NO_3)_2 \cdot 6H_2O$ (0.11 g) are dissolved in 1mL of 2-methoxyethanol and 1mL of ethanol. The solution is allowed to stir for two to three days, after which PBO-PEO polymer (0.04 g) dissolved in 1 mL of warm ethanol is added, for a total sol volume of 3 mL. This sol is once more stirred for 1 h. Films are dip-coated from the solution onto silicon wafers in a humidity-controlled chamber set to approximately 13% relative humidity. The withdrawal rate varied between 0.3 and 0.6 cm/s, depending on desired thickness. The films were calcined under air at 180°C for 24 h to form rigid inorganic/organic composite structures. Crystallization and subsequent removal of the organic template were achieved by heating the films above 600°C using a 10°C/min ramp rate.

Immediate characterization of these films is done.

6.4.2 Methods: Scanning electron microscopy (SEM) images were obtained using a JEOL model 6700F electron microscope with beam energy 5 kV, and with a Zeiss Gemini Ultra-55 Analytical electron microscope with beam energy 5 kV. Ellipsometric porosimetry was performed on a PS-1000 instrument from Semilab using toluene as the adsorbate. A UV–visible CCD detector adapted to a grating spectrograph analyzes the signal reflected by the sample. The light source is a 75 W Hamamatsu Xenon lamp and measurements were performed on the spectral range from 1.24-4.5 eV. Data analysis was performed using the associated SEA software.

6.5 References

1. Perego, C. & Millini, R. Porous materials in catalysis: challenges for mesoporous materials. *Chem. Soc. Rev.* **42,** 3956–76 (2013).

2. Rauda, I. E. *et al.* General method for the synthesis of hierarchical nanocrystal-based mesoporous materials. *ACS Nano* **6,** 6386–99 (2012).

3. Rauda, I. E. *et al.* Nanoporous semiconductors synthesized through polymer templating of ligand-stripped CdSe nanocrystals. *Adv. Mater.* **25,** 1315–22 (2013).

4. Tricoli, A., Wallerand, A. S. & Righettoni, M. Highly porous TiO2 films for dye sensitized solar cells. *J. Mater. Chem.* **22,** 14254 (2012).

5. Badawy, W. a. A review on solar cells from Si-single crystals to porous materials and quantum dots. *J. Adv. Res.* **xxx,** (2013).

6. Search, H., Journals, C., Contact, A., Iopscience, M. & Address, I. P. A new technique for growing large surface area SnO2 thin film (RGTO technique). *Semicond. …* **1231,** 1231–1233 (1990).

7. Brezesinski, T., Wang, J. & Polleux, J. Templated nanocrystal-based porous TiO2 films for next-generation electrochemical capacitors. *J. Am. Chem. Soc.* 1802–1809 (2009). at <http://pubs.acs.org/doi/abs/10.1021/ja8057309>

8. Z-R. Tian, E. al. Manganese Oxide Mesoporous Structures: Mixed-Valent Semiconducting Catalysts. *Science (80-.).* **276,** 926–930 (1997).

9. Jr, G. G. & Cannon, P. On the energetics of physically adsorbed films, with particular reference to the use of krypton for surface area measurement. *J. Phys. Chem.* **313,** 7–10 (1960).

10. Krause, K. M., Thommes, M. & Brett, M. J. Pore analysis of obliquely deposited nanostructures by krypton gas adsorption at 87K. *Microporous Mesoporous Mater.* **143,** 166–173 (2011).

11. Klobes, P., Meyer, K. & Munro, R. G. *Porosity and Specific Surface Area Measurements for Solid Materials*. (2006).

12. Elam, J. W. & Pellin, M. J. GaPO 4 Sensors for Gravimetric Monitoring during Atomic Layer Deposition at High Temperatures. **77,** 3531–3535 (2005).

13. Fritze, H. & Tuller, H. L. Langasite for high-temperature bulk acoustic wave applications. *Appl. Phys. Lett.* **78,** 976 (2001).

14. Boissiere, C. *et al.* Porosity and mechanical properties of mesoporous thin films assessed by environmental ellipsometric porosimetry. *Langmuir* **21,** 12362–71 (2005).

15. Baklanov, M. R., Mogilnikov, K. P., Polovinkin, V. G. & Dultsev, F. N. Determination of pore size distribution in thin films by ellipsometric porosimetry. *J. Vac. Sci. Technol. B Microelectron. Nanom. Struct.* **18,** 1385 (2000).

16. Dultsev, F. & Baklanov, M. Nondestructive determination of pore size distribution in thin films deposited on solid substrates. *Electrochem. solid-state Lett.* **2,** 192–194 (1999).

17. Semilab. http://www.semilab.hu/products/si/ps-series.

18. Brunauer, S., Emmett, P. & Teller, E. Adsorption of gases in multimolecular layers. *J. Am. Chem. Soc.* **407,** (1938).

19. Brunauer, S. & Deming, L. On a theory of the van der Waals adsorption of gases. *J. Am. Chem. Soc.* **1139,** (1940).

20. Ricco, a. J., Frye, G. C. & Martin, S. J. Determination of BET surface areas of porous thin films using surface acoustic wave devices. *Langmuir* **5,** 273–276 (1989).

21. Nina, H. & Barron, A. R. BET Surface Area Analysis of Nanoparticles. 1–11

22. Jin, C., Luttmer, J., Smith, D. & Ramos, T. Nanoporous silica as an ultralow-k dielectric. *MRS Bull.* 39–42 (1997). at <http://journals.cambridge.org/abstract_S0883769400034187>

23. Iqbal, M. J. & Siddiquah, M. R. Electrical and magnetic properties of chromium-substituted cobalt ferrite nanomaterials. *J. Alloys Compd.* **453,** 513–518 (2008).

CHAPTER 7

Conclusions

This work demonstrates two distinct synthetic routes to producing thin films with nanoscale morphologies starting with solution processable precursors that allow for good control of the final architecture. Porous germanium films can be produced using a surface nucleated method in which the germanium precursor solution and the surfactant co-assembled into an ordered architecture that can produce a porous network. We establish two methods that are simple for getting continuous porous germanium films, for which the thickness can be tuned, and still show order and porosity.

Synthesis of mesoporous nanocrystal-based films was described starting from soluble precursors. Solution-phase assembly of bare nanocrystals with block copolymers produced mesoporous films with bimodal porosity. Micropores arise from the space in between the nanocrystals and mesorpores come directly from the space that was occupied by micelles formed by the block copolymers. Bare nanocrystals of various metal oxides, conductive metal oxides and metal-chalcogenide semiconductors, were stripped off their native ligands from their surface using a novel approach that involved using various salts, including $NOBF_4$ and Et_3OBF_4. This method produced highly dispersable nanocrystlas that serve as building blocks for the porous films. We demonstrated that using different block copolymer gives rise to a high degree of tenability of the mesopoer and changing the size of the nanocrystal also allowed us to tun the size of the micropore.

Semiconductors such as Cadmium selenide still maintain their nanocrystal properties when made into a templated a poropus network. It was demonstrated that CdSe semiconductor

materials keep the quantum confined excitonic features of CdSe nanocrystals as well as reasonable charge carrier transport, confirming that the nanocrystals are electronically interconnected in the film.

Materials that have redox active properties were studied for energy storage devices such as pseudocapacitors. A comparison of mesoporous lithium manganese ferrite nanocrystals with a film of the same nanocrystals that was not porous showed a significant difference in the pseudocapacitance obtained. However since a porous architecture was a major player in increasing the pseudocapacitance but it did not provide conductivity, a different electrode design was proposed. This involved using conductive ITO nanocrystals assembled into high surface area architectures that can provide an effective conductive platform. This scaffold was coated with a suitable redox-active material by atomic layer deposition. This type of construction made it possible to study other fundamental aspects of the architecture. For example, the limitations of film thickness on capacitive charge storage are of great interest in designing the ideal pseudocapacitor.

And finally we propose a new set of parameter to be able to measure surface area of thin films films using the already available ellipsometric-porosimetry technique at room temperature. By exploring two solvents, isopentane and methanol, we were able to overcome the limitation of doing ellipsometric-porosimetry at room temperature and thus generated a BET region that allowed us to calculate the surface area in a thin film

Appendix A

Detailed experimental procedures for the synthesis of germanium film precursors as well as a procedure for using the porosimeter

This section contains in detail the synthesis of the CTEAB surfactant, Zintl germanium precursor, Nanoporous Germanium Films as well as step by step procedures to use the ellipsometer porosimeter and associated SEA software.

A.1 Germanium film Synthesis

Materials: The following chemicals were purchased and used as received: Germanium powder (99.9% Alfa Aesar), Potassium metal (99.9% Afa Aesar) Ammonium Bromide (99.9% Alfa Aesar), Bomohexadecane (98% Aldrich), Triethylamine (96% Aldrich), Ethelene Diamine and Acetonitrile were distilled under Nitrogen using standard schlenk line techniques.

All procedures were carried out under inert atmosphere using standard glove box techniques.

A.1.1 CTEAB synthesis

CTEAB was made by combining 32 g of Bromohexadecane (Acros) with 24-26 g of triethylamine (Acros) in 100 mL of ethanol, the solution was heated for 3 days at 65 C. then thisa solution was evaporated using a rotovap and the precipitate was dissolved in 10 mL of Chloroform and about 400 mL of Diethyl Ether. The precipitate that formed was filtered using vacuum filtration. To further remove all impurities we dissolve The CTEAB with impurities in warm acetone ~400mL. Once allthe solid had dissolved the solution was cooled to room temperature overnight. The solid that precipitated again was filtered, dried and ready to be used.[1]

A.1.2 Synthesis of K_4Ge_9 precursor

0.3 g of elemental potassium was cut using a razor blade and heated in a ceramic crucible with 1.0 g of elemental germanium for 1 hr at 300 ºC to allow for mixing of the two metals. After 1 hour the crucible was allowed to cool and the mixture was grinded several times for 5 minutes each time to promote intimate mixing of the two elements. Once the mixture was well mixed it was returned to the oven for another round of heating to 300 ºC again to increase the alloying of the two components and obtain a higher yield. This mixture was then sealed in a sealed container. In our case we used a stainless steel flange that could resist temperatures of up to 1600 ºC. the powder was added to this flange and heated for 2 hours at 850 ºC to obtain the fully reduced K_4Ge_9 powder precursor. This powder was dissolved in 20 mL of ethylene diamine and allowed to settle, the supernatant was saved to make the precursor solution for the films and the powder was weighted to determine the amount dissolved so a concentration could be calculated.[2]

A.1.3 Synthesis of nanoporous germanium films

Interface Nucleated films: 2 mL of the K_4Ge_9 precursor solution was combined with 2mL of 0.3M Cetyltriethylammonium Bromide dissolved in ethylenediamine at 40°C. This mixture was allowed to come to equilibrium and 1 to 3 drops depending on the sample (0.1 mL) of 0.02 M NH_4Br was added to initiate the oxidation process from Ge_9^{4-} to the more polymeric species Ge_9^{2-} allowing the co-assembly process of zintl germanium with the surfactant to take place. A film starts to form at the top of the solution, if this does not happen then add one more drop of ammonium bromide. These films were carefully picked up using any type of very clean substrate; silicon for porosimetry measurements, glass for absorbance.

Spin-Coated thin-films 2 mL of the K_4Ge_9 precursor solution combined with 2mL of 0.3M Cetyltriethylammonium Bromide dissolved in ethylenediamine at 40^oC. This mixture was spin-coated onto clean polar substrates using an evaporation-induced self-assembly process.

In both cases, the surfactant self-assembles to form micelles in solution and by electrostatic attraction the anionic germanium precursor assembles around the surfactant to yield a mesostructured organic/inorganic composite.

Both types of films were given the same post-treatment to remove the surfactant. In each case the films were heated to 60 °C for 1 hour to strengthen the bonds. They were washed in a 0.3M NH_4Br solution in ethylenediamine to fully oxidize the germanium to neutral germanium, following by a wash in acetonitrile to remove any leftover surfactant on the film. To get rid of any surface oxidation the films were briefly submerged in 4%HF in ethanol right before doing any measurements.

A.2 Porosimeter instructions

The films to be measured must be of good optical quality otherwise the data obtained is not reliable. The size of the film can be as small as 0.5cm by 0.5 cm but anything smaller may not be hit by the light source.[3,4]

- To start make sure the PS-1000 software is open. Vent the sample holder chamber if it is under vacuum.
- Load the sample by opening the front door of the instrument. Make sure the gas tanks have enough Nitrogen, put the sample in the center of the stage. If the sample is large, put

it under the black circle which serves as a clamp. Do this by pulling on the two metal pieces sticking towards you.

* Create a recipe on the PS-1000 software that works well for your sample. Check that the solvent matches what is in the back of the tool, i.e. toluene, water etc.
* To run the recipe just click on run
* The data will be saved under the recipe folder under the date and time the data was taken. So make sure to note the date and time the recipe starts because this will be the name of the file.
* To fit the data use the associated SEA software that comes with the instrument. This software is fairly straight forward and easy to use
* This Figure shows a screen view of the tabs when the SEA software is opened. There can be seen 9 tabs at the top left of the screen. In Session create a session to start your analysis.

* Go to measure, here is where the data will be loaded, click on the + sign to add your set of data, make sure to add both adsorption and desorption.
* Go to structure, this is the most difficult part of the fit, you need to create a structure that matches your raw data, this is not trivial, as many parameters are taken into account. There are a few structures that have been saved over the years, but they are specific for a material. You need to play with all the parameter here until you get something that roughly matches your raw data so the software has a decent starting point.

* The thickness is a major factor, so make sure you roughly know how thick your films are, that will be very useful. Then choose either an NK file or a dispersion law, this depends on the material being analyzed.
* Once you have a structure that roughly matches your data go to Fit and click on start fit, this will start the iteration to best fit your raw data. Once you are happy with the fit, click update structure and this will save the new parameter.
* Once you are happy with the fit to the ellipsometry, then you can run the porosimetry fit. For this go to porosimetry fit, at the top left add the adsorption and desorption files, then click start. It will do all of the pressures.